2016

QUASI-MAGNETOSTATIC FIELD MODELING OF SHIPS IN THE PRESENCE OF DYNAMIC SEA WAVES

Cody Lonsbury
University of Kentucky, cody.lonsbury@gmail.com
Digital Object Identifier: http://dx.doi.org/10.13023/ETD.2016.070

STUDENT AGREEMENT:

I represent that my thesis or dissertation and abstract are my original work. Proper attribution has been given to all outside sources. I understand that I am solely responsible for obtaining any needed copyright permissions. I have obtained needed written permission statement(s) from the owner(s) of each third-party copyrighted matter to be included in my work, allowing electronic distribution (if such use is not permitted by the fair use doctrine) which will be submitted to UKnowledge as Additional File.

I hereby grant to The University of Kentucky and its agents the irrevocable, non-exclusive, and royalty-free license to archive and make accessible my work in whole or in part in all forms of media, now or hereafter known. I agree that the document mentioned above may be made available immediately for worldwide access unless an embargo applies.

I retain all other ownership rights to the copyright of my work. I also retain the right to use in future works (such as articles or books) all or part of my work. I understand that I am free to register the copyright to my work.

REVIEW, APPROVAL AND ACCEPTANCE

The document mentioned above has been reviewed and accepted by the student's advisor, on behalf of the advisory committee, and by the Director of Graduate Studies (DGS), on behalf of the program; we verify that this is the final, approved version of the student's thesis including all changes required by the advisory committee. The undersigned agree to abide by the statements above.

Cody Lonsbury, Student

Dr. John Young, Major Professor

Dr. Caicheng Lu, Director of Graduate Studies

QUASI-MAGNETOSTATIC FIELD MODELING OF SHIPS IN THE PRESENCE OF DYNAMIC SEA WAVES

THESIS

A thesis submitted in partial fulfillment of the
requirements for the degree of Master of Science
in Electrical Engineering in the College of Engineering
at the University of Kentucky

By

Cody Lonsbury

Lexington, Kentucky

Director: Dr. John Young

Lexington, Kentucky

2016

ABSTRACT OF THESIS

QUASI-MAGNETOSTATIC FIELD MODELING OF SHIPS
IN THE PRESENCE OF DYNAMIC SEA WAVES

Mechanical stresses placed on ferromagnetic materials while under the influence of a magnetic field are known to cause changes to the permanent magnetization of the material. Modeling this phenomenon is vital to the safety of ocean faring ships. In this thesis, a quasi-strip theory method of computing the nonlinear wave induced motion of a ship is developed, and the fluid pressure on the surface of the hull is used to determine the mechanical stresses. An existing magnetostatic volume integral equation code is used to evaluate the effects of the ship motion and hull stresses. The resulting changes in the magnetic field for various ship forms are presented to demonstrate the effects of given sea states.

KEYWORDS: Electromagnetics, Magnetostatics, Ship Motion, Dynamic Stress, Non Uniform Loading

Cody M. Lonsbury

April 21, 2016

QUASI-MAGNETOSTATIC FIELD MODELING OF SHIPS IN THE PRESENCE OF DYNAMIC SEA WAVES

By

Cody Lonsbury

Dr. John Young
Director of Thesis

Dr. Caicheng Lu
Director of Graduate Studies

April 21, 2016

ACKNOWLEDGEMENTS

First I must express my sincere gratitude to my advisor Dr. John Young who I have had the pleasure of working with as a research assistant for the past two years. His classroom instruction, willingness to answer my many questions, and meticulous attention to detail have been invaluable in my graduate studies and to the completion of my thesis.

I would like to thank Dr. Jonathan Wenk for all of his assistance in learning the fundamentals of rigid body dynamics necessary for this project. Furthermore, I would like to thank Dr. Robert Adams for serving on my defense committee.

I am indebted to Dr. Stephen Gedney for giving me the opportunity to work with the computational electromagnetics group during my undergraduate studies. His mentorship and passion for teaching have served as a great source of inspiration in my continuing education.

I must thank my family for all of their love and support. They have instilled in me from a young age the skills and desire necessary to be successful in life. Finally, I would like to thank my fiancée, who has been so supportive, and a much needed source of encouragement.

TABLE OF CONTENTS

LIST OF TABLES

TABLE OF FIGURES

1. INTRODUCTION

Most ships are made of ferromagnetic materials such as steel. When a ferromagnetic material is placed in a magnetic field, the material will cause a perturbation of the field around it. Knowledge of the perturbation of Earth's magnetic field is of great importance to the safety of naval ships due to hazards such as underwater mines. By accurately modeling the ship's magnetic field, techniques may then possibly be applied to decrease the field below the detection levels of these underwater threats [1]. There are four main sources of a ship's magnetic field: the induced and permanent magnetization of the ship's ferromagnetic steel, the induced eddy currents in the electrically conducting materials of the ship, electric currents in the hull due to electrochemical corrosion, and electric currents due to motors, generators, and other electrical equipment on board the ship [2].

The application of stress to ferromagnetic materials has been shown to cause significant changes to the magnetic field and more specifically the permanent magnetization [3-5]. Due to the dynamic nature of ocean waves, the hull of a ship is constantly subjected to large stresses from fluid pressure while also under the influence of Earth's magnetic field. While a ship is comprised of much more than just the outer hull, going forward this thesis will use the term hull to indicate all ferromagnetic material in the structure. The main stresses in the hull of a ship are induced by both hydrostatic and hydrodynamic pressure from the water thereby exciting nonlinear ship motion. In order to compute the actual stresses in the hull of a ship the nonlinear wave induced motion must be simulated. Computation of this wave induced motion can be performed in either the frequency domain or in the time domain. The advantage of frequency-domain

computations is that linear signal theory may be applied for irregular sea states so that the solutions of many different wave amplitudes and wave lengths may be superimposed [6], however this method fails to capture any nonlinear effects. Although time-domain methods include these nonlinear effects, it comes at the expense of much greater computational complexity.

In this thesis, a quasi-strip theory method is developed to solve for the nonlinear wave induced motion of a ship in the time domain. The wave induced pressure is used to compute the stresses in the hull with LS-DYNA [7], a commercial dynamic stress analysis code. Finally, these hull stresses will input to a quasi-magnetostatic volume integral equation code developed at the University of Kentucky, to calculate the magnetic field of a ship. A nonlinear transient solver is used to handle nonlinear hysteretic materials as well as a magnetostrictive materials. The main goal of this work is to expand the capabilities of quasi-magnetostatic field modeling to include the effects of wave induced dynamic stresses on the magnetic properties of ships.

This thesis is outlined as follows. Chapter 2 derives the six coupled equations of motion in the time domain along with a numerical solution method. Validation for each part of the code is given and the motion of two different ship forms are validated against other published results. Chapter 3 briefly discusses the magnetostatic volume integral equation and transient solver scheme. A description of LS-DYNA is also given. Results for the magnetostatic field of various ship models are shown for several ship headings and wave excitations. Finally chapter 4 discusses the accomplishments of this work and ideas for future development.

2. SHIP MOTION

2.1 Theory

The motion of a ship in dynamic sea waves can be determined from Newton's second law

$$\mathbf{M}\ddot{\boldsymbol{\eta}} = \mathbf{F} \ , \tag{1}$$

where $\mathbf{F}$ is a vector of forces and moments acting on the ship, $\mathbf{M}$ is the solid mass matrix, and $\ddot{\boldsymbol{\eta}}$ is a vector of the acceleration of the ship in each degree of freedom. If the coordinate system origin is set to the ship's center of gravity, the mass matrix simplifies to

$$\mathbf{M} = \begin{bmatrix} m & 0 & 0 & 0 & 0 & 0 \\ 0 & m & 0 & 0 & 0 & 0 \\ 0 & 0 & m & 0 & 0 & 0 \\ 0 & 0 & 0 & I_{xx} & 0 & 0 \\ 0 & 0 & 0 & 0 & I_{yy} & 0 \\ 0 & 0 & 0 & 0 & 0 & I_{zz} \end{bmatrix} , \tag{2}$$

where m is the mass of the ship and I_{xx} , I_{yy} , and I_{zz} are the moments of inertia about the three principal axes. The moments of inertia may be expressed in terms of the radius of gyration about each axis as

$$\begin{aligned} I_{xx} &= mk_{xx}^2 \\ I_{yy} &= mk_{yy}^2 \\ I_{zz} &= mk_{zz}^2 \end{aligned} \ . \tag{3}$$

If the distribution of mass is unknown, the radii of gyration may be approximated as [8]

$$\begin{aligned} k_{xx} &= 0.30B \;\; to \;\; 0.40B \\ k_{yy} &= 0.22L \;\; to \;\; 0.28L \\ k_{zz} &= 0.22L \;\; to \;\; 0.28L \end{aligned} \quad , \tag{4}$$

where B is the breadth and L is the length of the ship.

The forces on the right-hand side of (1) consist of both hydromechanical as well as viscous forces. Since the hydromechanical forces are typically orders of magnitude larger [6], viscous forces are typically neglected. To solve for the forces acting on the ship, a description of the fluid flow is required. For an ideal, incompressible, inviscid, and irrotational fluid, the pressure p on the hull of the ship may be found using Bernoulli's equation

$$p = -\rho g z - \rho \frac{\partial \phi}{\partial t} - \frac{\rho}{2} |\nabla \phi|^2 \;, \tag{5}$$

where ρ is the water density, g is the acceleration of gravity, z is the vertical distance below the still water surface, and ϕ is the velocity potential function which describes the fluid flow. An irrotational fluid implies

$$\nabla \times \mathbf{V} = 0 \,, \tag{6}$$

where $\mathbf{V} = \nabla \phi$ is the velocity vector of any fluid particle. The total force acting at the center of gravity of the ship is determined by integration of the pressure over the hull

$$\mathbf{F} = \oiint_S p \hat{\mathbf{n}} d\mathbf{s} \;. \tag{7}$$

The velocity potential ϕ in (5) satisfies all boundary conditions and Laplace's equation

$$\nabla^2 \phi = 0 \;. \tag{8}$$

Establishing boundary conditions with a ship travelling in wind generated waves is a difficult problem due to their time varying nature. By assuming that the squared particle velocities in (5) are small compared to the other terms, the Bernoulli equation may be linearized as

$$p = -\rho g z - \rho \frac{\partial \phi}{\partial t} \ . \tag{9}$$

Then, using the linear model, the solution for the forces acting on the ship are found by the superposition of several sub-problems. The velocity potential ϕ is divided into a sum of three potential functions

$$\phi = \phi^{Incident} + \phi^{Radiation} + \phi^{Diffraction} \ , \tag{10}$$

where the incident potential $\phi^{Incident}$ includes the hydrostatic restoring force and the Froude-Krylov force, which arises due to the unsteady pressure field generated by the undisturbed waves. The interaction of the incident wave with the ship will cause some waves to be scattered in other directions which is described by $\phi^{Diffraction}$. Finally, the wave induced motion generates additional waves that propagate away from the ship and are described by $\phi^{Radiation}$.

In the frequency domain the equation of motion becomes

$$(\mathbf{A} + \mathbf{M})\ddot{\boldsymbol{\eta}} + \mathbf{B}\dot{\boldsymbol{\eta}} + \mathbf{C}\boldsymbol{\eta} = \mathbf{F}e^{j\omega t} \ , \tag{11}$$

where $\mathbf{A}$ is the hydrodynamic added mass matrix describing the added resistance in moving the volume of water surrounding the ship, and $\mathbf{B}$ is the hydrodynamic damping due to the radiating waves. $\mathbf{C}$ is the restoring matrix from the hydrostatic pressure, and $\mathbf{F}$

is a vector of the excitation forces including the Froude-Krylov and diffraction forces. The response in irregular sea states can be easily computed in the frequency domain by solving (11) for multiple frequencies and/or wave heights and then superimposing the results. The disadvantage to this solution is that nonlinear effects are not captured in the frequency domain. This problem can be overcome by applying linear signal theory to compute the impulse response of the ship and then convert the frequency-domain solution to the time domain [9] such that the equation of motion becomes

$$(\mathbf{M}+\mathbf{A})\ddot{\boldsymbol{\eta}}(t)+\int_0^{\infty}\mathbf{K}(\tau)\dot{\boldsymbol{\eta}}(t-\tau)d\tau+\mathbf{C}\boldsymbol{\eta}(t)=\mathbf{X}(t) \tag{12}$$

where $\mathbf{K}$ represents the impulse response or retardation functions and $\mathbf{X}(t)$ is the sum of the time dependent external forces applied to the ship. The coupled set of motion equations in (12) are often referred to as the Cummins equations [10, 11] due to the significant contribution [9] made to the study of ship motion. Although (12) has to be solved in the time domain, the benefit is that nonlinear effects are captured and the added mass and damping coefficients may be calculated using fairly straightforward frequency-domain methods. The program flow for computing the ship's nonlinear motion is shown in Figure 1 and the computation of each of the components in (12) will be explained in detail in section 2.5.

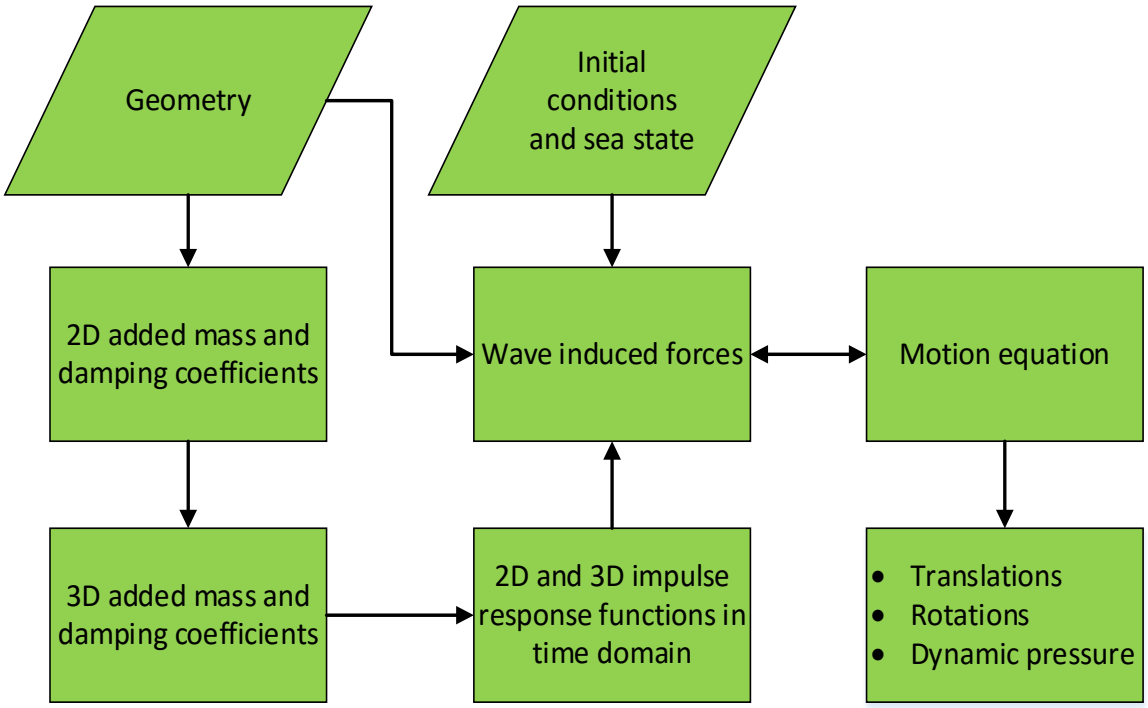

Figure 1. Ship motion program flow chart

2.2 Coordinate Systems

To fully describe the ship motion in waves, three coordinate systems are used as shown in Figure 2. A detailed explanation of each is as follows:

- OXYZ

  The Earth-fixed global coordinate system in which the wave is defined. The XY-plane lies in the still water plane with the negative X-axis pointing in the direction of wave propagation.

- oxyz

  The ship-fixed coordinate system with origin at the ship's center of gravity. The x-axis points in the ship's forward direction and the y-axis towards port side. The z-axis points upward and is always parallel to the global frame's Z-axis. This coordinate system translates only with the steady forward speed of the ship and the only rotation allowed is about the z-axis, which is defined by the ship's heading angle. The equations of motion are defined in this coordinate system.

- o*x*y*z*

  The body-fixed coordinate system has its origin fixed at the center of gravity of the ship. This coordinate system differs from the ship-fixed system only by three rotations about the x, y, and z axes. The rotational difference between the ship and body coordinate systems is described by the three Tait-Bryan angles.

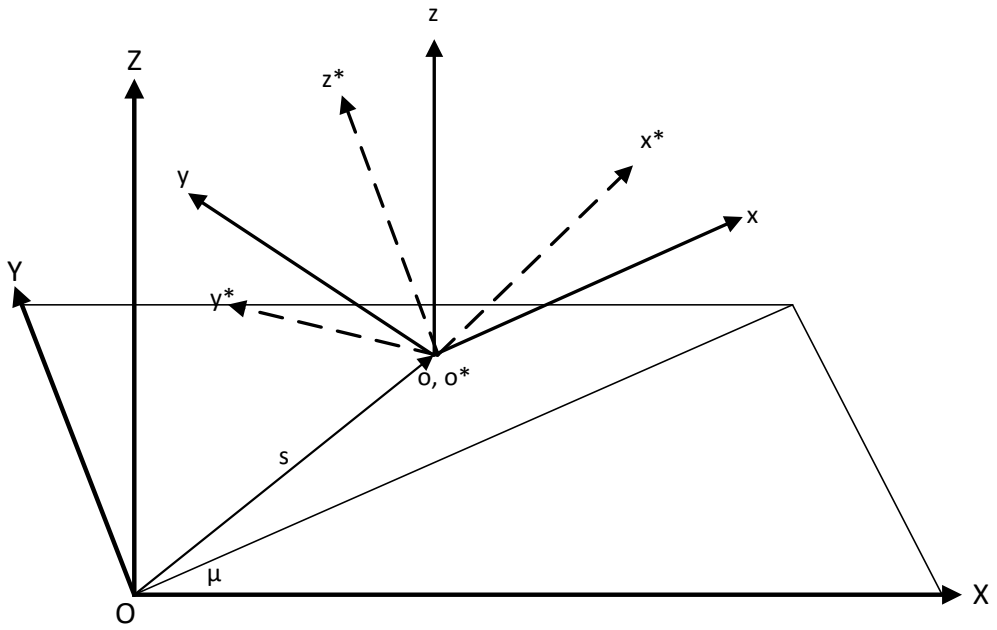

Figure 2. Illustration of the three coordinate systems used

2.3 Coordinate Transformations

To simplify the transformation between coordinate systems an auxiliary vector $\mathbf{s}$ is defined as

$$\mathbf{s} = \begin{bmatrix} Ut\cos(\mu) \\ Ut\sin(\mu) \\ VCG - T \\ 0 \\ 0 \\ \mu \end{bmatrix} + \boldsymbol{\eta} \ , \tag{13}$$

where $\boldsymbol{\eta}$ is a 6x1 vector containing the instantaneous motions and rotations of the ship and U is the ship's constant forward speed. VCG is the vertical center of gravity, the distance from CG to the keel, T is the ship draft, and μ is the ship's heading angle, the angle between the X-axis and x-axis as shown in Figure 2. The first three entries in $\mathbf{s}$ describe the translation from the global coordinate system to the body-fixed frame. The last three entries contain the Tait-Bryan angles which describe the rotation between the ship-fixed and body-fixed coordinate systems.

The transformation of a vector from one coordinate system to another can be described first by a translation and then a series of rotations about each coordinate axis. The rotation of a vector about a single axis by an angle θ can be found by multiplying the vector by one of the three rotation matrices

$$\mathbf{R}_x(\theta)=\begin{bmatrix}1 & 0 & 0\\ 0 & \cos(\theta) & -\sin(\theta)\\ 0 & \sin(\theta) & \cos(\theta)\end{bmatrix}$$
$$\mathbf{R}_y(\theta)=\begin{bmatrix}\cos(\theta) & 0 & \sin(\theta)\\ 0 & 1 & 0\\ -\sin(\theta) & 0 & \cos(\theta)\end{bmatrix}. \quad (14)$$
$$\mathbf{R}_z(\theta)=\begin{bmatrix}\cos(\theta) & -\sin(\theta) & 0\\ \sin(\theta) & \cos(\theta) & 0\\ 0 & 0 & 1\end{bmatrix}$$

The rotation about multiple axes is given by the product of matrices in (14) such that any rotation can be described by

$$\mathbf{T}=\mathbf{R}_z(\psi)\mathbf{R}_y(\theta)\mathbf{R}_x(\phi) \quad (15)$$

where ϕ, θ, and ψ are the roll, pitch, and yaw angles, respectively. Multiplying a vector by the transformation matrix in (15) will rotate the vector by the three Tait-Bryan angles in the same coordinate system. If instead of rotating the vector, the reference frame is being rotated as is the case between the oxyz and o*x*y*z* frames, the vector should be multiplied by the transpose of the rotation matrix. For example, using (15) a vector $\mathbf{V}$ in the global frame can be described in the body frame by

$$\mathbf{V}=\mathbf{T}\mathbf{v}^{*}+\mathbf{t}\ , \quad (16)$$

where

$$\mathbf{t}=\begin{bmatrix}\mathbf{s}_{11}\\ \mathbf{s}_{21}\\ \mathbf{s}_{31}\end{bmatrix} \quad (17)$$

is the translation vector. Due to the special orthogonality of the rotation matrix, the vector can be transformed back by

$$\mathbf{v}^{*} = \mathbf{T}^{\mathrm{T}}(\mathbf{V} - \mathbf{t}) \ . \tag{18}$$

2.4 Hydrodynamic Coefficients

The hydrodynamic potential coefficients are computed using a strip method. Local coefficients are calculated for each cross section and then the total hydrodynamic coefficients are found by integration along the length of the ship. To compute the local coefficients each section is first mapped to a more convenient circular cross section in the complex plane [8, 12]. The conformal mapping routine is detailed in Appendix B. Local hydrodynamic coefficients can now be computed for the circular cross sections based on the theory of Tasai [8, 13] resulting in the unknown coefficients in (19) and (20). A solution for these unknown coefficients is described in Appendix C. Once these local coefficients are computed for every cross section, the global coefficients may be calculated according to Appendix D.

$$\begin{aligned}
a_{22} &= \frac{\rho b_0^2}{2} \frac{M_0 Q_0 + N_0 P_0}{P_0^2 + Q_0^2} \\
a_{24} &= \frac{\rho b_0^3}{8} \frac{M_0 Q_0 + N_0 P_0}{P_0^2 + Q_0^2} \\
a_{33} &= \frac{\rho b_0^2}{2} \frac{M_0 B_0 + N_0 A_0}{A_0^2 + B_0^2} \\
a_{44} &= \frac{\rho b_0^4}{8} \frac{Y_R Q_0 + X_R P_0}{P_0^2 + Q_0^2}
\end{aligned} \tag{19}$$

$$
\begin{aligned}
b_{22} &= \frac{\rho b_0^2}{2} \frac{M_0 P_0 - N_0 Q_0}{P_0^2 + Q_0^2} \omega \\
b_{24} &= \frac{\rho b_0^3}{8} \frac{M_0 P_0 - N_0 Q_0}{P_0^2 + Q_0^2} \omega \\
b_{33} &= \frac{\rho b_0^2}{2} \frac{M_0 A_0 - N_0 B_0}{A_0^2 + B_0^2} \omega \\
b_{44} &= \frac{\rho b_0^4}{8} \frac{Y_R P_0 - X_R Q_0}{P_0^2 + Q_0^2} \omega
\end{aligned}
\tag{20}
$$

It should be noted that a_{24} and b_{24} are shown in [14] to have a negative sign, however according to [8] this is only correct in Tasai's coordinate system with the positive z-axis pointing in the downward direction. In any of the ship motion coordinate systems with z-axis pointing upwards both of these terms change sign.

2.5 Forces

2.5.1 Restoring and Froude-Krylov Forces

The restoring and Froude-Krylov forces are determined by integrating the two pressures over the momentary wetted hull at each time step. The pressures are integrated along the contour of each strip and then along the length of the ship. The restoring force is due to the hydrostatic pressure given by

$$
p^{rest} = -\rho g Z \ , \tag{21}
$$

where ρ is the density of the water, g is the acceleration due to gravity, and Z is the depth below the still water surface.

The Froude-Krylov force is due to the pressure from the undisturbed wave potential acting on the hull. For a wave propagating in the negative X-direction, the wave potential is given by [6]

$$\phi = -\frac{ga}{\omega}\frac{\cosh\left(k(Z+h)\right)}{\cosh(kh)}\sin(kX+\omega t) \ , \tag{22}$$

where a is the wave amplitude, $k = \frac{\omega^2}{g}$ is the wave number for deep water, and h is the sea depth. The Froude-Krylov force is then the integrated pressure from the undisturbed wave

$$p^{FK} = -\rho\frac{\partial\phi(X,Y,Z,t)}{\partial t} \ . \tag{23}$$

Note that X , Y , and Z are capitalized in (21), (22), and (23) as these equations are defined in the global coordinate system.

Typically for strip theory programs, the integration of these pressures follows [6]. First define $\mathbf{v}_i$ and $\mathbf{v}_{i+1}$ as vectors pointing to two subsequent points along a particular strip as shown in Figure 3. Let $\mathbf{n}_i$ be the unit normal to the line segment formed by the two consecutive points $\mathbf{v}_i$ and $\mathbf{v}_{i+1}$. By assuming the pressure varies linearly between these two points, the total force and moment produced on the segment due to the pressure are

$$\begin{aligned} f_j &= \sum_i \frac{p_i + p_{i+1}}{2} l_i \mathbf{n}_i \qquad 1 \le j \le 3 \\ f_j &= \sum_i \frac{p_i + p_{i+1}}{2} l_i (\mathbf{r}_i \times \mathbf{n}_i) \qquad 4 \le j \le 6 \end{aligned} \ , \tag{24}$$

where l_i is the length of the i-th segment given by

$$l_i = \left\| \mathbf{v}_{i+1} - \mathbf{v}_i \right\|_2 \ , \tag{25}$$

and $\mathbf{r}_i$ is a vector that points to the position on the segment where the total force is acting given by

$$\begin{aligned} \mathbf{r}_i &= \mathbf{v}_i + \frac{\frac{2}{3} p_{i+1} + \frac{1}{3} p_i}{p_{i+1} + p_i} (\mathbf{v}_{i+1} - \mathbf{v}_i) \qquad \text{if } \ p_i + p_{i+1} \neq 0 \\ \mathbf{r}_i &= \frac{\mathbf{v}_{i+1} - \mathbf{v}_i}{2} \qquad\qquad\qquad\qquad\quad \text{if } \ p_i + p_{i+1} = 0 \end{aligned} \ . \tag{26}$$

In the case of this work, a volume mesh rather than a strip mesh is used. Therefore the restoring and Froude-Krylov forces are computed by adaptively integrating the pressures over all wetted faces of the hull such that

$$\mathbf{F} = \int p \hat{\mathbf{n}} d\mathbf{s} \ , \tag{27}$$

and the moment about the center of gravity is

$$\mathbf{M} = \int \mathbf{r} \times (p \hat{\mathbf{n}}) d\mathbf{s} \ , \tag{28}$$

where $\mathbf{r}$ is a vector from CG to the particular integration point.

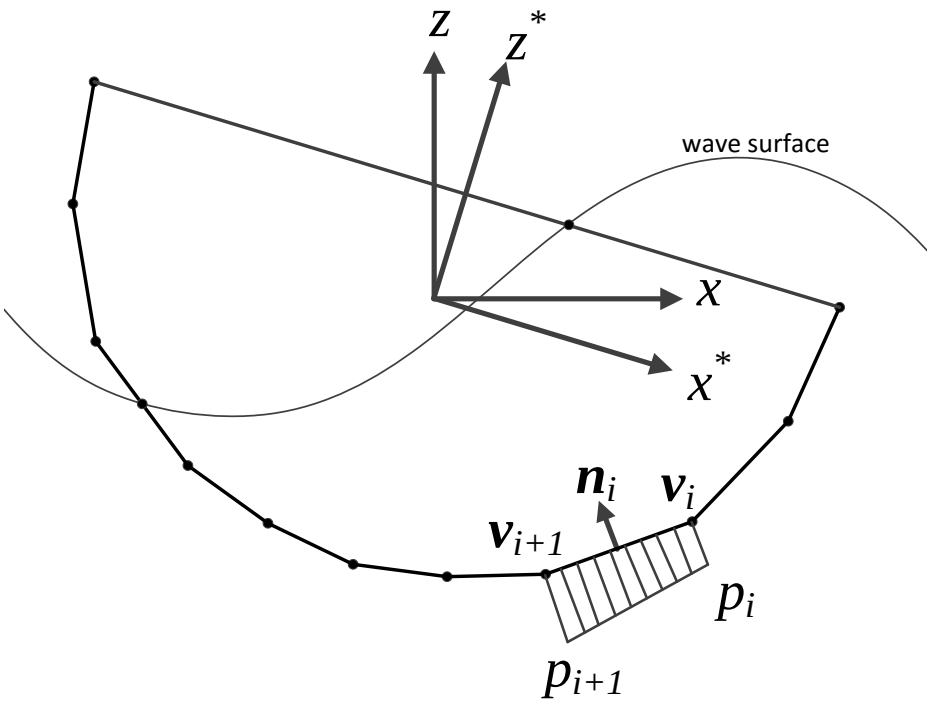

Figure 3. Pressure integration scheme for a single strip

2.5.2 Radiation Forces

Added mass and damping forces occur due to the induced oscillation of the ship. While the Froude-Krylov force is the primary excitation that causes the ship to accelerate, the damping forces control the resulting magnitude of the motion. These damping forces include both viscous and inviscid effects. As discussed in section 2.1, viscous effects are assumed to be negligible, which is a reasonable assumption for all degrees of freedom except roll [6]. No analytic solution has been found for calculating the damping forces in roll, however empirical models have been developed to estimate the damping coefficient. The implemented method to predict roll damping is discussed further in section 2.5.3.

The inviscid damping coefficients B_{ij} are computed in the frequency domain and transformed to the time domain according to the Cummins equation [6, 9] such that

$$F_i^{rad}(t) = \sum_{j=1}^{6}\left[-A_{ij}\ddot{\eta}_j(t) - \int_0^t K_{ij}(t-\tau)\dot{\eta}_j(\tau)d\tau\right] \tag{29}$$

where

$$K_{ij}(t) = \frac{2}{\pi}\int_0^\infty \Big(B_{ij}(\omega) - B_{ij}(\infty)\Big)\cos(\omega t)d\omega \ , \tag{30}$$

and

$$A_{i,j} = A_{i,j}(\omega) + \frac{1}{\omega}\int_0^\infty K_{i,j}(\tau)\sin(\omega\tau)d\tau \ . \tag{31}$$

Since (31) must be valid for all frequencies, the added mass in the time domain is simply equal to the added mass in the frequency domain as the frequency approaches infinity. Since potential theory fails to calculate hydrodynamic coefficients accurately at high

frequencies, (31) may be used to compute the infinite frequency added mass as long as $A_{i,j}(\omega)$ is known for just a single frequency. According to [10], the $B_{i,j}(\omega)$ terms should be calculated with forward speed effects included whereas the $A_{i,j}(\omega)$ terms should be calculated at zero speed.

In order to compute (30) numerically, the upper limit of integration must be truncated to some finite frequency such that

$$K_{ij}(t) = \frac{2}{\pi}\int_0^{\Omega} \Big(B_{ij}(\omega) - B_{ij}(\infty) \Big) \cos(\omega t) d\omega \tag{32}$$

with a suitable value of $\Omega = 5\,{}^{rad}\!/_{s}$ for normal merchant ships [14]. Computation of the radiation force in (29) includes an integral over the entire past motion history which can be an expensive computation for long simulation times. This interval may be reduced such that

$$F_i^{rad}(t) = \sum_{j=1}^{6} \left[-A_{ij}\ddot{\eta}_j(t) - \int_{t_1}^{t_2} K_{ij}(t-\tau)\dot{\eta}_j(\tau) d\tau \right] \tag{33}$$

where the new integration interval must be a minimum of five times the encounter frequency [6] which is defined as [15]

$$\omega_e = \omega + kU\cos(\mu) \ . \tag{34}$$

Care must also be taken to choose a small enough step size in frequency when computing the integral in (30) so as to avoid aliasing. This step size is dependent of the time interval $t = t_2 - t_1$ used to compute the radiation force. According to Nyquist's Theorem this gives a minimum frequency step size of

$$\Delta\omega \leq \frac{\pi}{t_2 - t_1} \ . \tag{35}$$

2.5.3 Viscous Damping in Roll Motion

The only degree of freedom where viscous effects are not negligible is in the roll motion. Although no analytic solution exists for computing the non-linear damping force, the use of empirical models are the industry standard to estimate the roll damping coefficient [16]. These models separate the roll damping into several components and ignore their interactions with each other. This gives the roll damping coefficient

$$B_{44} = B_F + B_W + B_E + B_{BK} + B_L \ , \tag{36}$$

where B_F is the frictional component, B_W is the wave component, B_E is the eddy component, B_{BK} is the bilge keel component, and B_L is the lift component due to forward speed. Detailed computation of each component is discussed in Appendix A. Once each component is computed the total viscous damping force in roll is expressed as

$$F^{roll-damp} = B_F\dot{\eta} + B_W\dot{\eta} + B_E\dot{\eta}\left|\dot{\eta}\right| + B_{BK} + B_L \tag{37}$$

For this work, the bilge keel component was not implemented.

2.5.4 Diffraction Forces

The diffraction forces are due to the scattered waves produced by the interaction of the excitation wave with the ship's hull. Along with the Froude-Krylov potential, the diffraction potential fulfills the boundary condition that no water penetrates the surface of

the ship's hull [6]. Like the radiation forces, the diffraction forces are transformed from the frequency domain to the time domain, however the diffraction force is computed with the ship held fixed within the impinging waves [6, 15]. Whereas other forces are computed in based on the ship's instantaneous time-dependent position in the global reference frame, the diffraction force is computed at each time step as if the ship is physically restrained to its equilibrium position. This implies that when transforming a point in the body-fixed coordinate system to the global system, the only translation is due to the draft, and the only rotation is due to the ship heading. According to [17] the diffraction force is given by

$$
\begin{aligned}
F_2^{diff} &= \int_L \left[a_{22}^{\infty} a_y(t) + \int_0^t k_{22}(t-\tau) v_y(\tau) d\tau \right] dx \\
F_3^{diff} &= \int_L \left[a_{33}^{\infty} a_z(t) + \int_0^t k_{33}(t-\tau) v_z(\tau) d\tau \right] dx \\
F_4^{diff} &= \int_L \left[a_{24}^{\infty} a_y(t) + \int_0^t k_{24}(t-\tau) v_y(\tau) d\tau \right] dx \quad , \\
F_5^{diff} &= -\int_L x \left[a_{33}^{\infty} a_z(t) + \int_0^t k_{33}(t-\tau) v_z(\tau) d\tau \right] dx \\
F_6^{diff} &= \int_L x \left[a_{22}^{\infty} a_y(t) + \int_0^t k_{22}(t-\tau) v_y(\tau) d\tau \right] dx
\end{aligned}
\tag{38}
$$

where k_{ij} are the sectional retardation functions computed by

$$
k_{ij}(t) = \frac{2}{\pi} \int_0^{\infty} b_{ij} \cos(\omega t) d\omega \ , \tag{39}
$$

a_{ij}^{∞} are the sectional added masses in the time domain, v_y, v_z, a_y, and a_z are the average particle velocities and accelerations in the y and z directions, respectively.

Cummins's derivation conveniently gives that the added mass in the time domain is equal to frequency-domain added mass when the frequency approaches infinity. However, strip methods fail to accurately compute hydrodynamic coefficients at high frequencies. Using the added mass for any one known frequency, the time-domain added mass may be computed as [10]

$$a_{ij}^{\infty} = a_{ij}(\omega) + \frac{1}{\omega}\int_0^{\Gamma_{ij}} K_{ij}(\tau)\sin(\omega\tau)d\tau \ , \tag{40}$$

where Γ_{ij} is the maximum time for which the retardation function was computed.

The particle velocities in the global coordinate system are the gradient of the potential function in (22)

$$\begin{aligned} v_y &= \frac{agk}{\omega}\frac{\cosh\left(k(Z+h)\right)}{\cosh(kh)}\cos(kX+\omega t) \\ v_z &= -\frac{agk}{\omega}\frac{\sinh\left(k(Z+h)\right)}{\cosh(kh)}\sin(kX+\omega t) \end{aligned} \ , \tag{41}$$

and the particle accelerations are the time derivative of the velocity functions

$$\begin{aligned} a_y &= -agk\frac{\cosh\left(k(Z+h)\right)}{\cosh(kh)}\sin(kX+\omega t) \\ a_z &= -agk\frac{\sinh\left(k(Z+h)\right)}{\cosh(kh)}\cos(kX+\omega t) \end{aligned} \ . \tag{42}$$

Since the particle velocity and acceleration varies with position in the cross section, the mean value for each cross section computed by

$$v_i = \frac{1}{T(Y_{\max} - Y_{\min})(X_{\max} - X_{\min})} \int_{-T}^{0} \int_{Y_{\min}}^{Y_{\max}} \int_{X_{\min}}^{X_{\max}} v_i(X,Y,Z)\,dXdYdZ \qquad i = x, y, z$$
$$a_i = \frac{1}{T(Y_{\max} - Y_{\min})(X_{\max} - X_{\min})} \int_{-T}^{0} \int_{Y_{\min}}^{Y_{\max}} \int_{X_{\min}}^{X_{\max}} a_i(X,Y,Z)\,dXdYdZ \qquad i = x, y, z \tag{43}$$

where T is the draft of the cross section and $X_{\min}$, $X_{\max}$, $Y_{\min}$, and $Y_{\max}$ are the minimum and maximum coordinates of the cross section.

2.6 Solving the Coupled Equations of Motion

The equation of motion in six degrees of freedom can be expressed as the second-order differential equation

$$(\mathbf{M} + \mathbf{A})\ddot{\boldsymbol{\eta}} + \mathbf{B}\dot{\boldsymbol{\eta}} + \mathbf{C}\boldsymbol{\eta} = \mathbf{F}_{ext} \ . \tag{44}$$

Once all forces acting on the ship are determined, the motion equation can be rewritten as

$$(\mathbf{M} + \mathbf{A})\ddot{\boldsymbol{\eta}} = \mathbf{F}^{rest} + \mathbf{F}^{FK} + \mathbf{F}^{rad} + \mathbf{F}^{diff} + \mathbf{F}^{roll-damp} \ . \tag{45}$$

In order to solve this second order differential equation, the six equations are written as the twelve first order equations:

$$
\begin{aligned}
\dot{y}_1 &= \dot{\eta}_1 \\
\dot{y}_2 &= \dot{\eta}_2 \\
\dot{y}_3 &= \dot{\eta}_3 \\
\dot{y}_4 &= \dot{\eta}_4 \\
\dot{y}_5 &= \dot{\eta}_5 \\
\dot{y}_6 &= \dot{\eta}_6 \\
\dot{y}_7 &= \ddot{\eta}_1 \\
\dot{y}_8 &= \ddot{\eta}_2 \\
\dot{y}_9 &= \ddot{\eta}_3 \\
\dot{y}_{10} &= \ddot{\eta}_4 \\
\dot{y}_{11} &= \ddot{\eta}_5 \\
\dot{y}_{12} &= \ddot{\eta}_6
\end{aligned}
\quad , \tag{46}
$$

which all y_i are then solved for numerically using a 4th order Runge-Kutta method.

2.7 Validation of the Motion Code

Hydrodynamic coefficients were computed for a rectangular section with breadth of 0.4 m and draft of 0.2 m. The coefficients are plotted in Figure 3 and compared to data published from [18]. The coefficients a_{22} and b_{33} computed for the midship section of the S-175 container ship [14, 19] are shown in Figure 6 alongside results published in [20]. Figure 7 shows the total added mass in sway and damping coefficient in heave for the S-175 with a forward speed of 10 knots. These computed hydrodynamic coefficients show good agreement with the published results. Although the sectional coefficients in Figure 6 match very well, there is a small amount of error shown in the 3D coefficients of Figure 7.

Integration along the length of the ship in [20] is performed using Simpson's rule [8] while this work's computed results use a midpoint rule which could explain the small difference.

The viscous damping computation was validated against Ikeda's Fortran code [21] using the S-175, and the results are shown in Figure 8. The dimensions of the S-175 are shown in Table 2, and the strip mesh is shown in Figure 5. Excellent agreement with the reference results is exhibited. The full nonlinear motion code was validated first using a simple box shaped ship excited by a 0.1 m amplitude wave with varying frequencies. The dimensions of the box ship are shown in Table 1. Headings of 0 degrees, 45 degrees, and 90 degrees were simulated for zero forward speed and the results are compared to data from [6] as shown in Figure 9-10. Due to the symmetry of the box, the results for headings of 135 degrees and 180 degrees are identical to those for headings of 45 degrees and 0 degrees respectively. For each frequency, the simulation was run until the ship reached steady state and then the peak amplitude of each motion mode was used to create the response functions. The heave motion is normalized by the wave amplitude while the roll and pitch motions are normalized by the wave slope defined as

$$\kappa = ka \ . \tag{47}$$

The frequency response agrees very well with the published results for heave and pitch motions and a slight amount of error is seen in roll. For the data produced by this work the frictional component of the roll damping coefficient was empirically scaled by a value of 300 in order to more closely match the reference data. The difference in response is likely due to the reference data using a different model for the roll damping coefficient, and insufficient information was given to determine the values used. Next the frequency response functions were simulated for the box with forward speed of 10 knots as shown in

Figure 12-15. Again the results show good agreement and are well within the range of other reported results from [6].

Finally, the S-175 container ship with 0 degree heading was simulated with 1 m amplitude wave with a period of 10.5 s. The motion as a function of time for heave is shown in Figure 17 and the pitch motion is shown in Figure 18 with comparisons to data from [14]. For both of these plots an initial condition was used that was determined from a previous simulation once the ship reached steady state. Excellent agreement is shown with the results from VERES, however it can be noticed that the computed motion is slightly asymmetrical in comparison. This may be due to the reference data being computed using the linear equations of motion [14] whereas the full nonlinear motion equations were solved in this work. Lastly the pitch motion is seen to be 180° out of phase with the reference data which may be a result of the wave propagating in the opposite direction. Due to some inconsistencies in the signs of several wave potential terms in [14] it is uncertain in which direction the wave propagates.

Table 1. Box ship dimensions and parameters

Length	40 m
Breadth	8 m
Height	4 m
Draft	2 m
Mass	656,000 kg
Longitudinal center of gravity (LCG)	0 m
VCG	2 m
k_{xx}	3.2 m
k_{yy}	10 m
k_{zz}	10 m

Table 2. S-175 ship dimensions and parameters

Length	175 m
Breadth	25.4 m
Draft	9.5 m
Mass	2.46×10^{7} kg
Longitudinal center of gravity (LCG)	2.34 m (aft midship)
VCG	9.52 m
k_{xx}	10.16 m
k_{yy}	44.16 m
k_{zz}	44.16 m

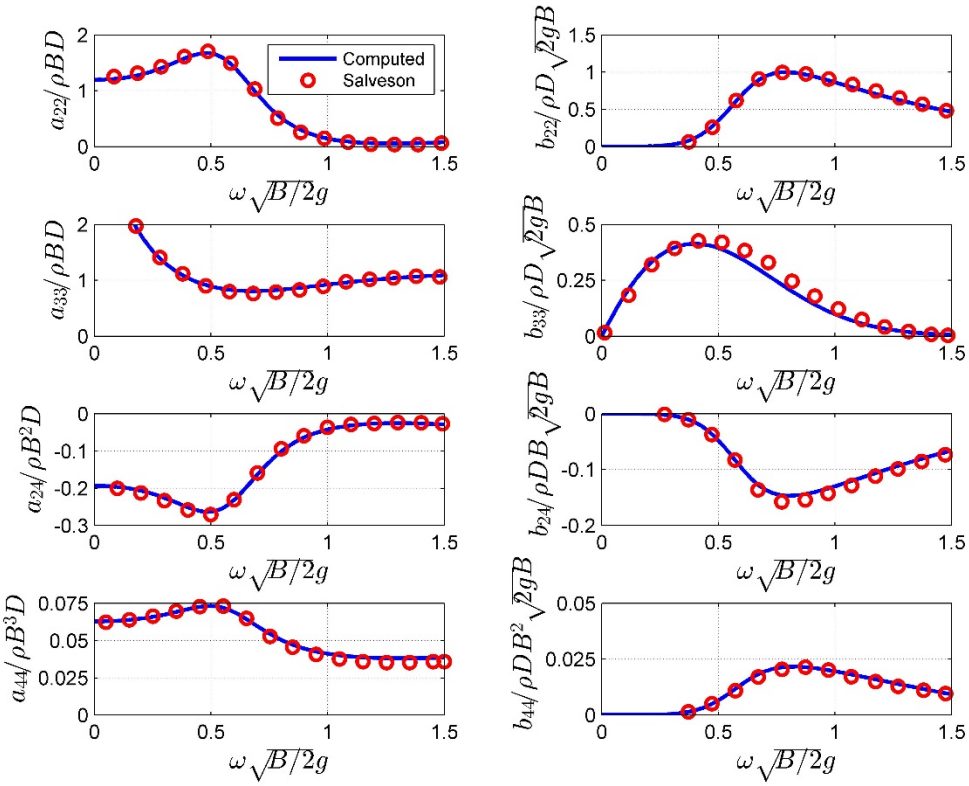

Figure 4. Normalized frequency dependent hydrodynamic coefficients of a rectangular section with breadth of 0.4 m and draft of 0.2 m.

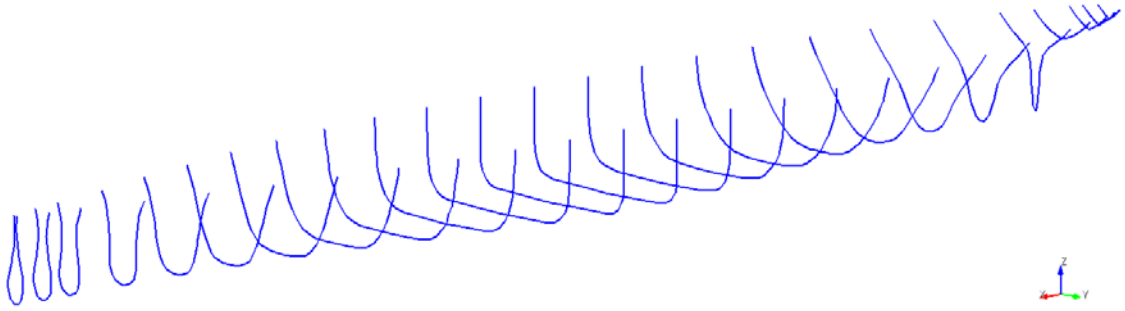

Figure 5. S-175 strip mesh

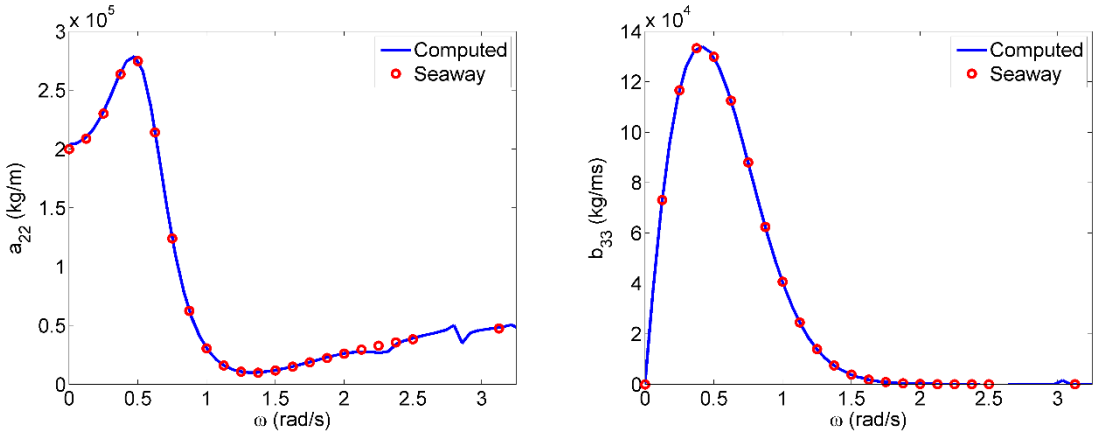

Figure 6. S-175 container ship midship sectional (a) added mass in sway (b) damping coefficient in heave.

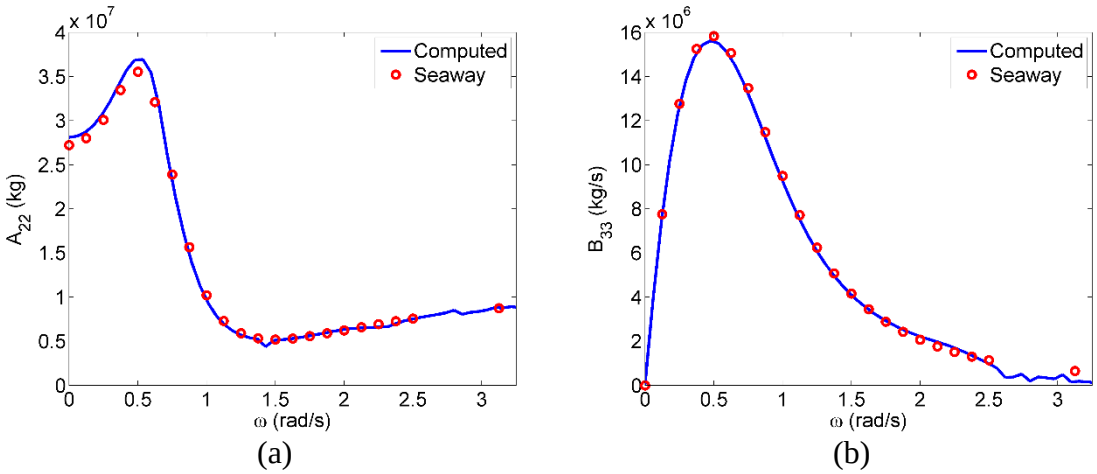

Figure 7. S-175 container ship (a) added mass in sway (b) damping coefficient in heave.

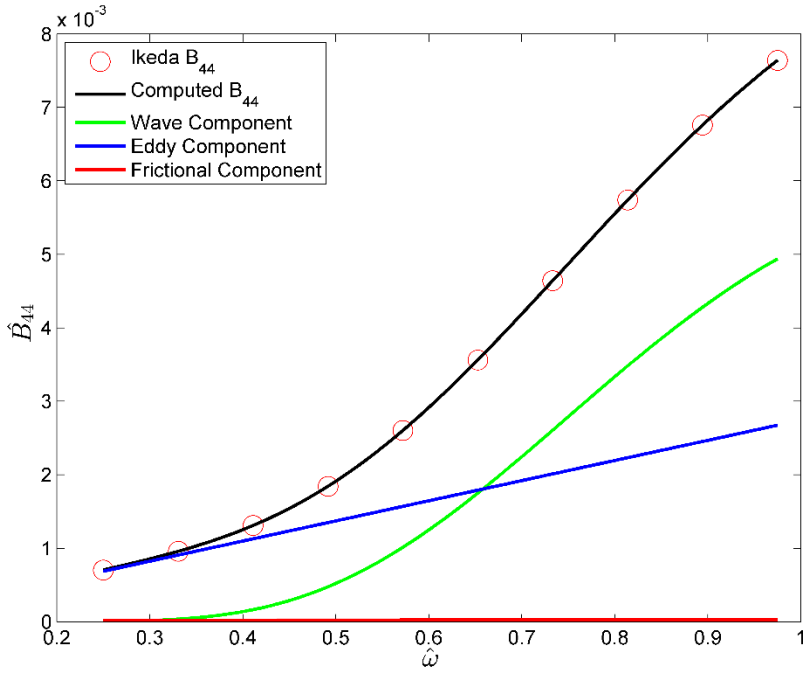

Figure 8. Non-dimensional frequency dependent viscous damping coefficient for S-175 container ship at a roll angle of 10 degrees.

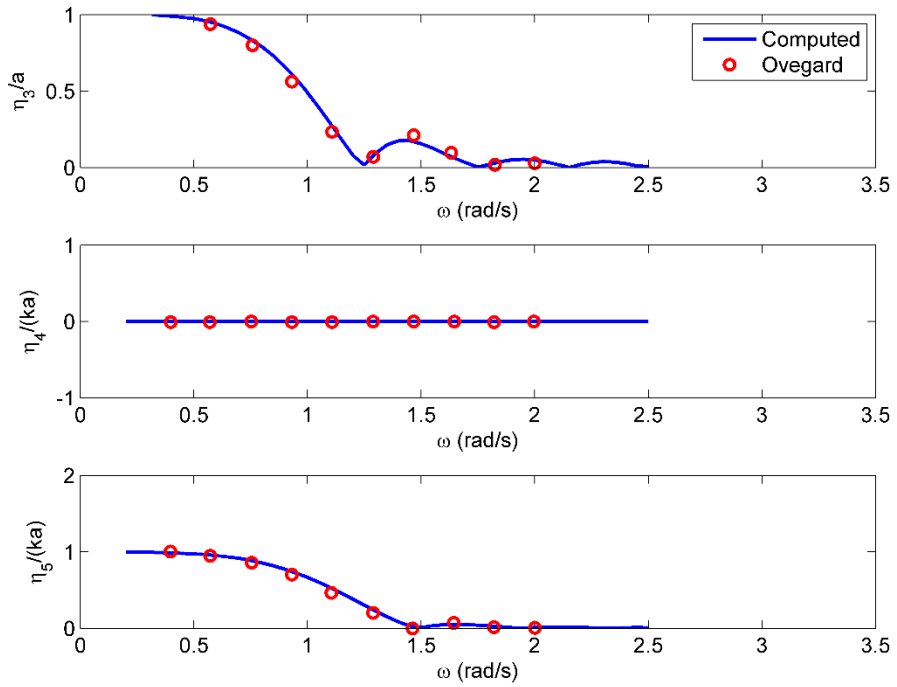

Figure 9. Frequency response amplitude of the box ship with 0 degree heading at zero speed.

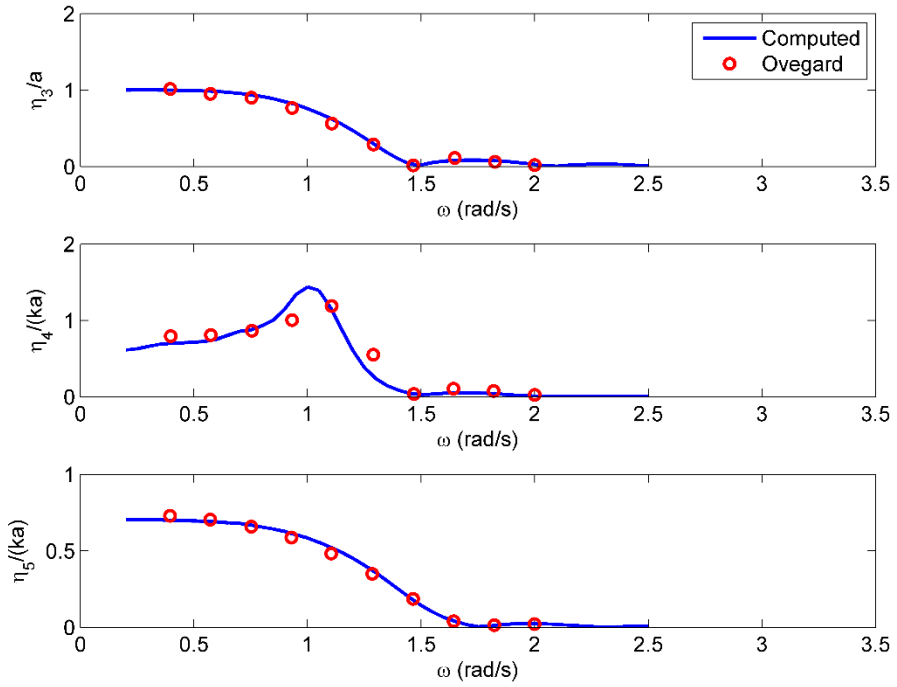

Figure 10. Frequency response amplitude of the box ship with 45 degree heading at zero speed.

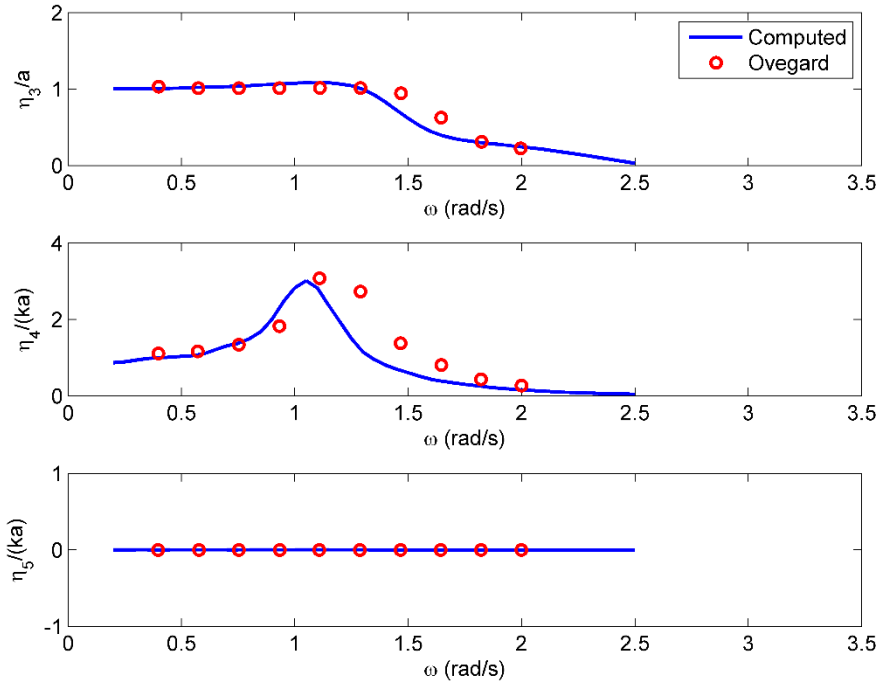

Figure 11. Frequency response amplitude of the box ship with 90 degree heading at zero speed.

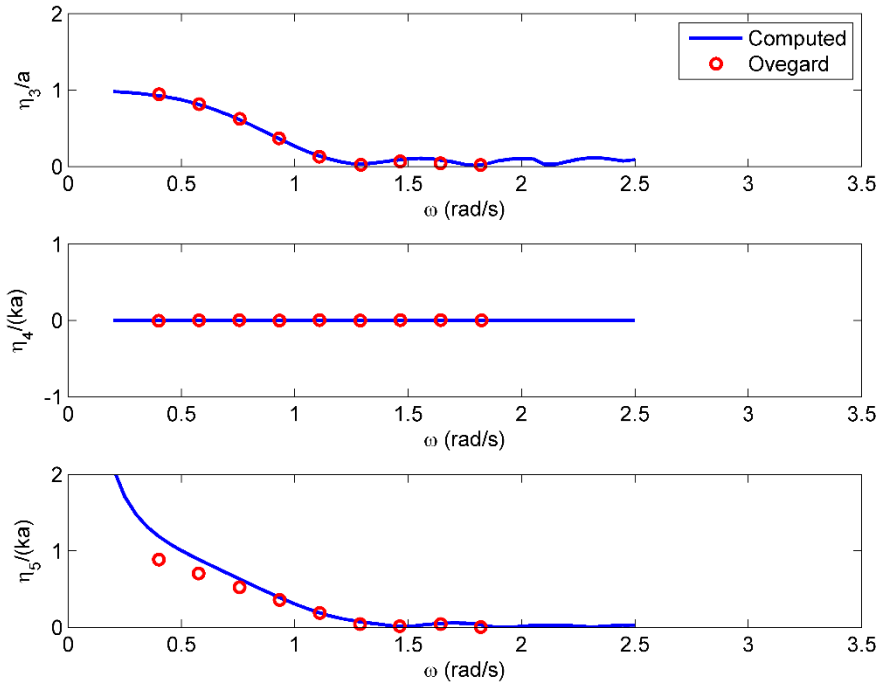

Figure 12. Frequency response amplitude of the box ship with 0 degree heading at 10 knots.

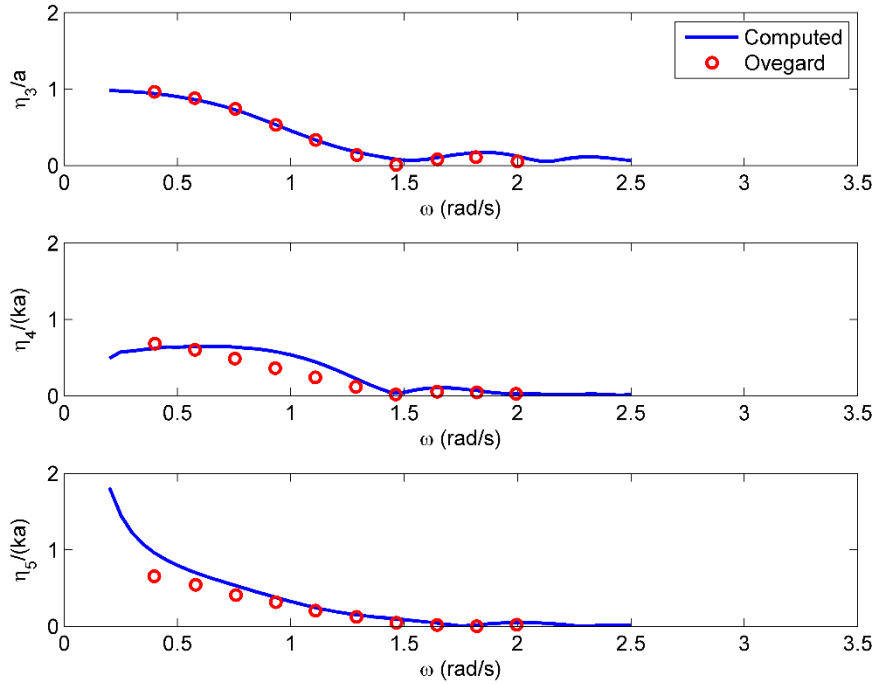

Figure 13. Frequency response amplitude of the box ship with 45 degree heading at 10 knots.

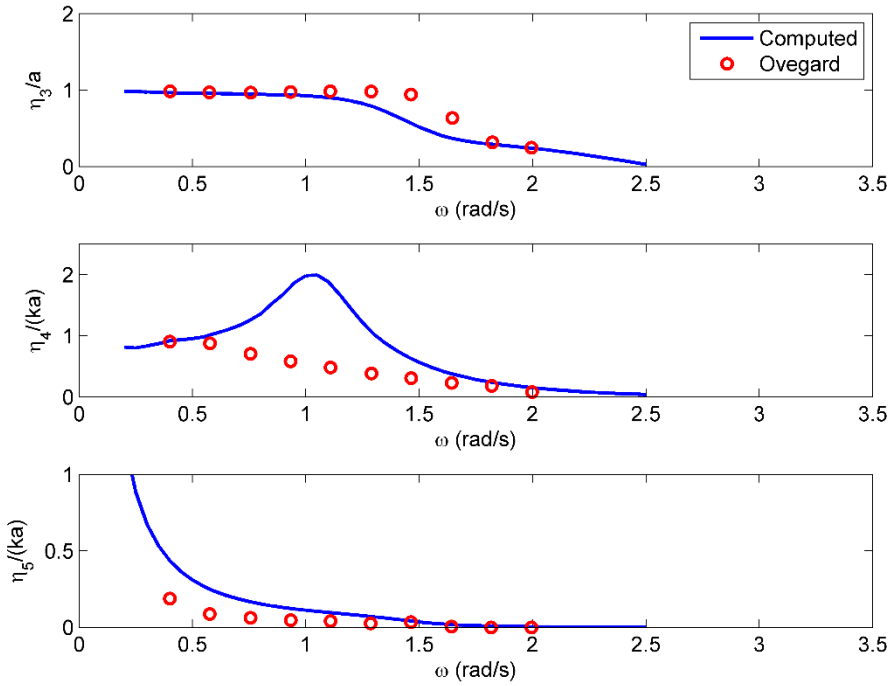

Figure 14. Frequency response amplitude of the box ship with 90 degree heading at 10 knots.

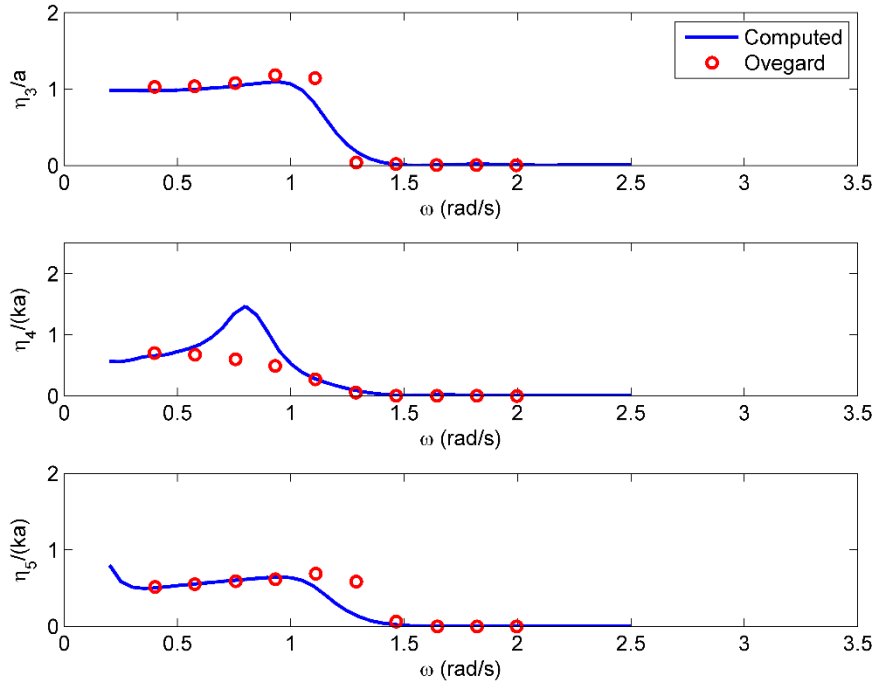

Figure 15. Frequency response amplitude of the box ship with 135 degree heading at 10 knots.

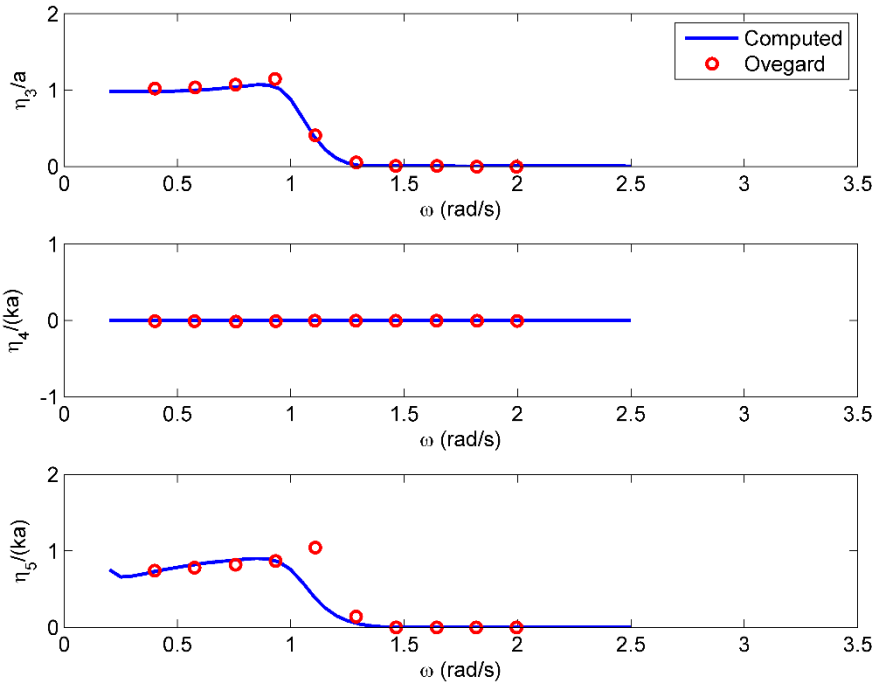

Figure 16. Frequency response amplitude of the box ship with 180 degree heading at 10 knots.

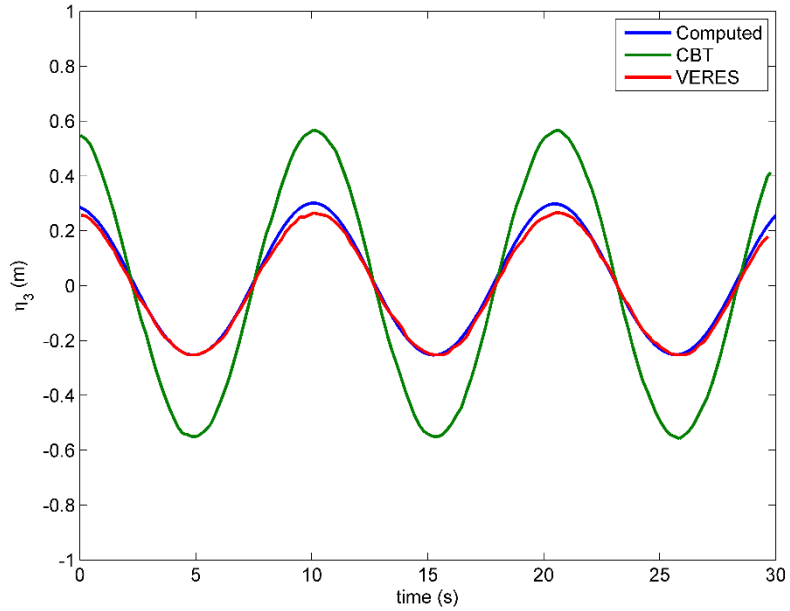

Figure 17. Heave motion time history for the S-175 compared with results published in [14]. The ship has zero forward speed and is excited by a 1 m head on wave.

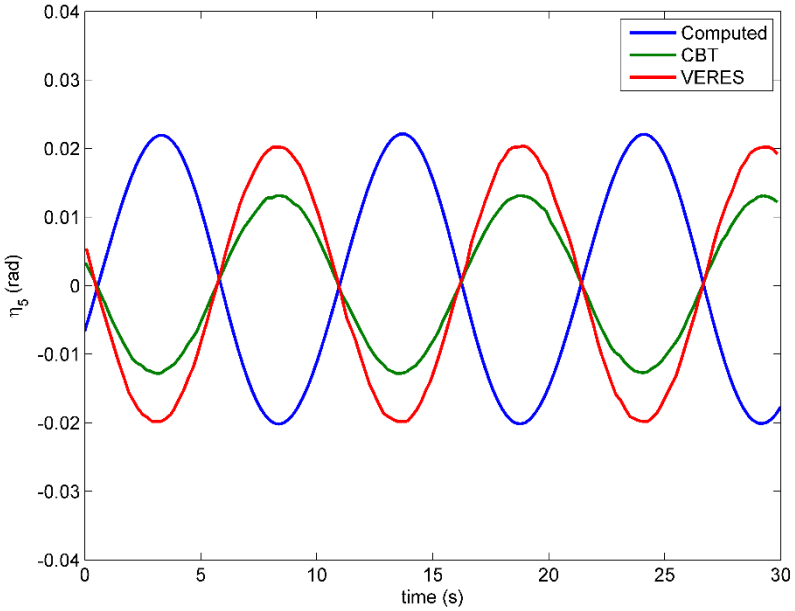

Figure 18. Pitch motion time history for the S-175 compared with results published in [14]. The ship has zero forward speed and is excited by a 1 m head on wave.

3. MAGNETIC FIELD MODELING

A discussion of the magnetic field modeling requires more precise notation. Therefore, this chapter will use an arrow above a variable to distinguish that it is a vector in $\mathbb{R}^3$, while a matrix or vector used in a linear algebra operation will remain in bold.

3.1 The Magnetostatic Volume Integral Equation

Consider a magnetic material placed in a magnetostatic field produced by an external source. The material has inhomogeneous permeability tensor $\bar{\bar{\mu}}(\vec{r})$. The presence of the material will alter the magnetic field in which the resulting total magnetic field $\vec{H}$ may be expressed as [22]

$$\vec{H} = \vec{H}_s + \vec{H}_p \tag{48}$$

where $\vec{H}_s$ is the source field and $\vec{H}_p$ is the perturbation of the field due to the magnetic material. In the absence of free electric current, a magnetic scalar potential ϕ_p for the perturbed field may be defined and (48) may be rewritten as

$$\vec{H} = \vec{H}_s - \nabla\phi_p \ . \tag{49}$$

The magnetic flux density is

$$\vec{B} = \mu_0(\vec{H} + \vec{M}) = \mu_0\vec{H}_s - \mu_0\nabla\phi_p + \mu_0\vec{M} \tag{50}$$

where μ_0 is the permeability of free space. The magnetization vector $\vec{M}$ is defined by

$$\vec{M}(\vec{r}) = \bar{\bar{\chi}}_m(\vec{r}) \cdot \vec{H} \tag{51}$$

where $\bar{\bar{\chi}}_m(\vec{\mathrm{r}}) = \bar{\bar{\mu}}_r(\vec{\mathrm{r}}) - \mathbf{I}$ is the magnetic susceptibility. Taking the divergence of (50) results in

$$\nabla \cdot \vec{B} = \mu_0 \nabla \cdot (\vec{H} + \vec{M}) = 0 \ , \tag{52}$$

thus

$$\nabla \phi_p^2 = -\rho^* = \nabla \cdot \vec{M} \tag{53}$$

where ρ^* is the magnetic charge density. Poisson's equation in (53) has the known solution

$$\phi_p(\vec{r}) = \iiint_V \rho^*(\vec{r}\,') \frac{1}{4\pi R} dv' + \iint_S \rho_s^*(\vec{r}\,') \frac{1}{4\pi R} ds' \ , \tag{54}$$

where $R = \left| \vec{r} - \vec{r}\,' \right|$ and the magnetic surface charge density

$$\rho_s^* = \hat{n} \cdot \vec{M} \Big|_S \tag{55}$$

is due to the magnetization vector being discontinuous on the boundary S. Plugging (53) and (55) into (54) results in

$$\phi_p(\vec{r}) = -\iiint_V \frac{\nabla' \cdot \vec{M}(\vec{r}\,')}{4\pi R} dv' + \oiint_S \frac{\vec{M}(\vec{r}\,')}{4\pi R} dv' \ . \tag{56}$$

Using a vector identity the first term in (56) can be rewritten as

$$\iiint_V \frac{\nabla' \cdot M(\vec{r}\,')}{4\pi R} dv' = \oiint_S \frac{M(\vec{r}\,')}{4\pi R} \cdot ds' + \nabla \cdot \iiint_V \frac{M(\vec{r}\,')}{4\pi R} dv' \tag{57}$$

in which (56) now becomes

$$\phi_p(\vec{r}) = -\nabla \cdot \iiint_V \vec{M}(\vec{r}') \frac{1}{4\pi R} dv' \ . \tag{58}$$

Finally, combining (49), (51), and (58) gives the magnetostatic volume integral equation

$$\vec{H}_s(\vec{r}) = \bar{\bar{\chi}}_m^{-1}(\vec{r}) \cdot \vec{M}(\vec{r}) - \iiint_V \vec{G}(\vec{r}, \vec{r}') \cdot \vec{M}(\vec{r}') dv' \tag{59}$$

where $\vec{G}$ is the dyadic Green's function which satisfies

$$\vec{G}(\vec{r}, \vec{r}') \cdot \vec{M}(\vec{r}') = \nabla\nabla \cdot \left(\frac{\vec{M}(\vec{r}')}{4\pi \left| \vec{r} - \vec{r}' \right|} \right) \ . \tag{60}$$

The implemented magnetostatic volume integral equation uses a locally corrected Nyström method to numerically solve (59) [22].

3.2 Nonlinear Transient Solver

Using the locally corrected Nyström discretization, the magnetostatic volume integral equation (59) may be expressed in matrix form as [23]

$$\mathbf{H}^S = \mathbf{Y}^\chi \mathbf{M} - \mathbf{Y}\mathbf{M} \ . \tag{61}$$

A nonlinear transient solver based on the differential susceptibility is implemented in order to implicitly handle hysteretic materials. The differential susceptibility $\bar{\bar{\chi}}^d$ satisfies

$$\bar{\bar{\chi}}^d(\vec{r}) = \frac{\partial \vec{M}(\vec{r})}{\partial \vec{H}(\vec{r})} \approx \frac{\delta \vec{M}(\vec{r})}{\delta \vec{H}(\vec{r})} \ , \tag{62}$$

where δ represents an approximation to the differentials. By denoting the change in a quantity from step $k-1$ to k to be

$$\delta \mathbf{P}^k = \mathbf{P}^k - \mathbf{P}^{k-1} \ , \tag{63}$$

then (61) can be written as

$$\delta \mathbf{H}^{s,k} = \mathbf{Y}^{\chi^d,k} \delta \mathbf{M}^k - \mathbf{Y} \delta \mathbf{M}^k \ . \tag{64}$$

In order to use the given transient solver, a model for the differential susceptibility must be known beforehand, whether analytic or computed within the simulation. For each step k the solution to (64) is obtained as follows:

1. For the initial step $k = 0$, $\mathbf{M}^{-1} = 0$, $\mathbf{H}^{-1} = 0$. The differential susceptibility is determined from the model with the given initial condition on $\mathbf{M}$ and $\mathbf{H}$ such that $\overline{\overline{\chi}}^{d,0} = \overline{\overline{\chi}}^{d}(\mathbf{M}^{-1}, \mathbf{H}^{-1})$.
2. The system matrix $\mathbf{Y}$ is computed for the linear problem.
3. For $k = 0, ..., n$
   i. The material term $\mathbf{Y}^{\chi^d}$ is filled using $\left(\overline{\overline{\chi}}^{d,k}(\vec{r})\right)^{-1}$.
   ii. The solution for $\delta \mathbf{M}^{k+1}$ with excitation $\delta \mathbf{H}^{s,k+1}$ is found using (64) which is then used to update $\mathbf{M}^{k+1}$ and $\mathbf{H}^{k+1}$.
   iii. Using the solution to the current iteration, the differential susceptibility is updated for the next iteration such that $\overline{\overline{\chi}}^{d,k+1} = \overline{\overline{\chi}}^{d}\left(\mathbf{M}^{k+1}, \mathbf{H}^{k+1}\right)$.

A very convenient aspect of this solver is that the system matrix which is computed initially for the linear problem only needs to be filled once. At each step in the nonlinear solver the material term is re-computed, so only the block-diagonal of the system matrix changes.

3.2.1 Magnetostrictive Material Model

As previously mentioned the transient solver is formulated to handle nonlinear hysteretic materials, but a suitable material model must be implemented. Commonly used models include the Jiles-Atherton model [24, 25], the Preisach model [26], and the Cooperative model [27]. For the simulations performed in this work, a magnetostrictive hysteresis model based on the cooperative model is used. The model was formulated based on the physics observed from experimental results and assuming that the magnetization could be formulated in terms of the cooperation of multiple physical phenomenon. Reverse magnetostriction effects, or magnetization induced by an applied stress, are incorporated by a superposition of irreversible 90-degree Brown domain walls and Bozorth stress which can be expressed as [28]

$$d\vec{M} = \begin{cases} \chi_{\text{rev}}\chi_{\text{den}} \cdot \vec{M} \cdot \dfrac{|d\sigma|}{\sigma_r}\left[f_{90}^{+} + \dfrac{4}{3} f_\sigma \left(\dfrac{\mathrm{X}_i H_c}{M_s \chi_r} + \dfrac{|\vec{M}|}{M_s} \right) \cdot \text{sign}(d\sigma) \right], & \text{on the virgin curve} \\ \chi_{\text{rev}}\chi_{\text{den}} \cdot \vec{M} \cdot \dfrac{|d\sigma|}{\sigma_r}\left[0 + \dfrac{4}{3} f_\sigma \left(\dfrac{\mathrm{X}_i H_c}{M_s \chi_r} + \dfrac{|\Delta\vec{M}|}{2M_s} \right) \cdot \text{sign}(d\sigma) \right], & \text{after an extremum in } \sigma \end{cases} \tag{65}$$

where

$$f_{90}^{+} = \frac{f_{90}}{2} = \frac{1}{2+\sqrt{2}} \tag{66}$$

represents the irreversible Brown stress, and

$$f_\sigma = \frac{3}{e^{\sigma/\sigma_r} + 2} \tag{67}$$

describes the changes in the domain structure due to stress where σ_r is the residual stress. $\vec{M}$ is the local magnetization vector, $\Delta\vec{M}$ is the change in $\vec{M}$ since the last stress reversal, X_i is the initial stress, H_c is the coercive field, M_s is the saturation magnetization, $\chi_{rev} = 1 - \left(\frac{\vec{M}}{M_s} \right)^2$ is the isotropic polycrystalline texture, and $\chi_{den} = (\chi_{rev})^2$ is the denucleation factor. In this work material constants for high tensile steel were used as follows: $X_i = 68$, $\sigma_r = 100\,\text{MPa}$, $H_c = 720\,\text{A/m}$, and $M_s = 1.66 \times 10^6$ A/m.

If the simulation includes stress, an additional stress update routine is called at the beginning of step 3 of the transient solver outlined in section 3.2, before the material term of the system matrix is filled. The procedure is as follows:

1. The change in magnetization $\delta\mathbf{M}^{k+1/2}(\mathbf{M}^k, \sigma^k, \delta\sigma^k)$ due to stress is computed using the material model, where σ is the total stress.
2. The induced magnetization is updated such that $\mathbf{M}^{k+1/2} = \delta\mathbf{M}^{k+1/2} + \mathbf{M}^k$.
3. The change in the magnetic field is computed as $\delta\mathbf{H}^{k+1/2} = \left(\overline{\overline{\chi}}^{d,k} \right)^{-1} \delta\mathbf{M}^{k+1/2}$.
4. The magnetic field is updated such that $\mathbf{H}^{k+1/2} = \delta\mathbf{H}^{k+1/2} + \mathbf{H}^k$.

Note that the stress updates occur at intermediate time steps which are denoted by the superscript $k+1/2$. When the field is subsequently updated after the stress, values at this intermediate step are now used instead of the previous step k.

3.3 Dynamic Stress Analysis with LS-DYNA

LS-DYNA is a multi-physics simulation software package which can compute the stresses in the ship's hull due to the wave pressure. Initially developed for highly nonlinear, transient dynamic finite element analysis using explicit time integration [7], the software now contains an implicit time integration scheme which is used in this work. At each time step the nonlinear problem is solved using the implicit integration scheme which allows for a larger time step to be used in the simulation. This is important as the size of the time step used in LS-DYNA is set by the ship motion simulation time-step. For the size of the problems in this project, it was observed that the actual simulation time using the nonlinear solution was comparable to using the linear solution.

Initially in the ship motion code described in Chapter 2, the linear hexahedral mesh is written to an LS-DYNA input file. At each subsequent time step the pressure on the face of each element is written to that same file. This includes only the restoring and the Froude-Krylov pressures as they are computed for each face on the hull's exterior at every time step. The radiation and diffraction forces are currently not included in the dynamic stress analysis since they are computed as net forces and moments acting on the entire body rather than a pressure acting on the face of each finite element. Although this approach will not capture the total stresses in the hull, the restoring and Froude-Krylov pressures were seen to be the dominant forces, so the introduced error is not expected to be large.

An example illustration of the effective stresses in the hull of the S-175 computed with LS-DYNA is shown in Figure 19. The Von Mises effective stress is the equivalent uniaxial stress that would have the equivalent distortion energy as the actual applied stresses [29]. In the LS-DYNA simulation a boundary condition is placed on each of the

nodes along the top edge in order to prevent rigid body motion. This however will add some error to the predicted stress in the hull. As a result, some stress can be seen along the top edge of the ship which is not a direct result of the fluid pressure as this area is above the water level.

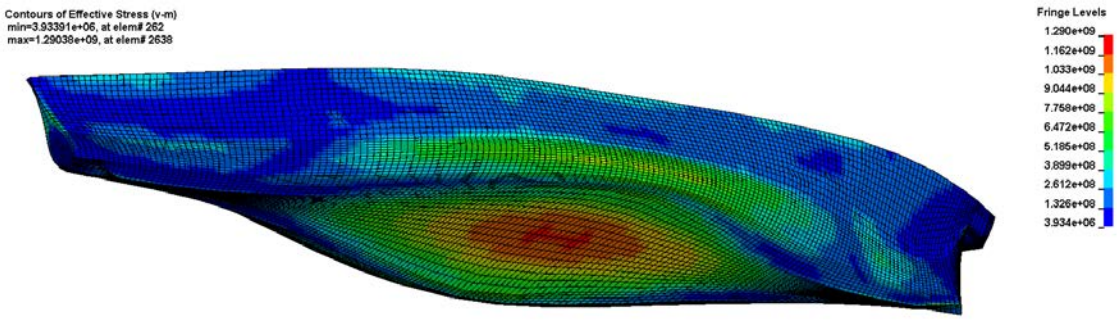

Figure 19. Example of the effective stress in the hull of the S-175 computed with LS-DYNA

3.4 Results

Motion of the box ship described in Table 1 was simulated for ship headings of 0, 45, and 90 degrees using a 10 cm wave with period of 7.5 s and results are plotted in Figures 20-21. The wave induced pressure was then used to compute the hull stresses using LS-DYNA as described in section 3.3. Finally a magnetic field excitation was applied in the positive x-direction of the global frame which was linearly ramped from 0 A/m to 20 A/m over 5 seconds, and then held constant for the remainder of the simulation. The scattered field was computed at discrete points along a line 2 m below the bottom of the ship at y = 0 in the body-fixed frame. This was performed first without including the motion and hull stresses to get reference values at each point, and then repeated to include the motion and stress. Using the computed reference data, the relative change in the field due to motion and stress at each point was computed as

$$B_{i,rc} = \frac{B_i - B_{i,ref}}{\max\left(\left\|\mathbf{B}\right\|_2\right)}, \quad i = x, y, z \tag{68}$$

where $\mathbf{B}$ is the magnetic flux density vector at each point.

The relative change in the magnetic field computed according to (68) for the box ship with 0 degree heading is shown in Figure 23 where several instances in time throughout the third wave period once the ship motion has reached steady state are plotted. In this configuration, the ship should look like a magnetic dipole with the bow being positively charged and the stern being negatively charged. This explains the antisymmetric nature of B_z as well as B_x being fairly constant through the mid-section of the ship before quickly reversing sign at both ends. The results for the ship with 45 degree heading are shown in Figure 24 and the case of a 90 degree heading is shown in Figure 25. As the ship

heading angle is increased, the port side will become more negatively charged, while the starboard side becomes more positively charged. The response of B_y in Figure 24 shows that the scattered field beneath the ship is starting to be directed from the starboard to port side. At a heading of 90 degrees the magnitude of B_y is even larger while B_x and B_z are negligible as expected. It should be noted that while large relative changes in B_x and B_z are seen in Figure 25, these components are actually three orders of magnitude smaller than B_y. All three of these cases show that the wave induced motion of the ship is periodic with the wave which results in the relative changes in the magnetic field also being periodic. Since the magnetic field varies periodically with the same period as the wave, only results for one wave period are presented.

The magnetic field as a function of time at the point (0,0,-4m) for a 0 degree heading and 10 cm wave amplitude is shown in Figure 26. Each of the three components of the field is normalized by the maximum of that particular component. With this ship orientation, and no motion or induced stress, it is expected to see the scattered field purely in the negative x direction at this particular probe point. Due to integration tolerances the y component is observed to have some non-zero value, although the field in this direction is three orders of magnitude smaller than the x component. The periodic nature of this component is likely a result of reverse magnetostriction due to the stresses in the hull which are periodic once the ship reaches steady state. A much larger change is seen in the z component which is caused by the induced pitching motion of the ship thus the excitation field direction is time varying. The results for a 45 degree heading are shown in Figure 27 where a small increase in the x and y components are noticed as time progresses. Close

inspection of Figure 21 shows a small amount of yaw motion which explains these results. Whereas the rudder of a real ship provides a counteracting force to maintain a constant heading, the motion code does not implement a maneuvering model or rudder forces which may be the cause of the additional yaw motion. Figure 28 shows the normalized field versus time for a 90 degree ship heading. As expected for this orientation, the y component is dominant and is three orders of magnitude larger than both the x and z components.

The same procedure was repeated for the box ship with a much larger wave amplitude of 50 cm and the induced motion is also shown in Figures 20-21. The larger wave results in very similar ship motion with the magnitude of the response being scaled. As expected, the same scaling effect observed in the motion is also seen in the relative change in the magnetic field for the 0 degree heading and the 90 degree heading shown in Figure 29 and Figure 31, respectively. However, the 45 degree heading shown in Figure 21 is seen to have a noticeable amount of motion in yaw. Once again, adding rudder forces and a maneuvering model to the motion code could drastically improve these results. Due to the yaw motion not being periodic with the wave period in this case, the relative changes in the magnetic field in Figure 30 are not periodic as previously observed in the other cases.

Next, the motion of the S-175 was simulated for headings of 0, 45, 90, 135, and 180 degrees with a 10.5 second period wave and two amplitudes: 1 meter and 2 meters. The results are plotted in Figures 32-35. The roll motion for the 45, 90, and 135 degree headings never reached a steady-state periodic response. This could be caused by several issues. First, due to the previously discussed lack of rudder forces, some yaw motion is observed. A larger contributor may be that the empirical model for viscous roll damping was implemented without the bilge-keel factor which should contribute significantly to

stabilizing the roll motion. Finally, the mesh for the S-175 only includes the hull 1.5 m above the still water line which may introduce additional error for the results of the 2 m wave.

The relative changes in the magnetic field at discrete points along a line 9.5 m below the bottom of the S-175 at y = 0 m were computed according to (68). These computed changes in the field are shown for several instances in time for the third wave period in Figures 37-40 for the 1 m amplitude wave and in Figures 42-45 for the 2 m wave. For the ship headings of 0 and 180 degrees, the changes in the field are periodic as previously observed since the ship motion is also periodic. Again, a larger wave height induces more stress in the hull as well as a larger motion response, thus the relative changes in the magnetic field are similar but with a larger scale. In comparison to the plots for the box ship, it is observed that the field is no longer symmetric about the center line. Not only is the S-175 asymmetric from bow to stern, the longitudinal center of gravity which is at zero on the x-axis of all figures is 2.34 m aft of mid ship. Looking at the changes in the field for the ship with 45 degree heading, some symmetry is observed in comparison to the 135 degree heading for the 1 m wave amplitude, however this does not occur for a 2 m wave due to the large roll motion that is developed. The x components of the field are 180 degrees out of phase with each other since the incident field has a component in the positive x direction for the 45 degree heading but has a component in the negative x direction for 135 degrees. The same effect is observed between the 0 degree and 180 degree headings. Again it should be noted that while a relative change in B_x and B_z are observed for the 90 degree heading, both of these components were three orders of magnitude smaller than B_y as expected.

Finally the box ship was simulated with a forward speed of 10 knots, a heading of 0 degrees, and a 50 cm wave with 7.5 s wave period. The motion history of the ship in this case is shown in Figure 47. According to (34), the encounter period is 5.21 s and it is observed that the ship's motion oscillates at this encounter period rather than the wave period. The relative changes in the magnetic field are shown in Figure 48 for several times within the third wave period while Figure 49 shows the same data but at several times within a single encounter period. When the ship had zero speed, the field is seen to be periodic with the wave period, however, the effect of forward speed is that the field oscillates at the encounter period.

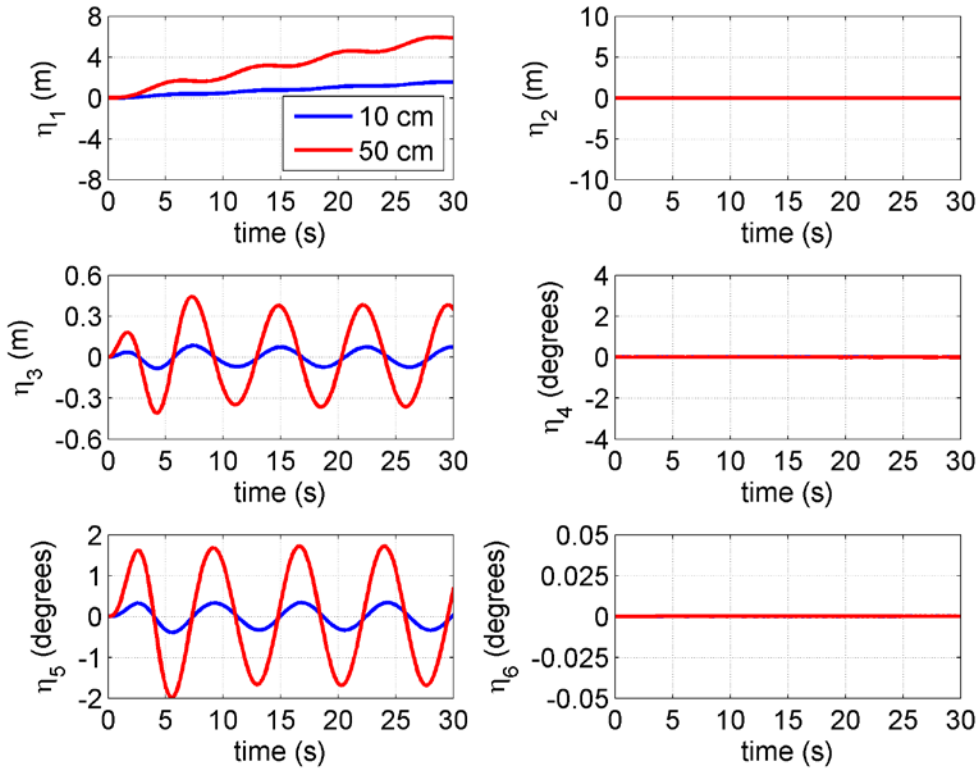

Figure 20. Comparison of the motion of the box ship with 0 degree heading for two different wave amplitudes each with the same 7.5 s period.

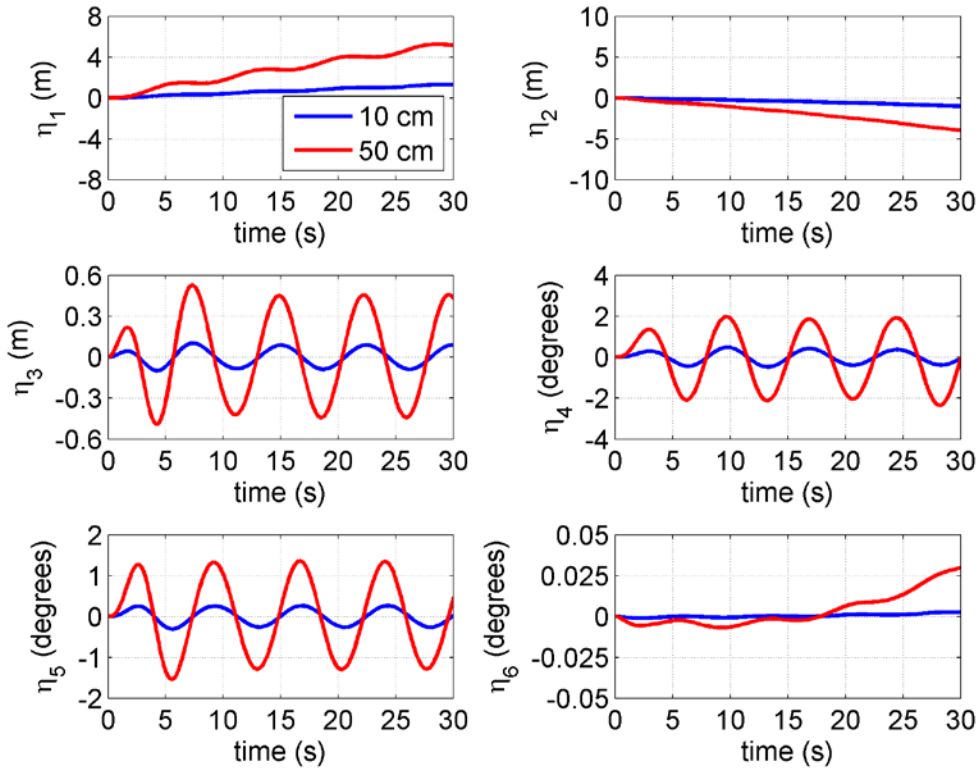

Figure 21. Comparison of the motion of the box ship with 45 degree heading for two different wave amplitudes each with the same 7.5 s period.

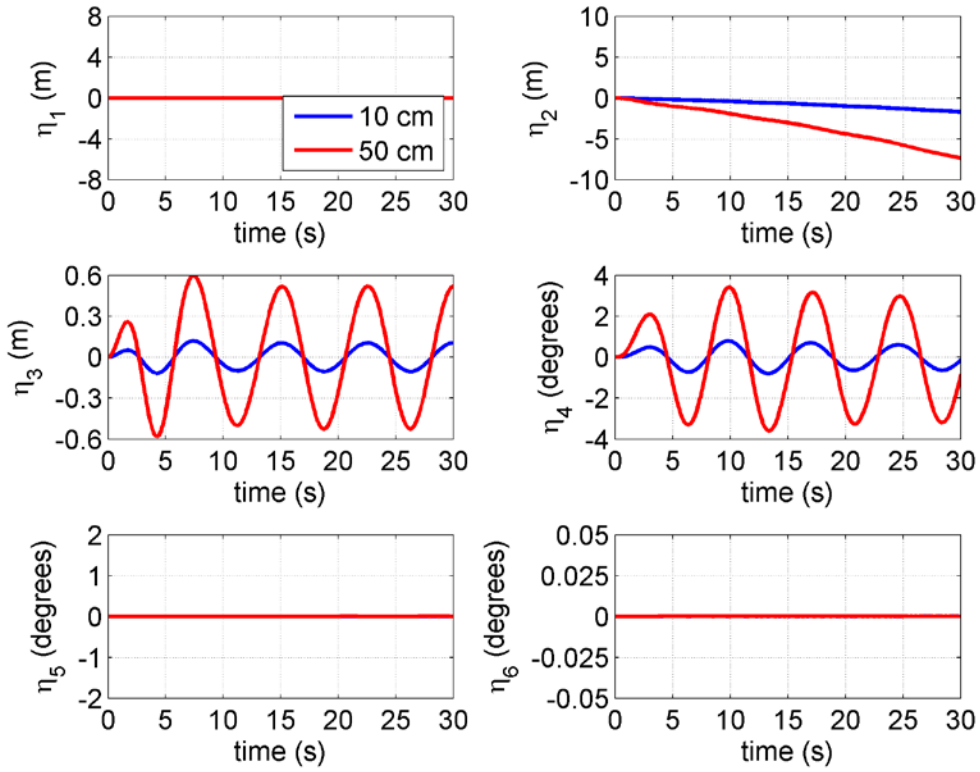

Figure 22. Comparison of the motion of the box ship with 90 degree heading for two different wave amplitudes each with the same 7.5 s period.

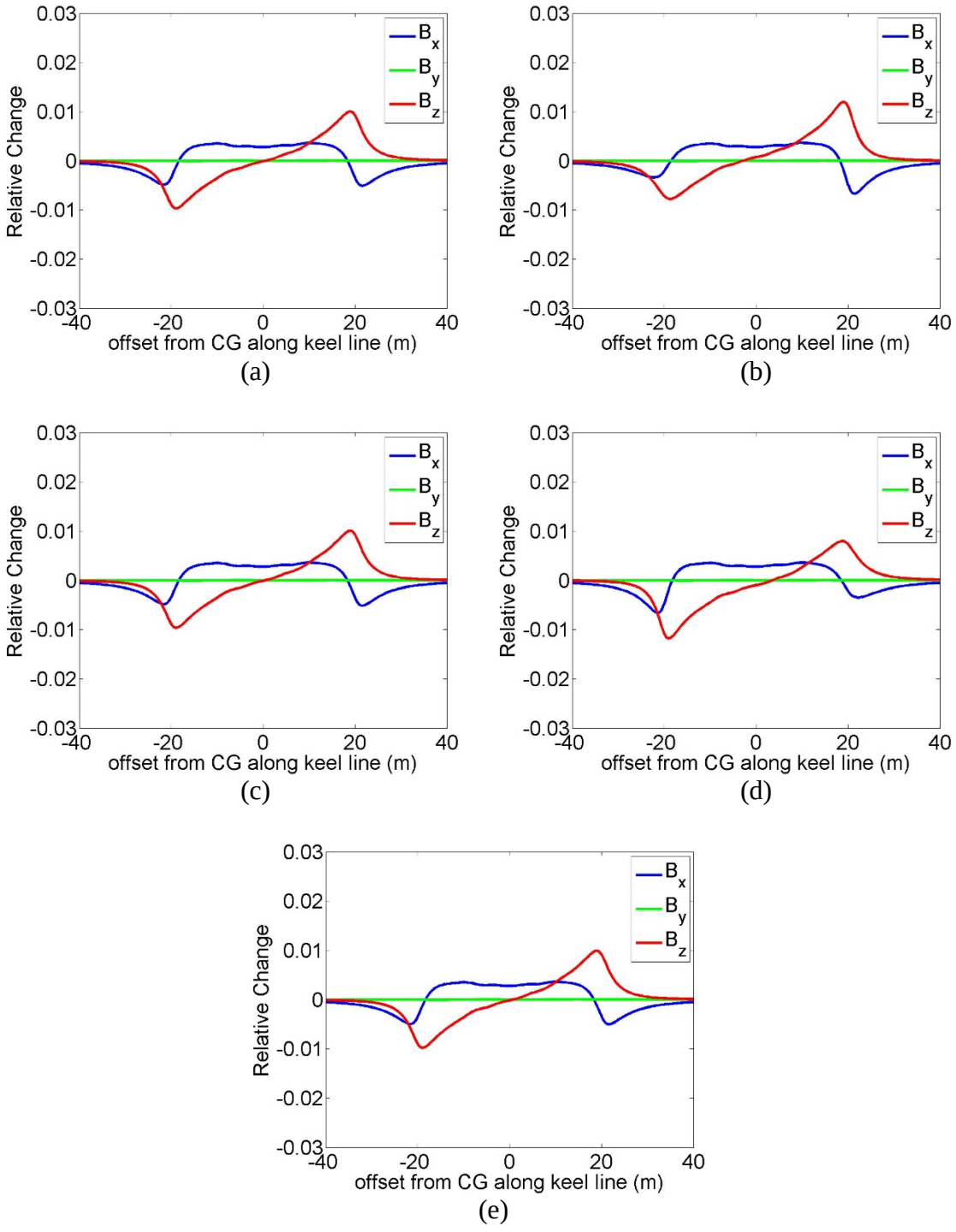

Figure 23. Relative change in the magnetic field along a line 2 m below the box ship at y = 0 at (a) 15 s (b) 16.8 s (c) 18.6 s (d) 20.6 s (e) 22.4 s. The ship has a heading of 0 degrees and is excited by a 10 cm wave with 7.5 s period.

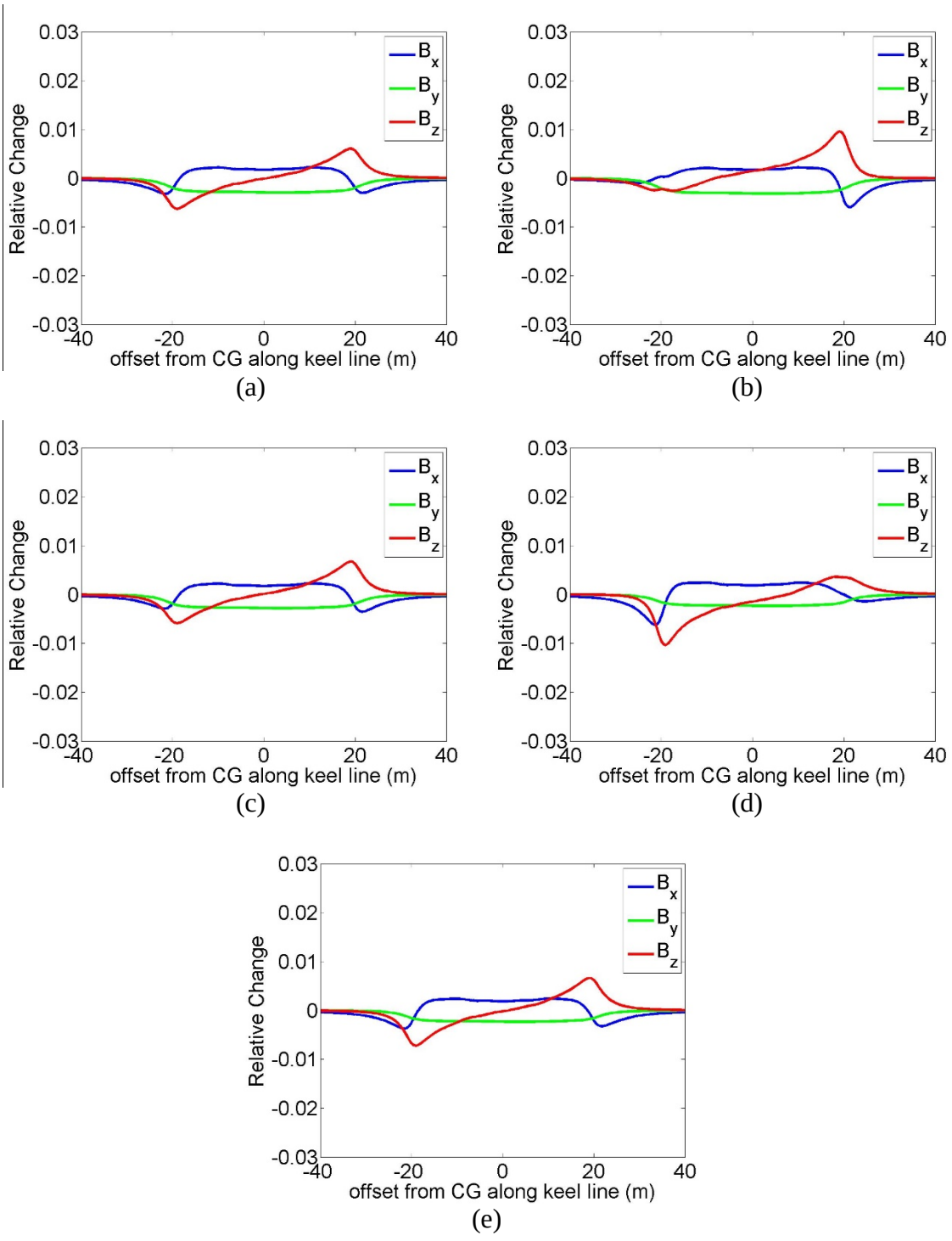

Figure 24. Relative change in the magnetic field along a line 2 m below the box ship at y = 0 at (a) 15 s (b) 16.8 s (c) 18.6 s (d) 20.6 s (e) 22.4 s. The ship has a heading of 45 degrees and is excited by a 10 cm wave with 7.5 s period.

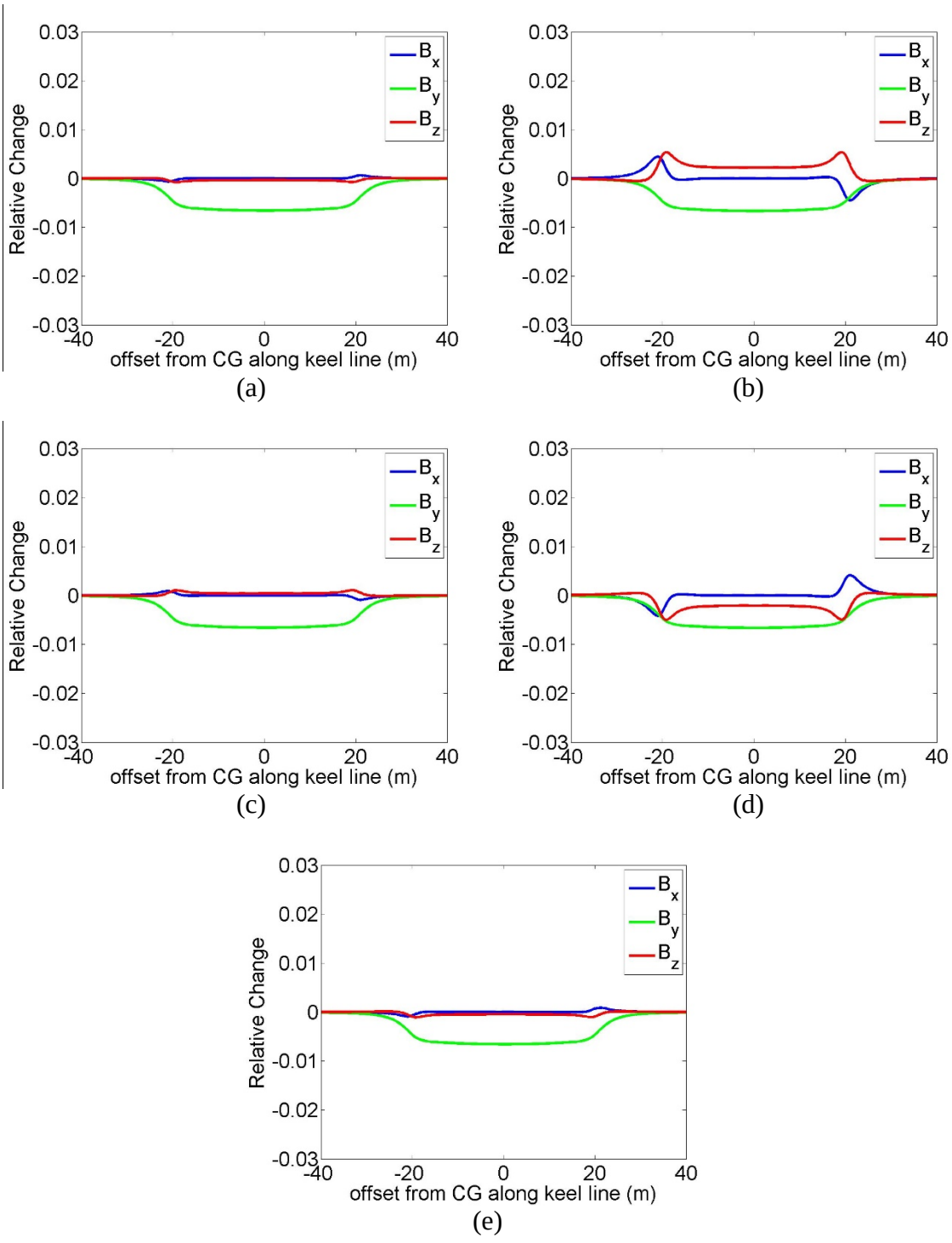

Figure 25. Relative change in the magnetic field along a line 2 m below the box ship at y = 0 at (a) 15 s (b) 16.8 s (c) 18.6 s (d) 20.6 s (e) 22.4 s. The ship has a heading of 90 degrees and is excited by a 10 cm wave with 7.5 s period.

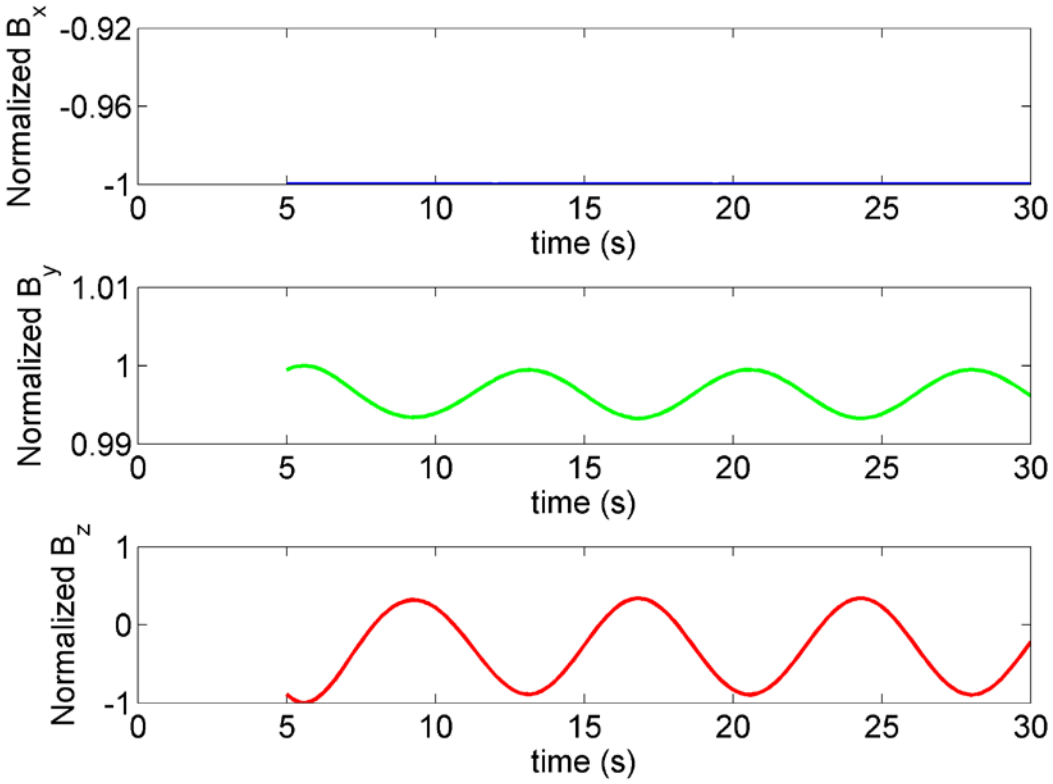

Figure 26. Normalized B-field of the box ship at the point (0, 0, -4 m). The ship has a heading of 0 degrees and is excited by a 10 cm amplitude wave with 7.5 s period. The x component is three orders of magnitude larger than the y component.

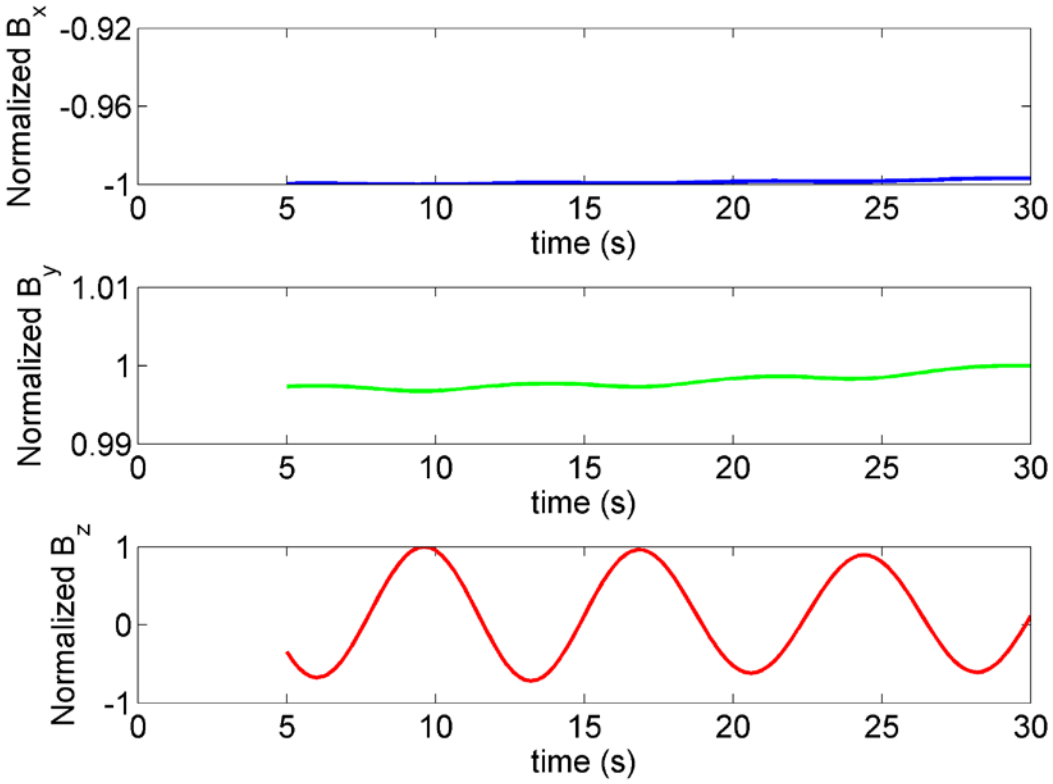

Figure 27. Normalized B-field of the box ship at the point (0, 0, -4 m). The ship has a heading of 45 degrees and is excited by a 10 cm amplitude wave with 7.5 s period. The x and y components are three orders of magnitude larger than the z component.

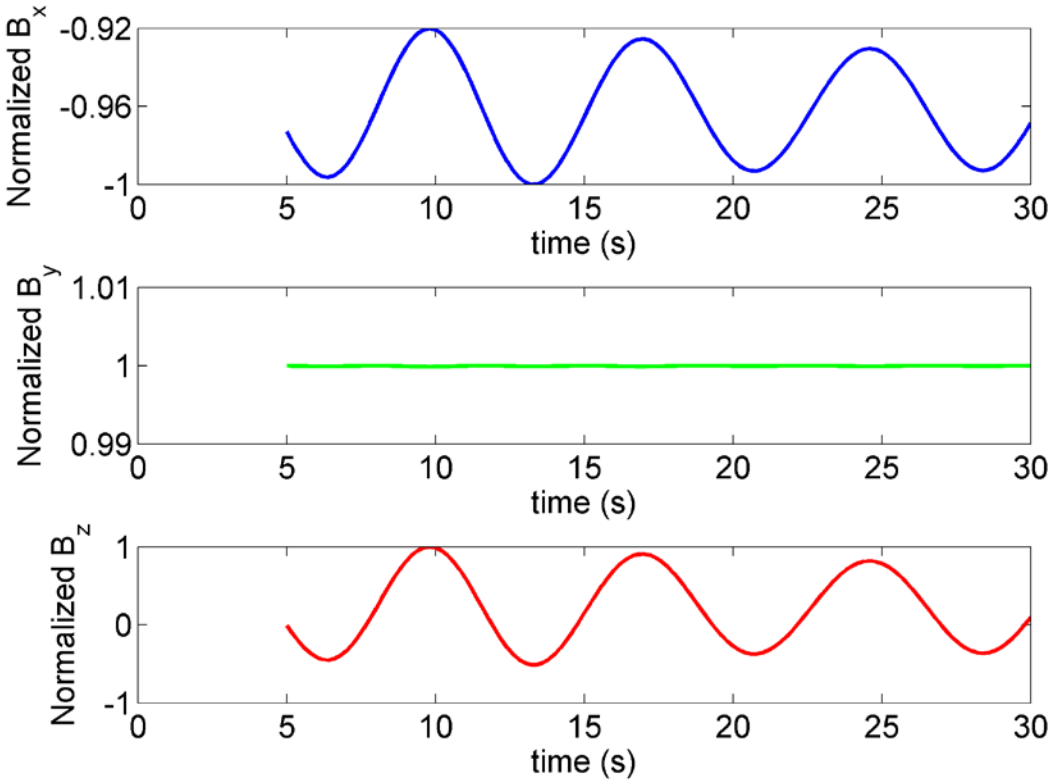

Figure 28 Normalized B-field of the box ship at the point (0, 0, -4 m). The ship has a heading of 90 degrees and is excited by a 10 cm amplitude wave with 7.5 s period. The y component is three orders of magnitude larger than the x and z components.

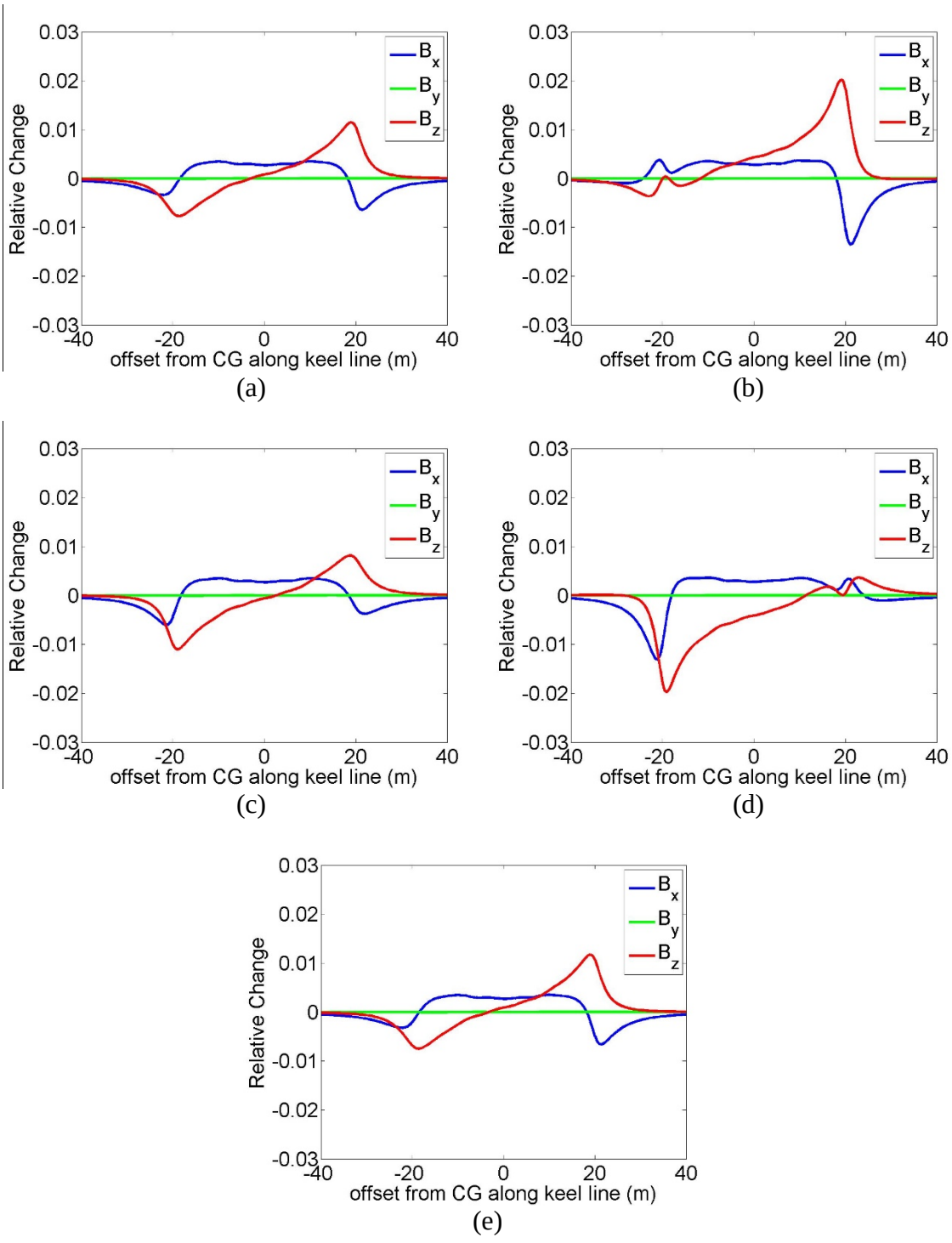

Figure 29. Relative change in the magnetic field along a line 2 m below the box ship at y = 0 at (a) 15 s (b) 16.8 s (c) 18.6 s (d) 20.6 s (e) 22.4 s. The ship has a heading of 0 degrees and is excited by a 50 cm wave with 7.5 s period.

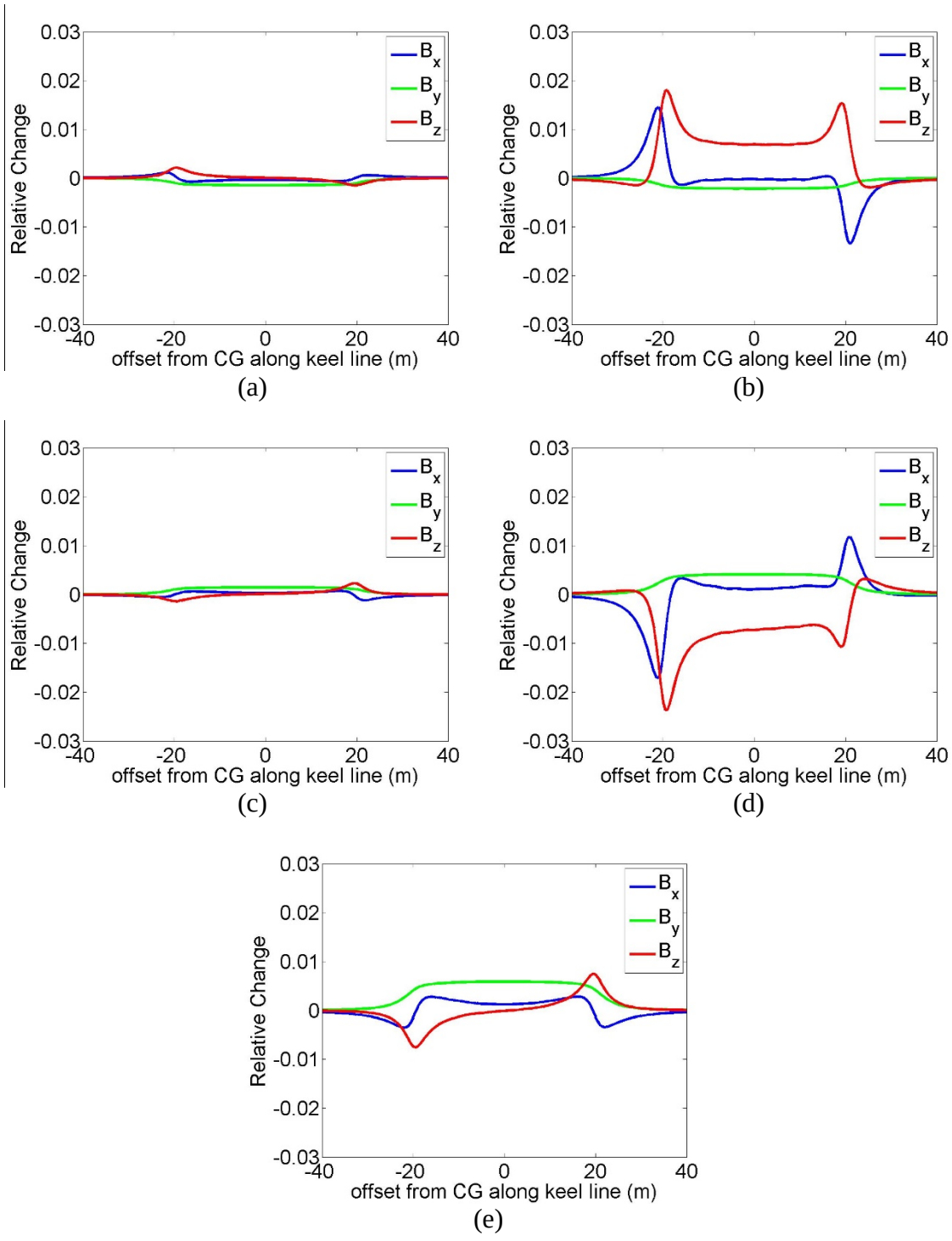

Figure 30. Relative change in the magnetic field along a line 2 m below the box ship at y = 0 at (a) 15 s (b) 16.8 s (c) 18.6 s (d) 20.6 s (e) 22.4 s. The ship has a heading of 45 degrees and is excited by a 50 cm wave with 7.5 s period.

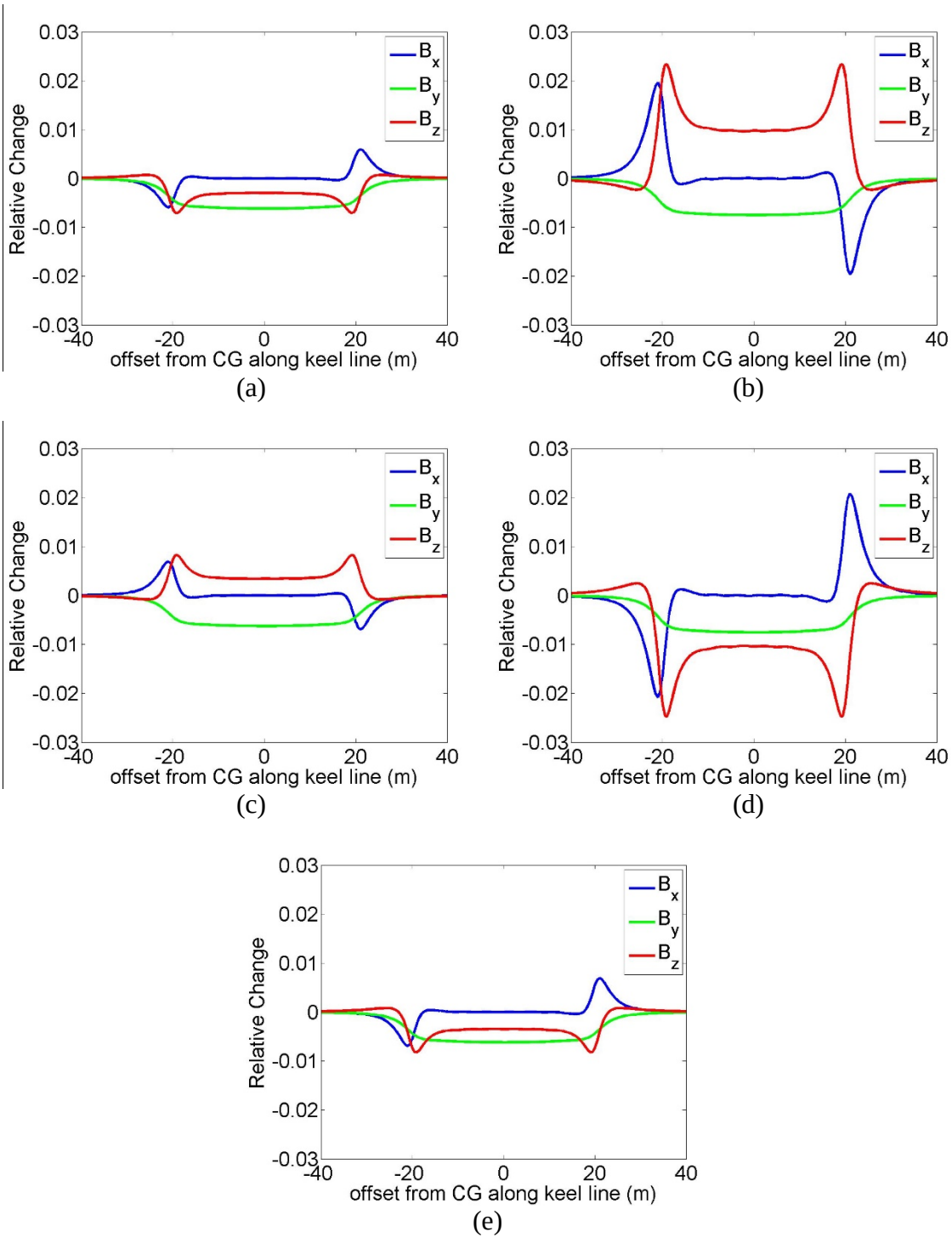

Figure 31. Relative change in the magnetic field along a line 2 m below the box ship at y = 0 at (a) 15 s (b) 16.8 s (c) 18.6 s (d) 20.6 s (e) 22.4 s. The ship has a heading of 90 degrees and is excited by a 50 cm wave with 7.5 s period.

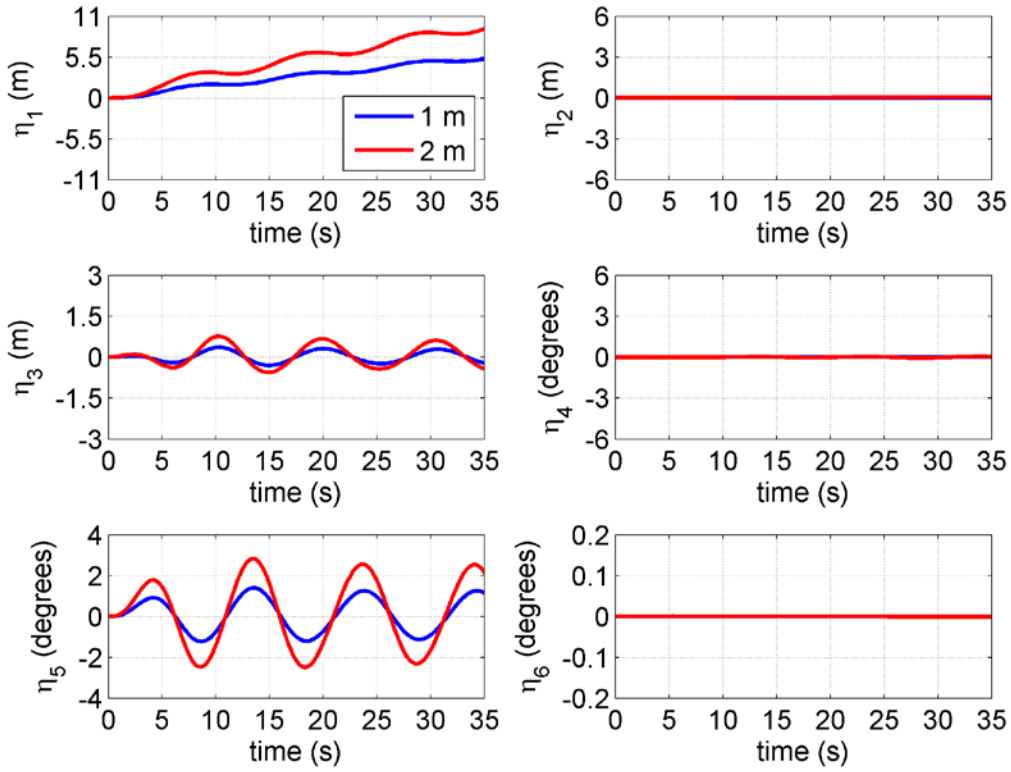

Figure 32. Comparison of the motion of the S-175 with 0 degree heading for two different wave amplitudes each with the same 10.5 s period.

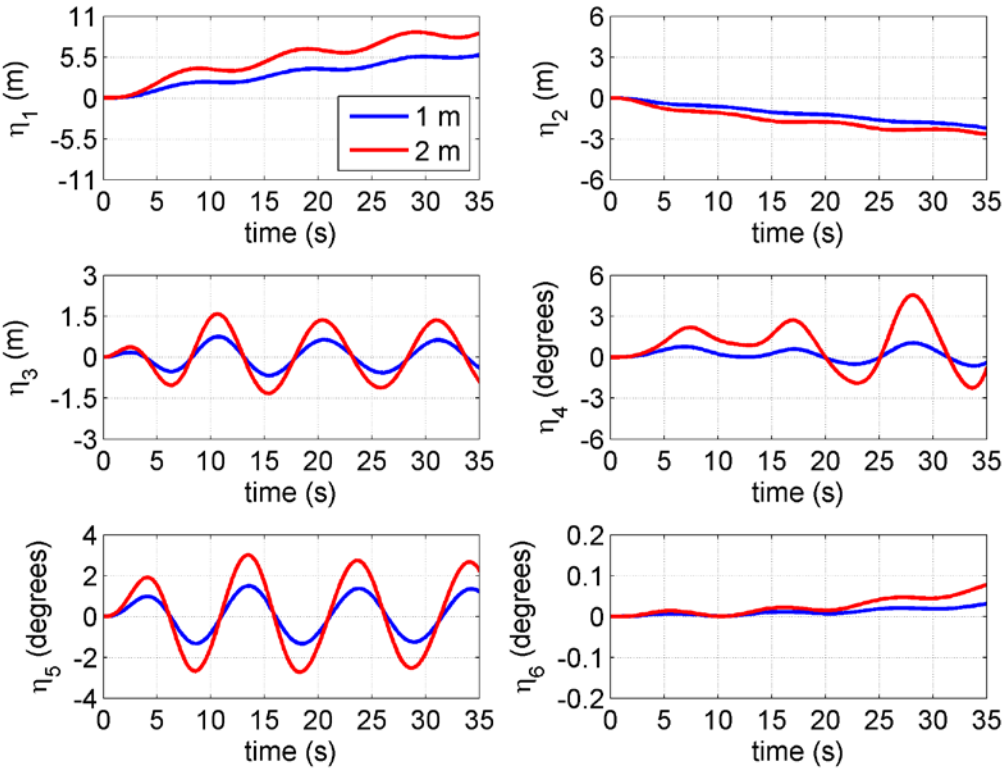

Figure 33. Comparison of the motion of the S-175 with 45 degree heading for two different wave amplitudes each with the same 10.5 s period.

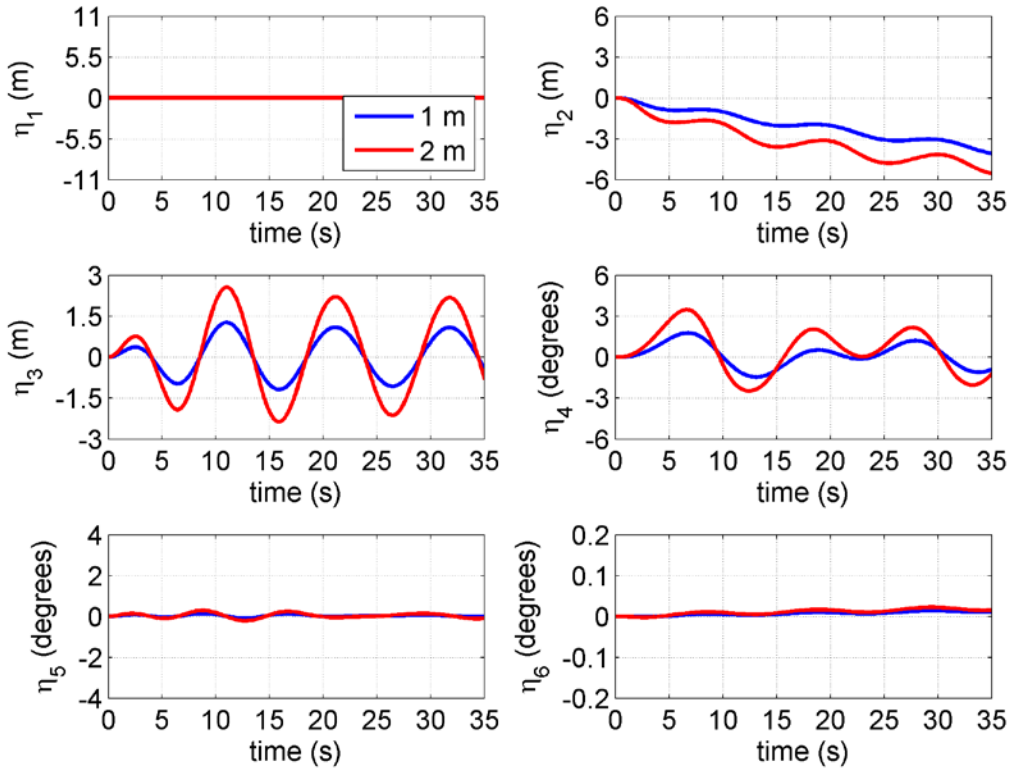

Figure 34. Comparison of the motion of the S-175 with 90 degree heading for two different wave amplitudes each with the same 10.5 s period.

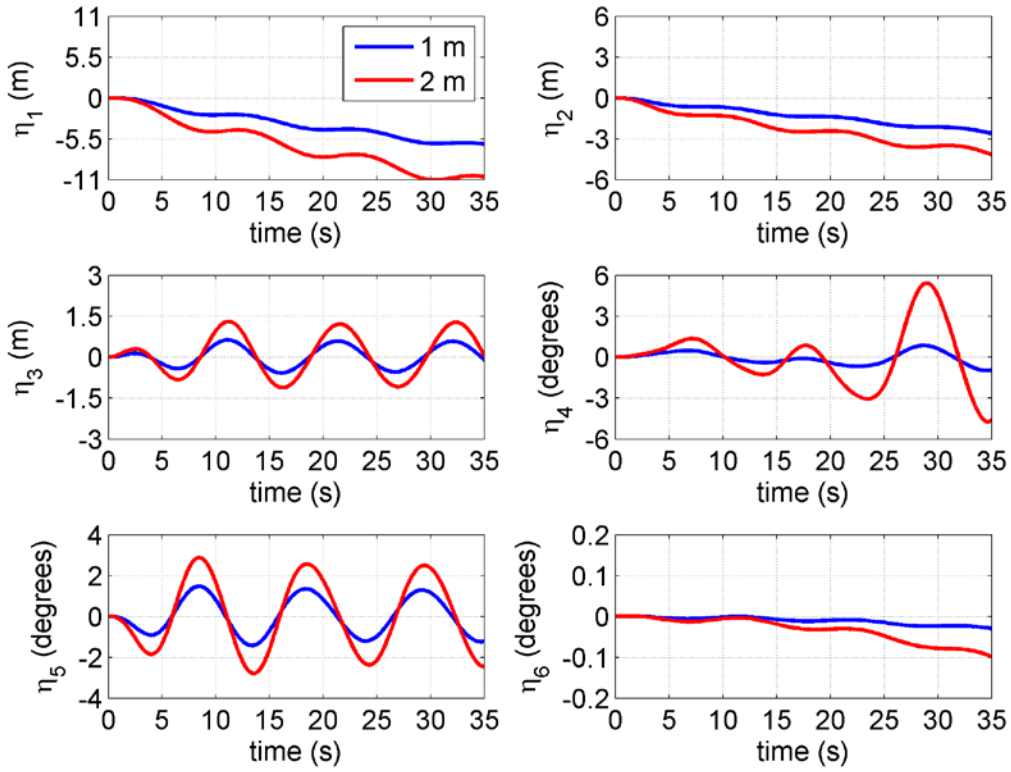

Figure 35. Comparison of the motion of the S-175 with 135 degree heading for two different wave amplitudes each with the same 10.5 s period.

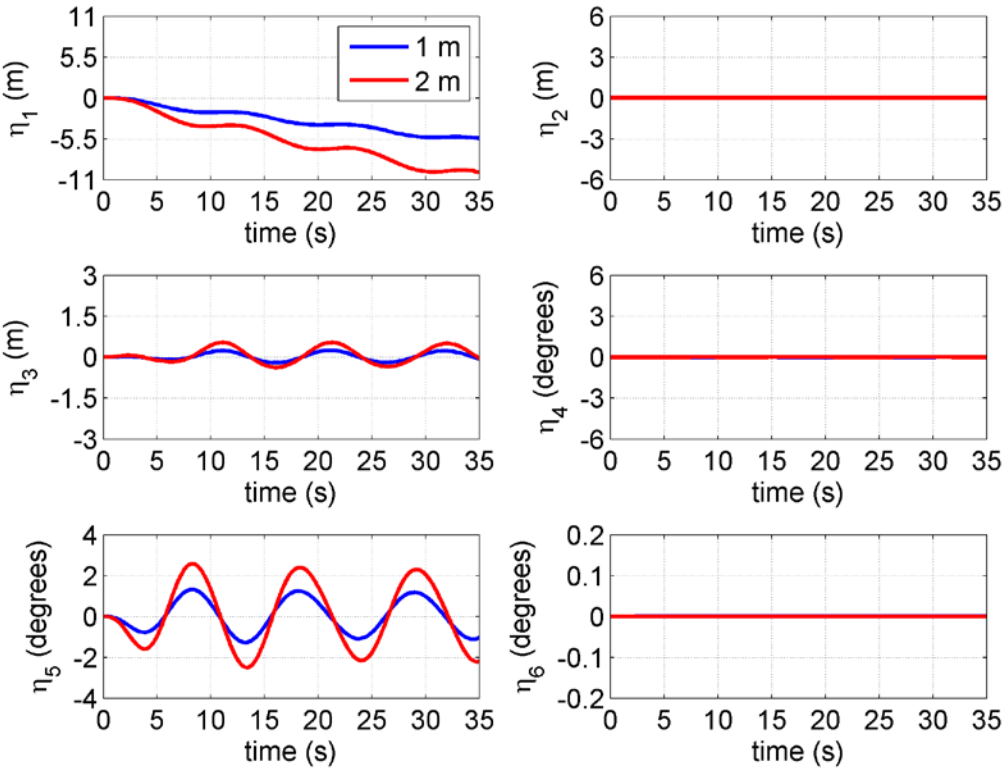

Figure 36. Comparison of the motion of the S-175 with 180 degree heading for two different wave amplitudes each with the same 10.5 s period.

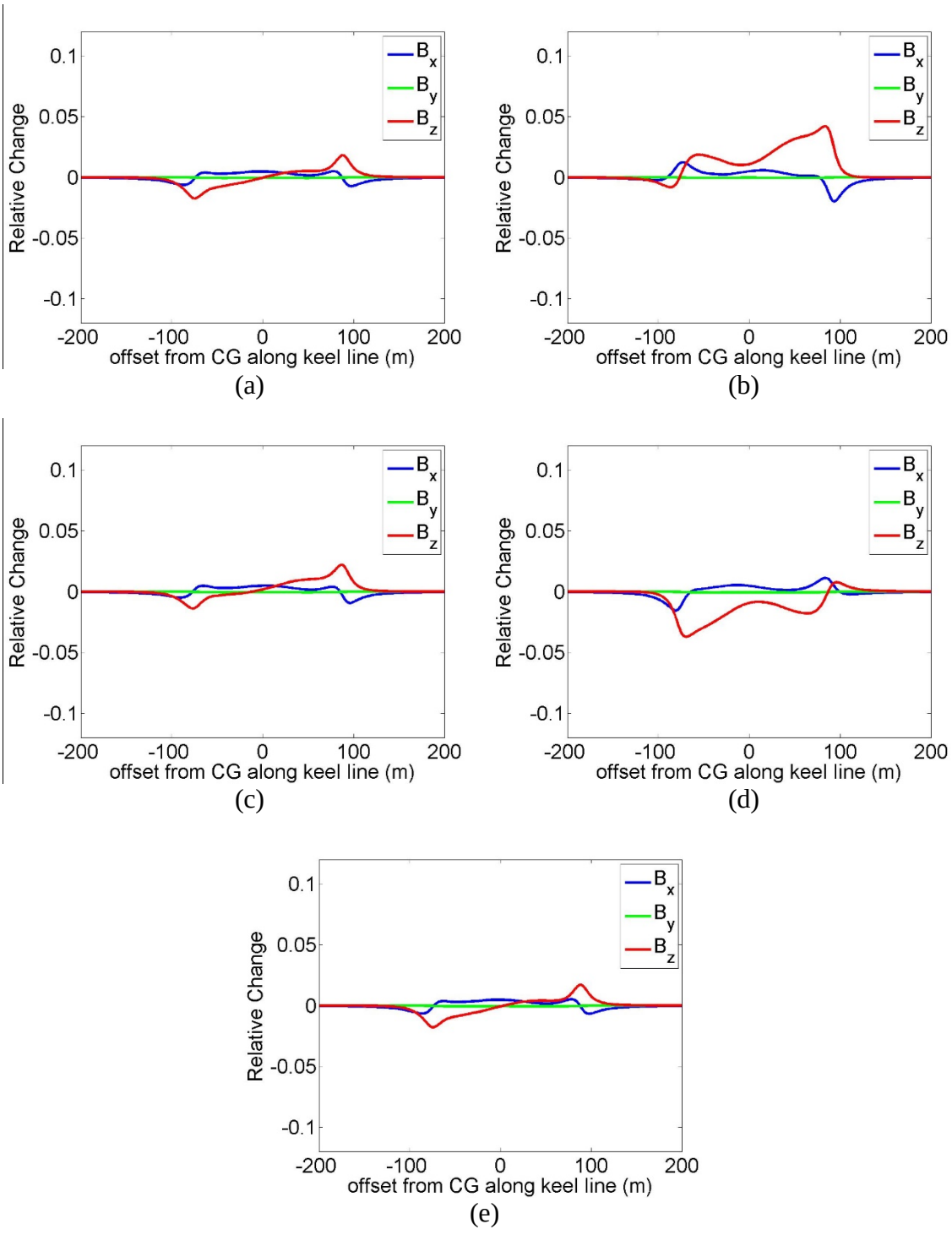

Figure 37. Relative change in the magnetic field along a line 9.5 m below the S-175 at y = 0 at (a) 21 s (b) 23.6 s (c) 26.2 s (d) 28.8 s (e) 31.4 s. The ship has a heading of 0 degrees and is excited by a 1 m wave with 10.5 s period.

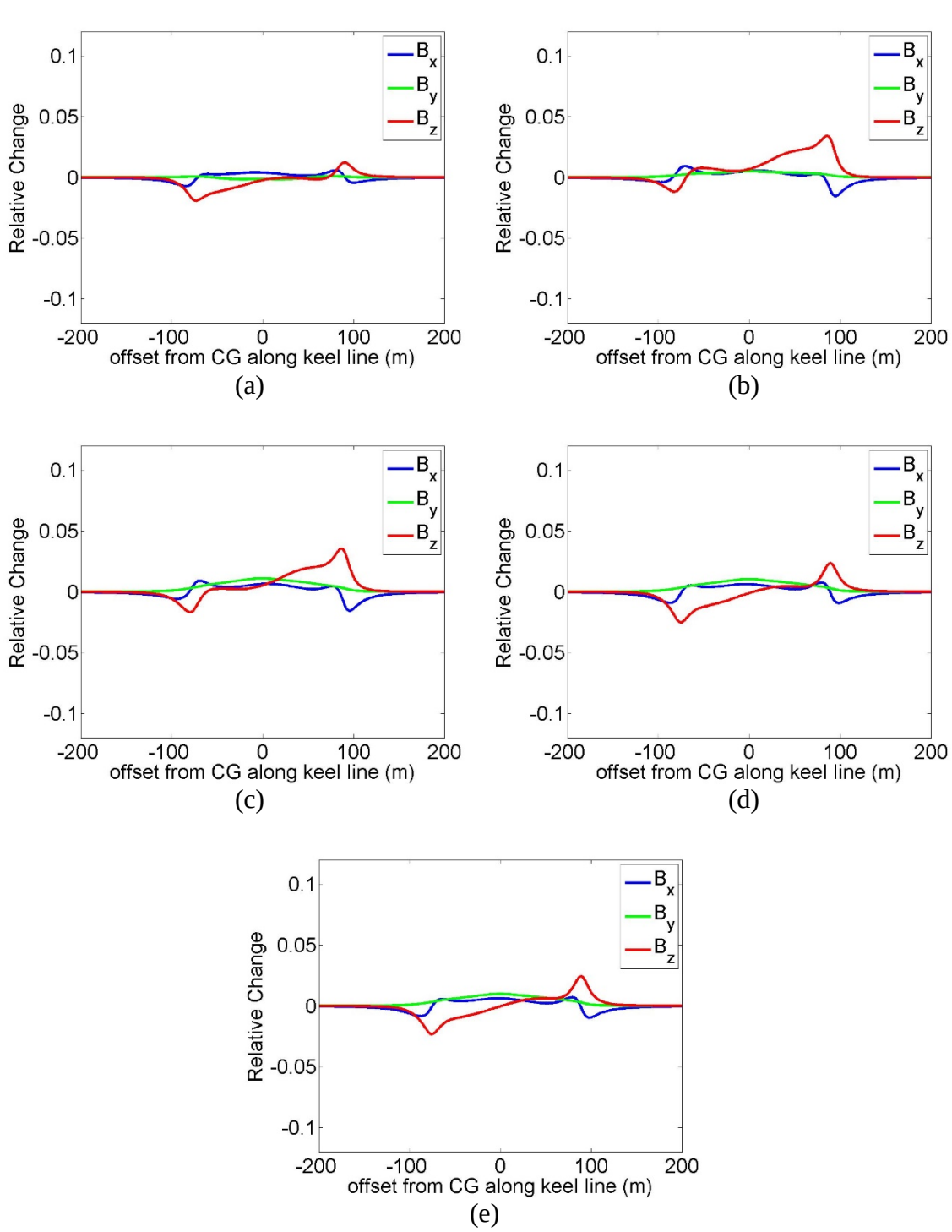

Figure 38. Relative change in the magnetic field along a line 9.5 m below the S-175 at y = 0 at (a) 21 s (b) 23.6 s (c) 26.2 s (d) 28.8 s (e) 31.4 s. The ship has a heading of 45 degrees and is excited by a 1 m wave with 10.5 s period.

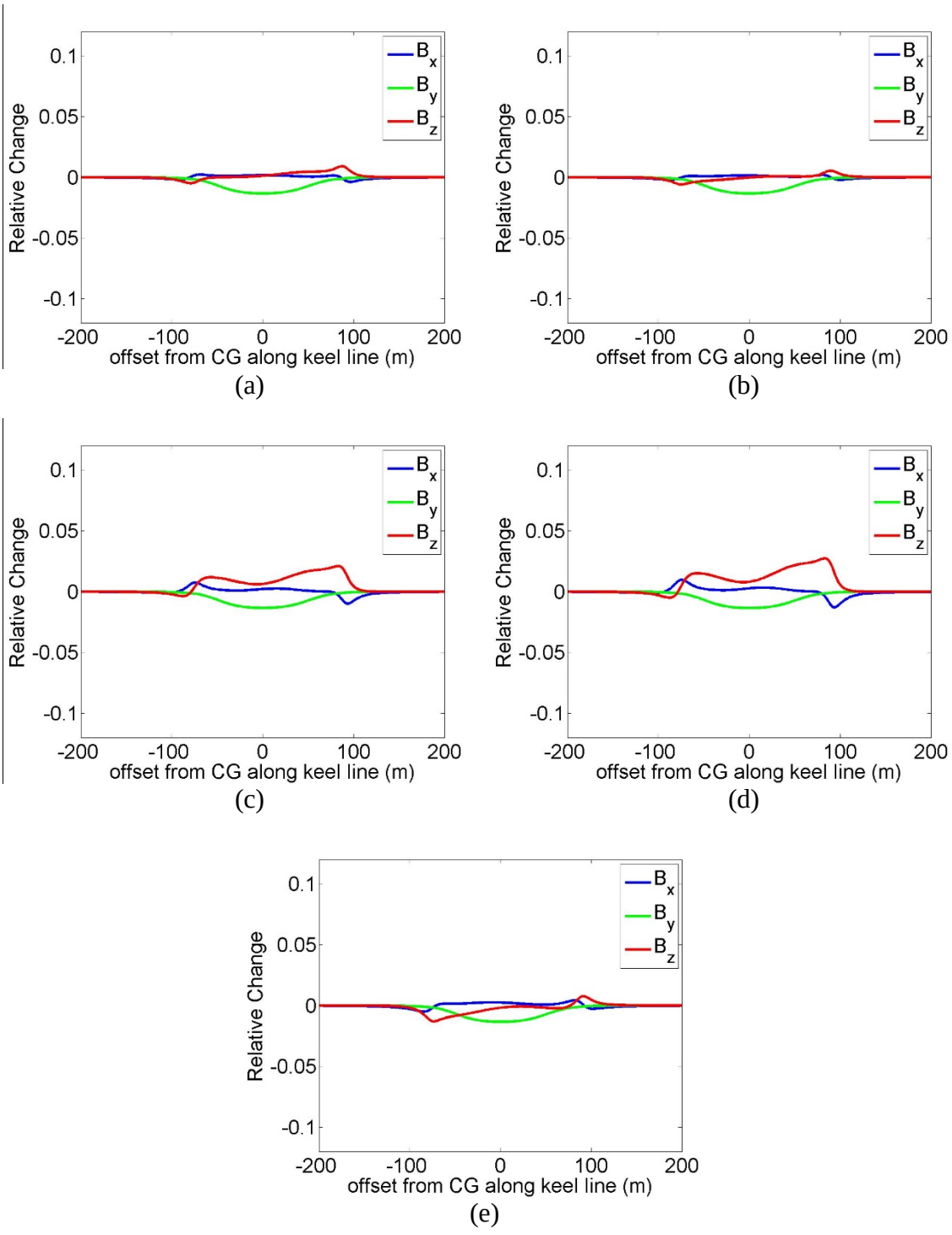

Figure 39. Relative change in the magnetic field along a line 9.5 m below the S-175 at y = 0 at (a) 21 s (b) 23.6 s (c) 26.2 s (d) 28.8 s (e) 31.4 s. The ship has a heading of 90 degrees and is excited by a 1 m wave with 10.5 s period.

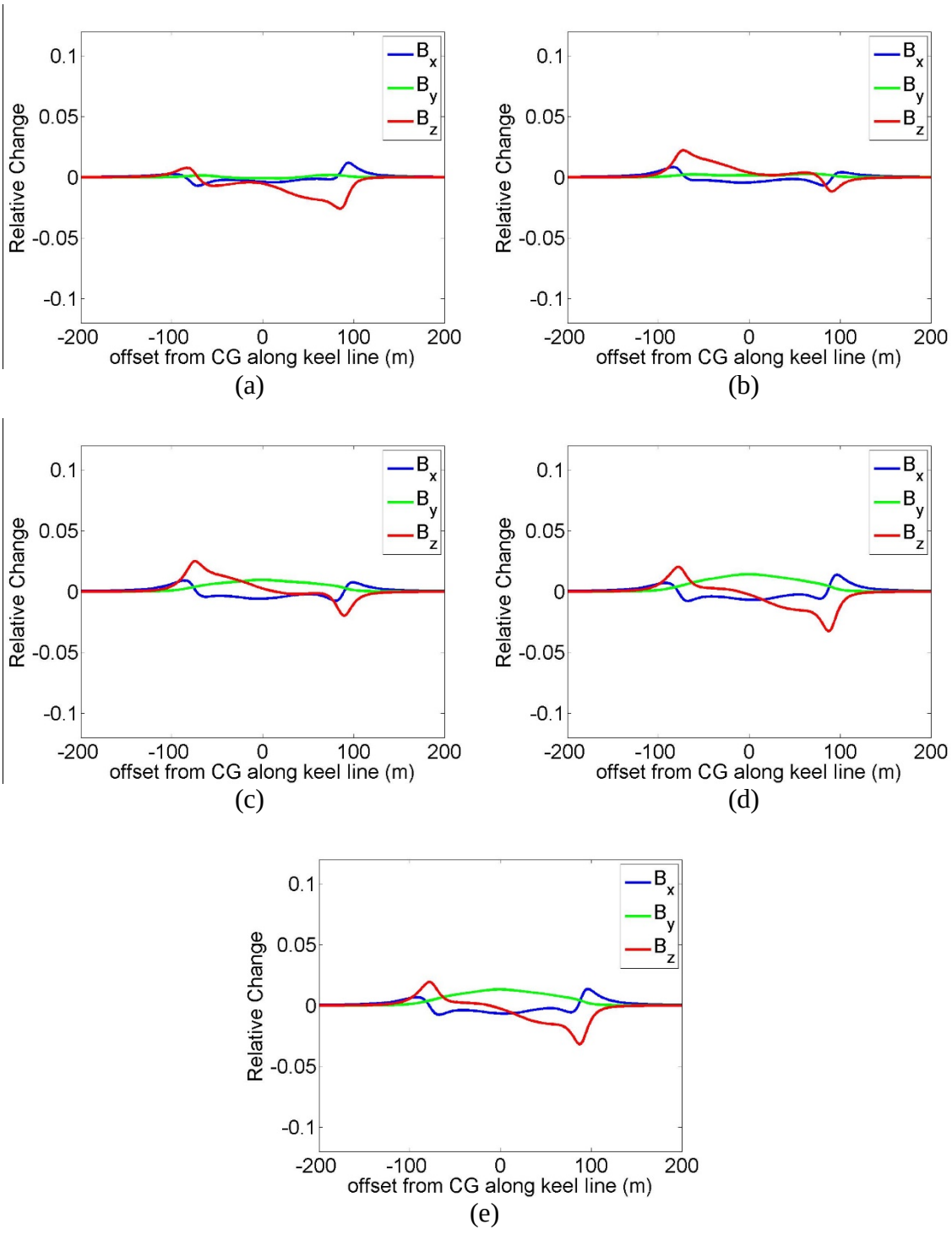

Figure 40. Relative change in the magnetic field along a line 9.5 m below the S-175 at y = 0 at (a) 21 s (b) 23.6 s (c) 26.2 s (d) 28.8 s (e) 31.4 s. The ship has a heading of 135 degrees and is excited by a 1 m wave with 10.5 s period.

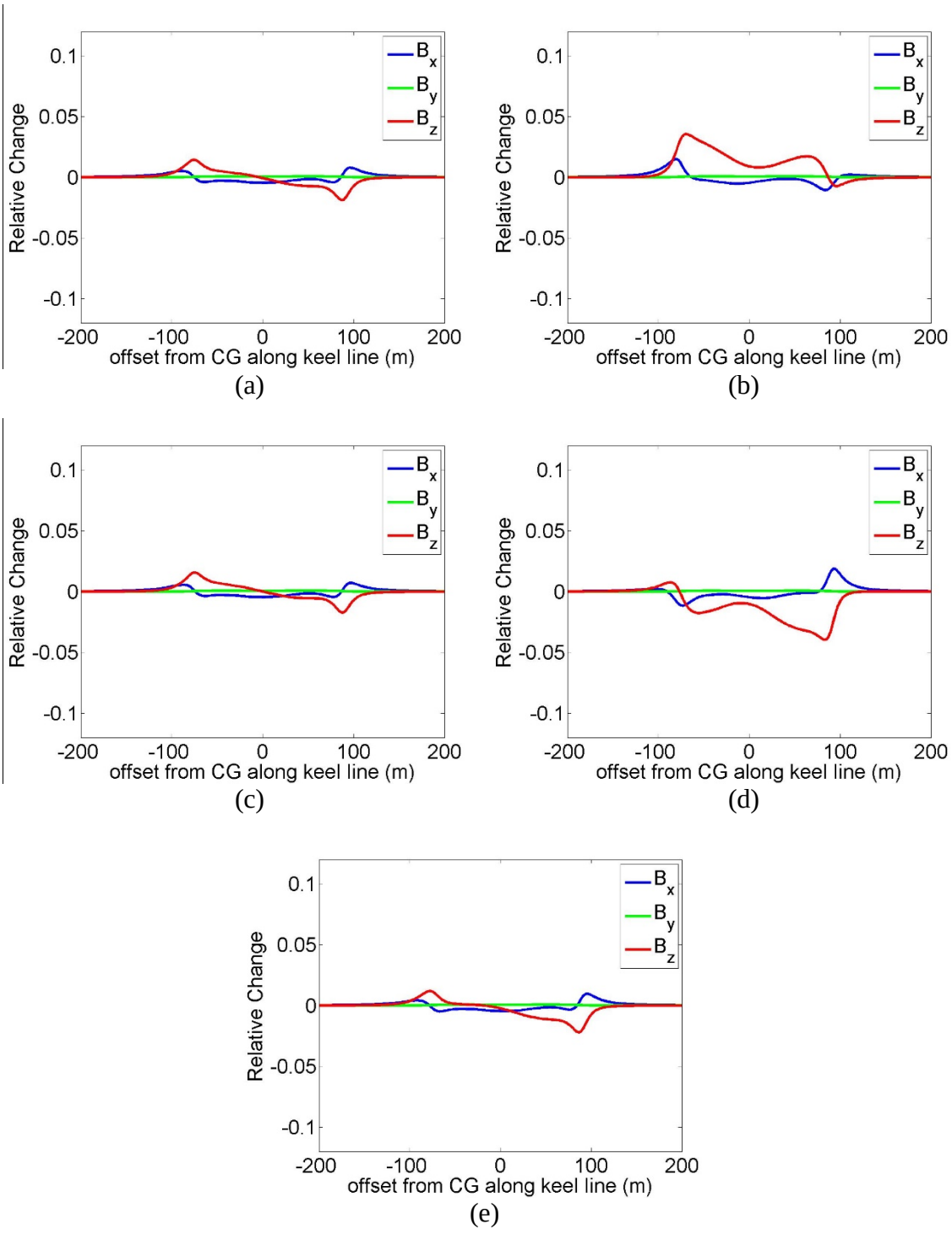

Figure 41. Relative change in the magnetic field along a line 9.5 m below the S-175 at y = 0 at (a) 21 s (b) 23.6 s (c) 26.2 s (d) 28.8 s (e) 31.4 s. The ship has a heading of 180 degrees and is excited by a 1 m wave with 10.5 s period.

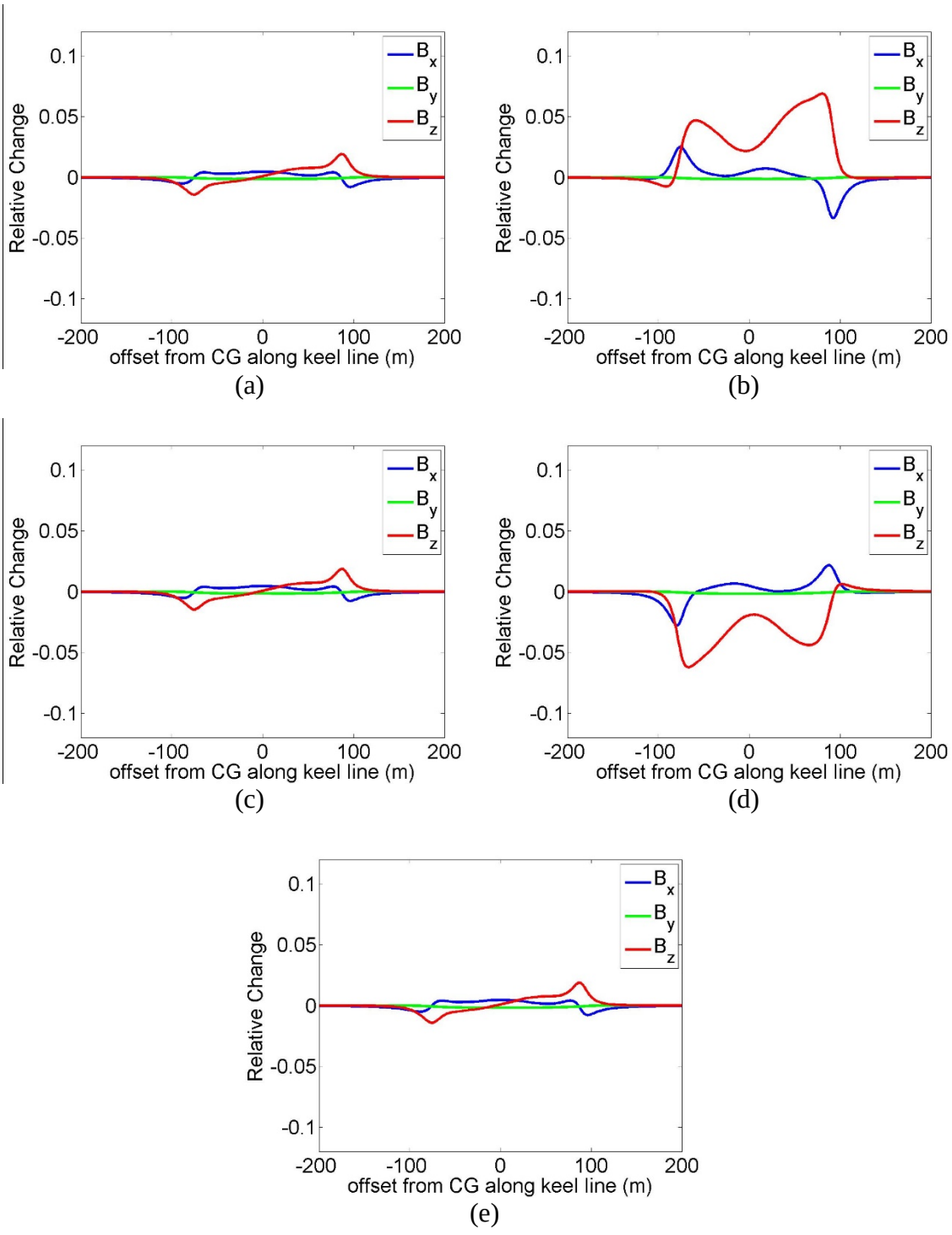

Figure 42. Relative change in the magnetic field along a line 9.5 m below the S-175 at y = 0 at (a) 21 s (b) 23.6 s (c) 26.2 s (d) 28.8 s (e) 31.4 s. The ship has a heading of 0 degrees and is excited by a 2 m wave with 10.5 s period.

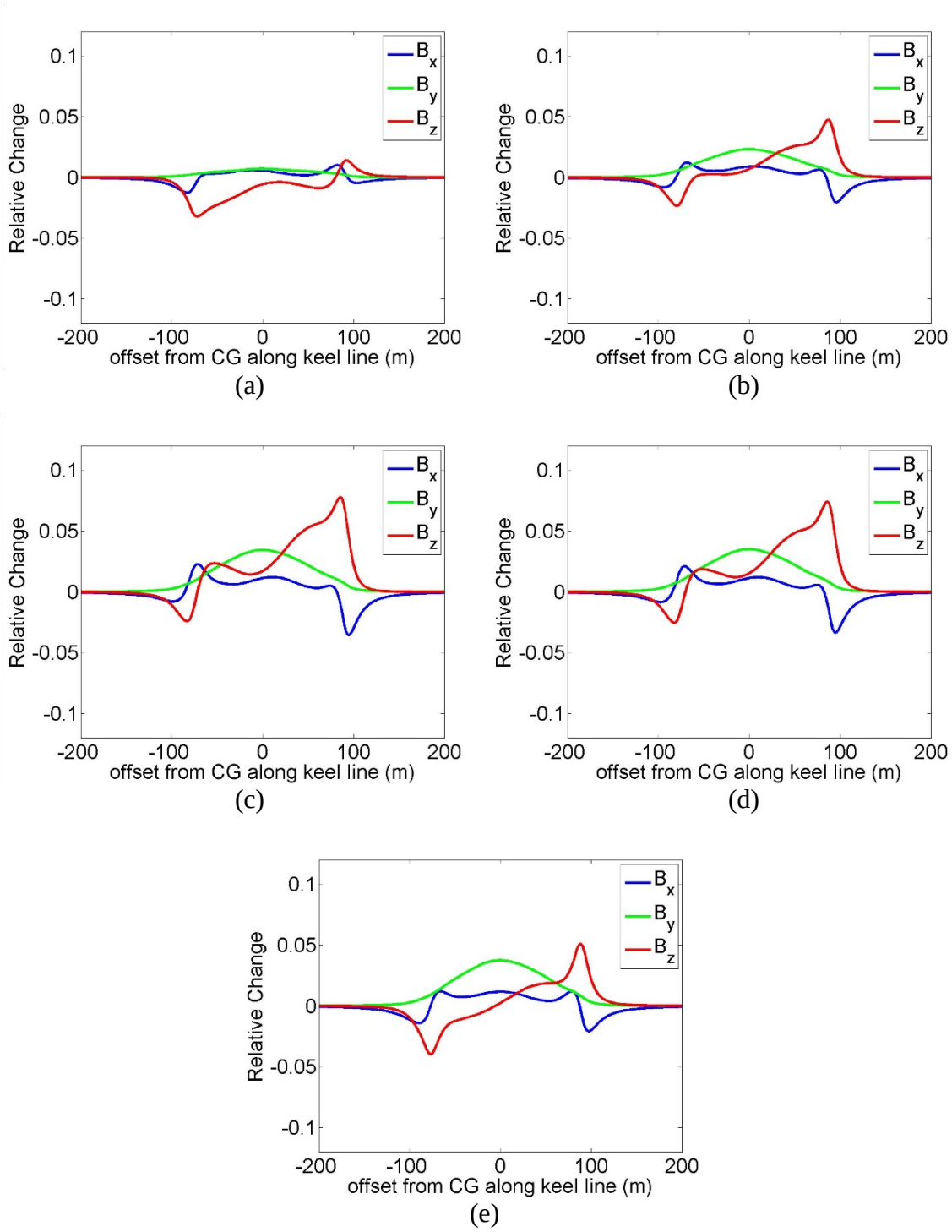

Figure 43. Relative change in the magnetic field along a line 9.5 m below the S-175 at y = 0 at (a) 21 s (b) 23.6 s (c) 26.2 s (d) 28.8 s (e) 31.4 s. The ship has a heading of 45 degrees and is excited by a 2 m wave with 10.5 s period.

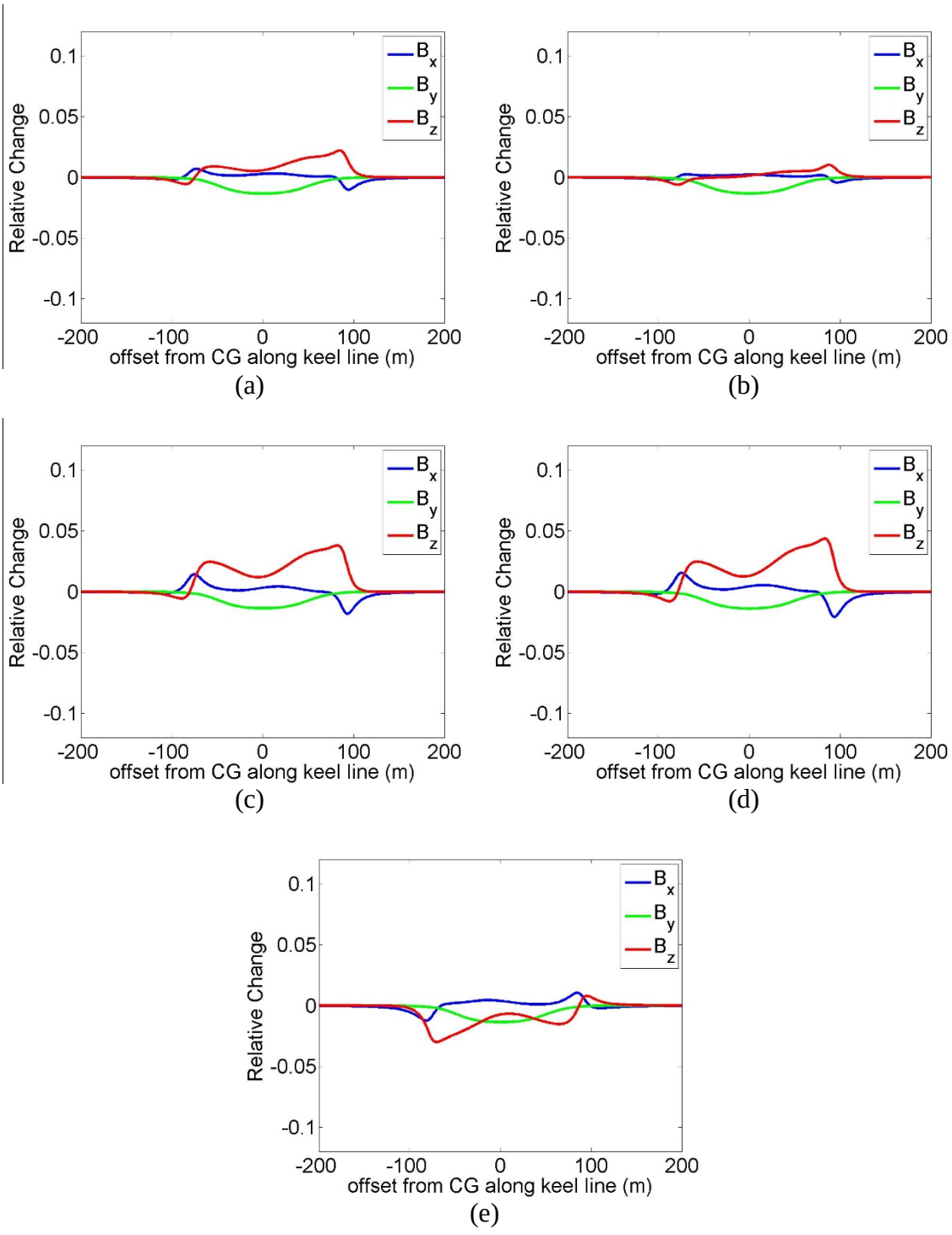

Figure 44. Relative change in the magnetic field along a line 9.5 m below the S-175 at y = 0 at (a) 21 s (b) 23.6 s (c) 26.2 s (d) 28.8 s (e) 31.4 s. The ship has a heading of 90 degrees and is excited by a 2 m wave with 10.5 s period.

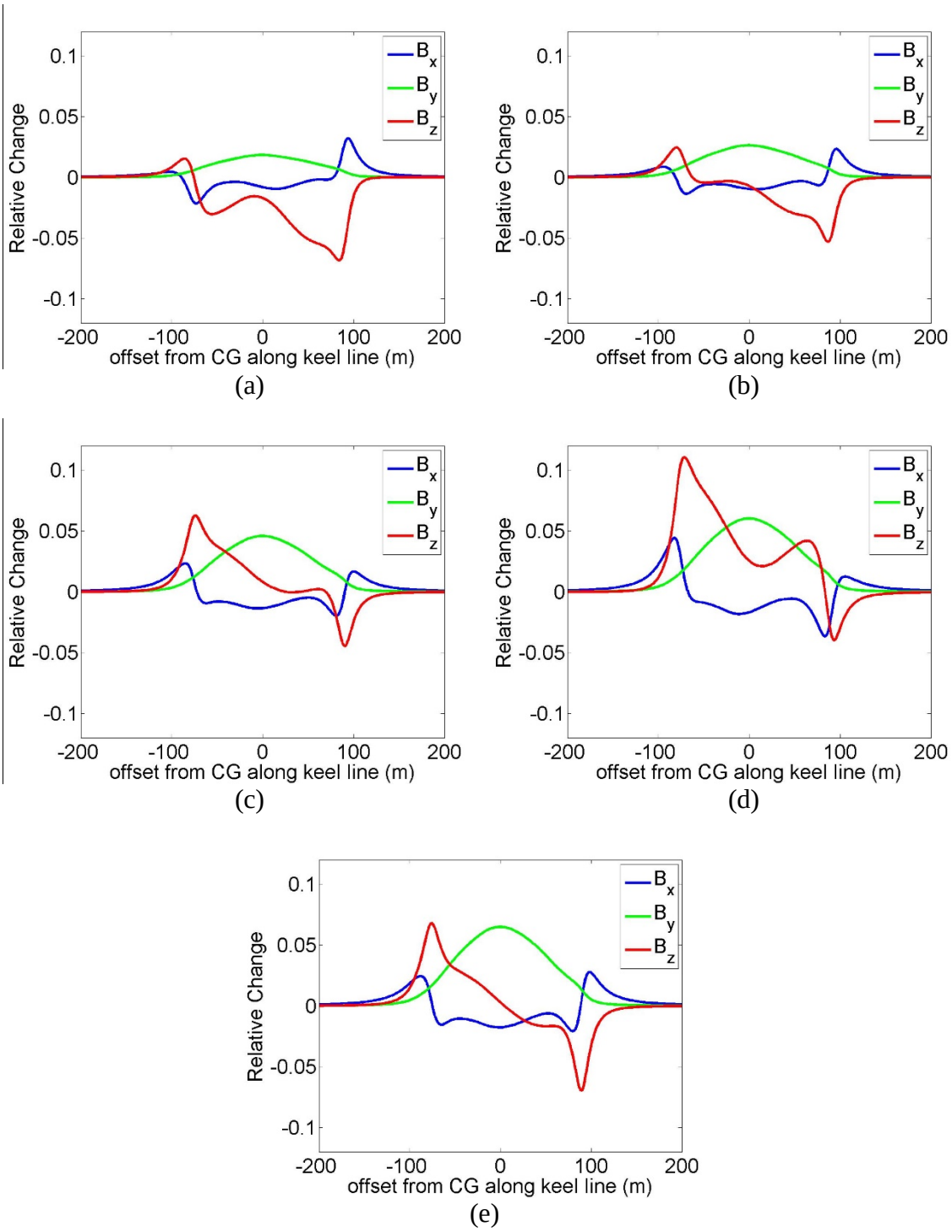

Figure 45. Relative change in the magnetic field along a line 9.5 m below the S-175 at y = 0 at (a) 21 s (b) 23.6 s (c) 26.2 s (d) 28.8 s (e) 31.4 s. The ship has a heading of 135 degrees and is excited by a 2 m wave with 10.5 s period.

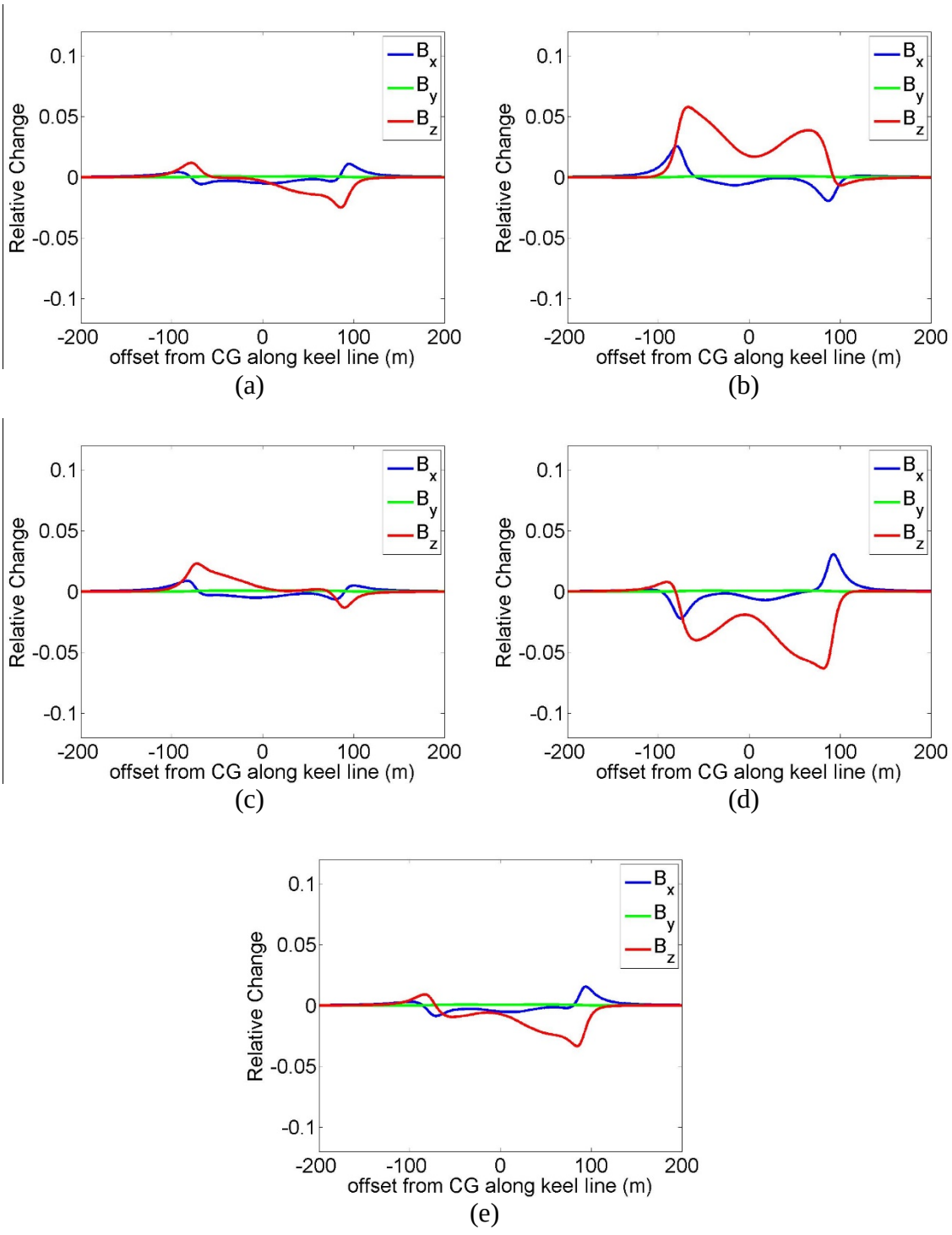

Figure 46. Relative change in the magnetic field along a line 9.5 m below the S-175 at y = 0 at (a) 21 s (b) 23.6 s (c) 26.2 s (d) 28.8 s (e) 31.4 s. The ship has a heading of 180 degrees and is excited by a 2 m wave with 10.5 s period.

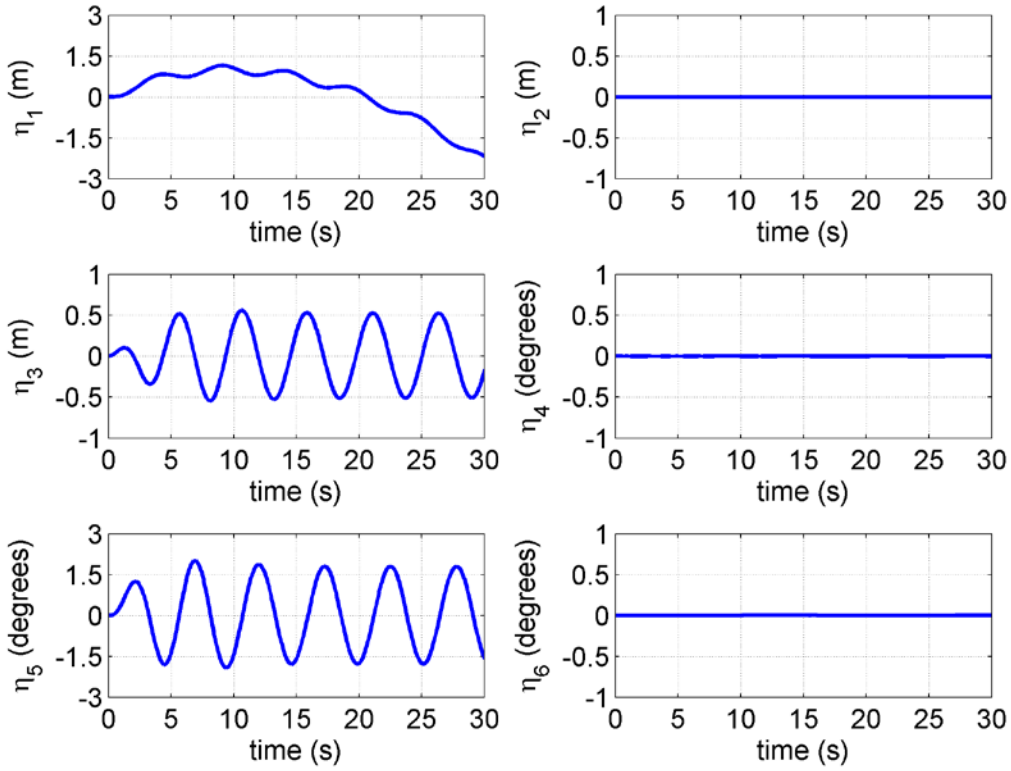

Figure 47. Time history of the box ship motion with 0 degree heading and forward speed of 10 knots. The ship is excited by a 10 cm amplitude wave with 7.5 s period.

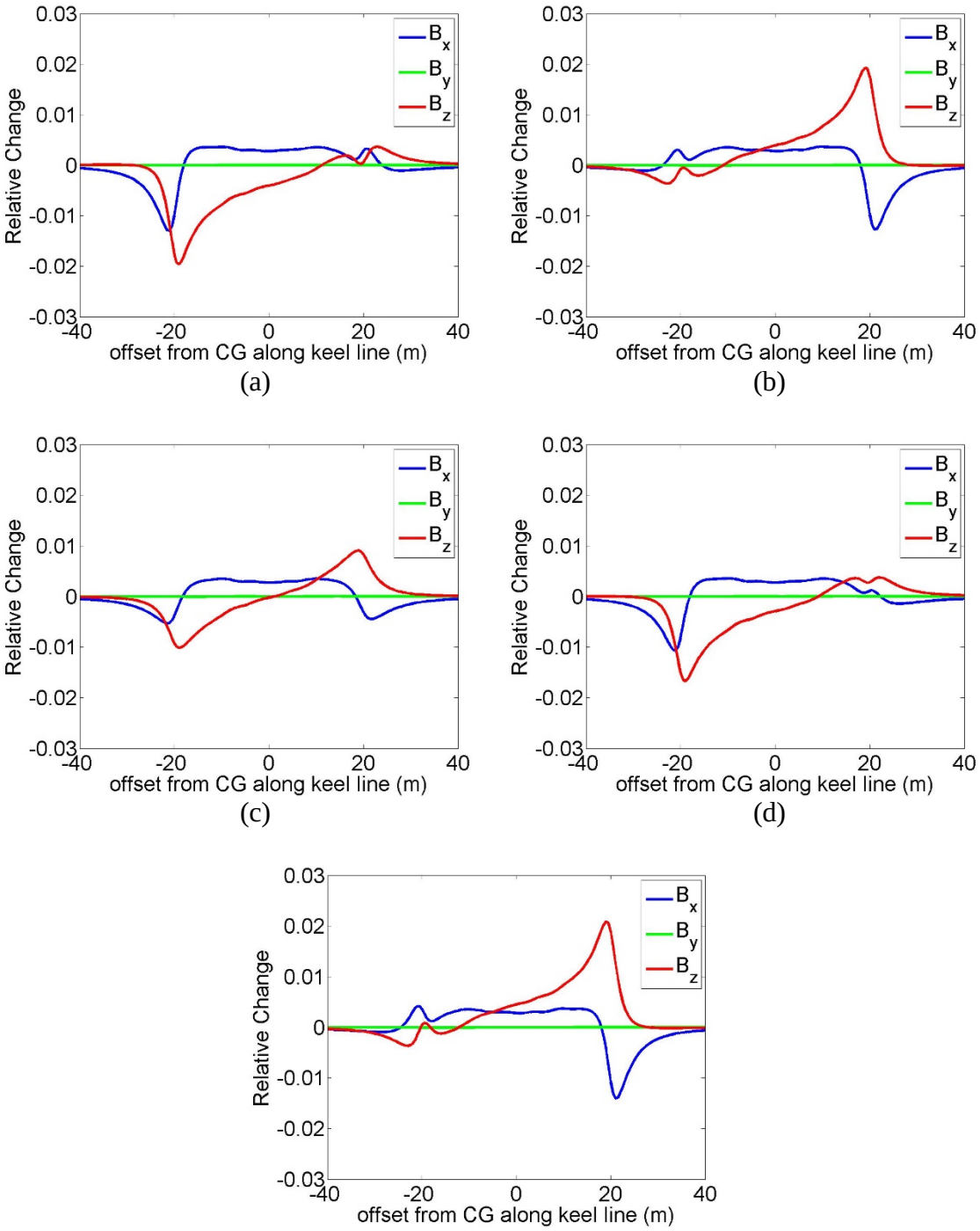

Figure 48. Relative change in the magnetic field along a line 2 m below the box ship at y = 0 at (a) 15 s (b) 16.8 s (c) 18.6 s (d) 20.6 s (e) 22.4 s. The ship has forward speed of 10 knots, a heading of 0 degrees, and is excited by a 10 cm wave with 7.5 s period.

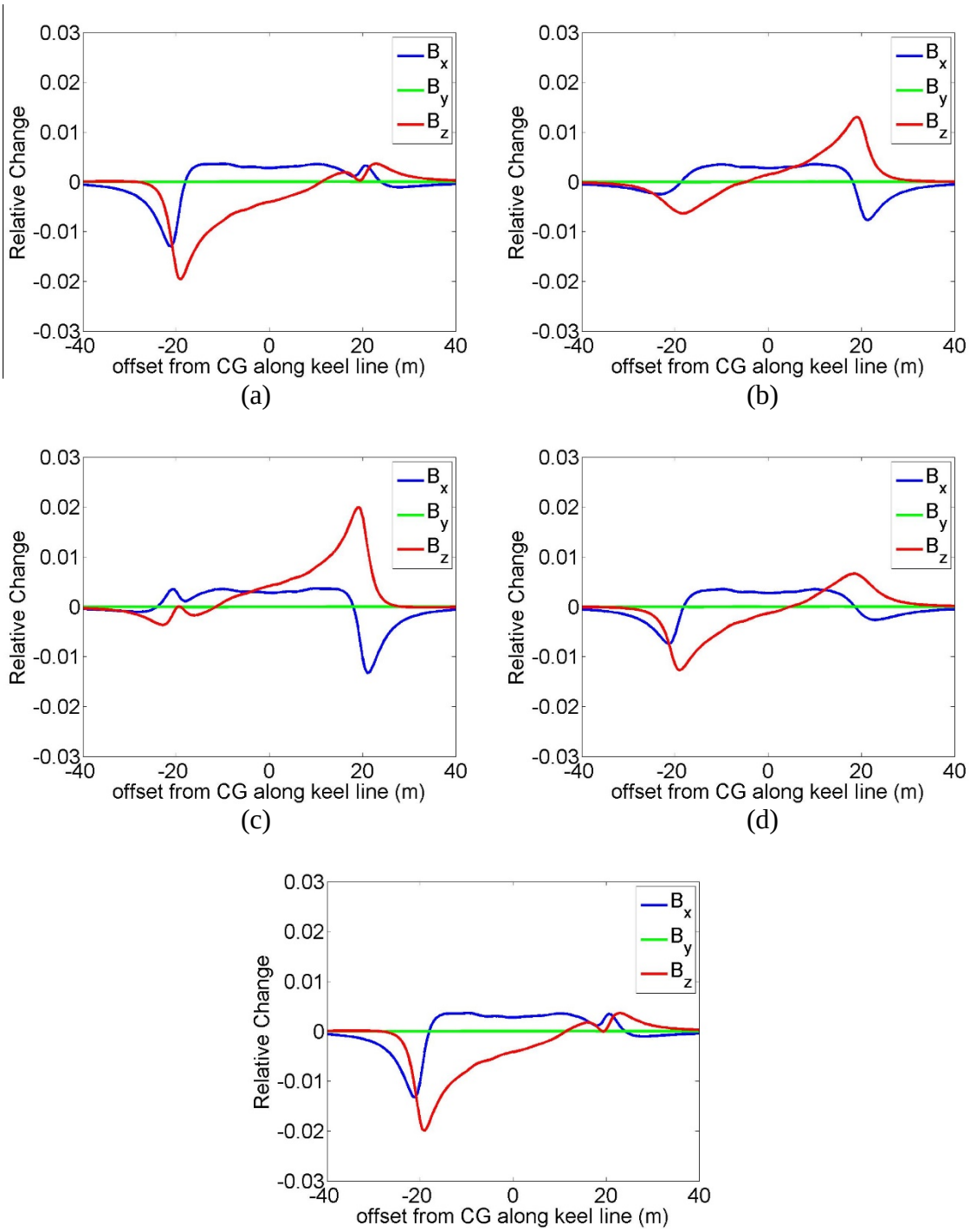

Figure 49. Relative change in the magnetic field along a line 2 m below the box ship at y = 0 at (a) 15 s (b) 16.2 s (c) 17.6 s (d) 18.8 s (e) 20.2 s. The ship has forward speed of 10 knots, a heading of 0 degrees, and is excited by a 10 cm wave with 7.5 s period.

4. CONCLUSIONS

In this thesis a quasi-strip theory method for simulating the nonlinear wave induced motion of a ship was developed and implemented. The impulse response method which was used allowed for the hydrodynamic coefficients to be computed by straightforward frequency-domain methods while the nonlinear equations of motion were solved in the time domain. A box shaped ship and the S-175 container ship were used to validate the code with other published results. The wave induced pressure on the face of each finite element is used by LS-DYNA to compute the stresses in the hull. Finally the motion and induced stresses are input to a magnetostatic volume integral equation code to compute the magnetic field. The changes in the magnetic field due to the wave induced motion and hull stresses is presented for the box ship and S-175 for multiple ship headings and wave amplitudes. At this time, no other results for the magnetic field of ship like structure under motion and stress are known to have been published for comparison.

The current method for simulating ship motion has several limitations. Strip theory requires a large length to breadth ratio which may limit the types of structures that may be analyzed. Only the restoring and Froude-Krylov forces are considered in computing the stresses in the hull as the strip method has not been derived for use with finite elements. Other more computationally complex techniques such as a panel method may also be implemented in the future which could allow all forces to be included in the stress analysis. Computation of rudder forces and a maneuvering model are not currently implemented which should improve the stability of the ship motion for oblique angles of incidence. Additionally, it should be fairly straightforward to expand the capabilities of the current

code to include multiple wave amplitudes and headings either by superposition, or by defining the wave in terms of a spectral density function as proposed in [17].

The results of this work have shown the ability of the magnetostatic volume integral equation to compute the magnetic field around a ferromagnetic material under motion and non-uniform stress, however, the magnetostrictive material model is still largely in development. The current model is only valid up to around 50% of saturation. More importantly, the results of this work have shown that the stress becomes periodic at steady state motion where effects such as creeping, which are currently not included, should provide an increased accuracy in results. Based on the results of the ship motion and wave induced pressure it may be possible to develop statistical models of the stresses in the hull of a ship which could simplify the simulation in the future.

APPENDIX A: VISCOUS DAMPING USING IKEDA'S METHOD

As previously stated, the viscous roll damping can be expressed by

$$B_{44} = B_F + B_W + B_E + B_{BK} + B_L \ , \tag{69}$$

where each term is computed using Ikeda's prediction method [30, 31]. The normalized roll damping coefficient is defined as

$$\hat{B}_{44} = \frac{B_{44}}{\rho \nabla B^2} \sqrt{\frac{B}{2g}} \ , \tag{70}$$

and the normalized circular wave frequency is defined as

$$\hat{\omega} = \omega \sqrt{\frac{B}{2g}} \ , \tag{71}$$

where ρ is the density of water, B is the ship breadth, ∇ is the volume of water displaced by the ship, and g is the acceleration due to gravity. Note that B_{44} as expressed in (36) and (69) is not normalized. Only the wave and eddy terms are computed as normalized quantities, therefore they must be un-normalized before used in the motion equations.

Frictional Component ($\mathbf{B_F}$)

The frictional damping component at zero speed is

$$B_{F0} = \frac{4}{3\pi} \rho s_f r_f^3 \varphi_a c_f \tag{72}$$

where s_f is the wetted surface area, r_f is the average radius from the axis of rolling, φ_a is the roll angle in radians, and c_f is the frictional coefficient. These parameters are given by

$$c_f = 1.328\sqrt{\frac{3.22 r_f^2 \varphi_a^2}{Tv}} \ , \tag{73}$$

$$r_f = \frac{\left(0.887 + 0.145 C_b\right)\left(1.7d + C_b B\right) - 2OG}{\pi} \ , \tag{74}$$

and

$$s_f = L_{pp}\left(1.75d + C_b B\right) \ , \tag{75}$$

where T is the roll period, v is the kinematic viscosity of water, C_b is the block coefficient of the ship, d is the ship draft, and OG is the distance from the calm water surface to the axis of rolling with positive direction being downward. The kinematic viscosity of sea water in $m^2 s$ is given by [11]

$$v = 10^{-6}\left(1.063 + 0.1039\left(\rho - 1000\right) + 0.02602\left(\rho - 1000\right)^2\right) \ . \tag{76}$$

It is important to note that this model for the frictional component only includes laminar flow, thus the computed magnitude will be negligible for a full-size ship. Adding a correction factor to (72) which includes the turbulent flow for a full-size ship results in

$$B_{F0} = 0.787 \rho s_f r_f^2 \sqrt{\omega v}\left\{1 + 0.00814\left(\frac{r_e^2 \varphi_a^2 \omega}{v}\right)^{0.386}\right\} \ . \tag{77}$$

For a ship moving with forward speed U

$$B_F = B_{F0}\left(1 + 4.1\frac{U}{\omega L_{pp}}\right) \ . \tag{78}$$

Lift Component (B_L)

In the case of non-zero forward speed, the lift component is

$$B_L = 0.075\rho U L_{pp} d^3 k_N \left[1 - 2.8\frac{OG}{d} + 4.667\left(\frac{OG}{d}\right)^2 \right], \tag{79}$$

where

$$k_N = 2\pi\frac{d}{L_{pp}} + \kappa\left(4.1\frac{B}{L_{pp}} - 0.045 \right). \tag{80}$$

Also

$$\begin{aligned} &\kappa = 0.0 \ \ for \ C_M \le 0.92 \\ &\kappa = 0.1 \ \ for \ 0.92 < C_M \le 0.97 \\ &\kappa = 0.3 \ \ for \ 0.97 < C_M \le 0.99 \end{aligned}, \tag{81}$$

where C_m is the midship coefficient.

Wave Component (B_W)

The wave component is given by

$$\hat{B}_w = \frac{A_1}{x_5}\exp\left(\frac{-A_2\left(\log\left(x_5\right) - A_3\right)^2}{1.44} \right), \tag{82}$$

where

$$
\begin{aligned}
x_1 &= \frac{B}{d} \\
x_2 &= C_b \\
x_3 &= C_m \\
x_4 &= 1 - \frac{OG}{d} \\
x_5 &= \hat{\omega}
\end{aligned}
\quad , \tag{83}
$$

and

$$
\begin{aligned}
A_1 &= \left(A_{11} x_2^2 + A_{12} x_2 + A_{13} \right) AA_1 \\
A_2 &= -1.402 x_2^3 + 7.189 x_2^2 - 10.993 x_2 + 9.45 \\
A_3 &= A_{31} x_2^6 + A_{32} x_2^5 + A_{33} x_2^3 + A_{35} x_2^2 + A_{36} x_2 + A_{37} + AA_3 \\
x_6 &= x_4 - AA_{32}
\end{aligned}
\quad . \tag{84}
$$

Detailed computation of the unknown coefficients in (84) can be found in [21].

Eddy Component ($\mathbf{B_E}$)

The eddy component is given by

$$
\hat{B}_{E0} = \frac{4\hat{\omega}\varphi_a}{3\pi x_2 x_1^3} C_R \ , \tag{85}
$$

where

$$
\begin{aligned}
C_R &= A_E \exp\left(B_{E1} + B_{E2} x_3^{B_{E3}}\right) \\
A_E &= \left(-0.0182 x_2 + 0.0155\right)\left(x_1 - 1.8\right)^3 - 79.414 x_2^4 + 215.695 x_2^3 \\
&\quad - 215.883 x_2^2 + 93.894 x_2 - 14.848 \\
B_{E1} &= \left(-0.2 x_1 + 1.6\right)\left(3.98 x_2 - 5.1525\right)\left(\begin{matrix}\left(0.9717 x_2^2 - 1.55 x_2 + 0.723\right) x_4 \\ + \left(0.04567 x_2 + 0.9408\right)\end{matrix}\right) x_4 \\
B_{E2} &= \left(0.25 x_4 + 0.95\right) x_4 - 219.2 x_2^3 + 443.7 x_2^2 - 283.3 x_2 + 59.6 \\
B_{E3} &= \left(46.5 - 15 x_1\right) x_2 + 11.2 x_1 - 28.6
\end{aligned}
\quad . \tag{86}
$$

and the coefficients x_1, x_2, and x_3 are given by (83) and

$$
x_4 = \frac{OG}{d} \ . \tag{87}
$$

If the ship has forward speed U, the eddy component decreases according to

$$
\hat{B}_{\mathrm{E}} = \hat{B}_{E0}\left[\frac{(0.04\omega L_{pp}/U)^2}{1+(0.04\omega L_{pp}/U)^2}\right] . \tag{88}
$$

APPENDIX B: CONFORMAL MAPPING

Ursell derived an analytic solution for the potential coefficients of a circular cylinder [12]. The work of several others including Tasai [13] extended this solution by conformally mapping arbitrary ship sections to a unit semi-circle. The general transformation is given by

$$x + iy = M_s \sum \left\{ a_{2n-1} \zeta^{-(2n-1)} \right\} \ , \tag{89}$$

where the left hand side of the equation is a point in the plane of the arbitrary ship section, $\zeta = ie^{\alpha} e^{-i\theta}$ is the plane of the unit circle, M_s is the scale factor, and a_{2n-1} is a set of conformal mapping coefficients $(n = 1, ..., N)$ where N is the number of mapping parameters, and $a_{-1} = 1$.

The unit circle is obtained by setting $\alpha = 0$, thus the relationship between the two coordinate systems becomes

$$\begin{aligned} x_0 &= -M_s \sum_{n=0}^{N} \left\{ (-1)^n a_{2n-1} \sin\left((2n-1)\theta \right) \right\} \\ y_0 &= +M_s \sum_{n=0}^{N} \left\{ (-1)^n a_{2n-1} \cos\left((2n-1)\theta \right) \right\} \end{aligned} \tag{90}$$

where

$$M_s = \frac{B_s / 2}{\sum_{n=0}^{N} a_{2n-1}} \tag{91}$$

and B_s is the sectional breadth. It is important to note that the z-axis in Tasai's coordinate system is positive facing downward. Using $N = 2$ mapping coefficients will result in the

so called Lewis transformation, while setting $N = 10$ will result in the Close-Fit conformal mapping. This work computes potential coefficients using Close-Fit conformal mapping beginning with Lewis coefficients as a first guess. The other mapping coefficients are computed iteratively until a specified error tolerance is achieved.

From (90), the Lewis transformation is

$$\begin{aligned} x_0 &= M_s\left(\left(1+a_1\right)\sin\theta - a_3\sin 3\theta\right) \\ y_0 &= M_s\left(\left(1-a_1\right)\cos\theta + a_3\cos 3\theta\right) \end{aligned}, \tag{92}$$

and the scale factor becomes

$$M_s = \frac{B/2}{1+a_1+a_3} = \frac{D_s}{1-a_1+a_3} \tag{93}$$

where D_s is the sectional draft. The sectional half breadth to draft ratio is

$$H_0 = \frac{B_s/2}{D_s} = \frac{1+a_1+a_3}{1-a_1+a_3}\ , \tag{94}$$

and the sectional area coefficient is

$$\sigma_s = \frac{A_s}{B_s D_s} = \frac{\pi}{4}\frac{1-a_1^2-3a_3^2}{\left(1+a_3\right)^2-a_1^2} \tag{95}$$

where A_s is the area of the cross section. Solving (94) for a_1 and substituting into (95) results in the quadratic equation

$$c_1 a_3^2 + c_2 a_3 + c_3 = 0 \tag{96}$$

with

$$
\begin{aligned}
c_1 &= 3+\frac{4\sigma_s}{\pi}+\left(1-\frac{4\sigma_s}{\pi}\right)\left(\frac{H_0-1}{H_0+1}\right)^2 \\
c_2 &= 2c_1-6 \\
c_3 &= c_1-4
\end{aligned}
\quad . \tag{97}
$$

The valid solutions for a_3 and a_1 in (96) are

$$
\begin{aligned}
a_3 &= \frac{-c_1+3+\sqrt{9-2c_1}}{c_1} \\
a_1 &= \frac{H_0-1}{H_0+1}(a_3+1)
\end{aligned}
\quad . \tag{98}
$$

All other mapping coefficients a_{2n-1} $(N=3,...,10)$ are initially set to zero. With the initial M_s and a_{2n-1} values, the iterative procedure begins by determining the angle θ_i such that each point of the approximated section (x_{0i}, y_{0i}) lies on the normal to the actual contour (x_i, y_i) which results in [32]

$$
\begin{aligned}
&x_i\cos\phi_i + M_s\cos\phi_i\sum_{n=0}^{N}(-1)^n a_{2n-1}\sin((2n-1)\theta) \\
&-x_y\sin\phi_i + M_s\sin\phi_i\sum_{n=0}^{N}(-1)^n a_{2n-1}\sin((2n-1)\theta) = 0
\end{aligned}
\tag{99}
$$

where

$$
\begin{aligned}
\cos\phi_i &= \frac{x_{i+1}-x_{i-1}}{\sqrt{(x_{i+1}-x_{i-1})^2+(y_{i+1}-y_{i-1})^2}} \\
\sin\phi_i &= \frac{-y_{i+1}+y_{i-1}}{\sqrt{(x_{i+1}-x_{i-1})^2+(y_{i+1}-y_{i-1})^2}}
\end{aligned}
\quad . \tag{100}
$$

This work uses Brent's method [33] to find the value of θ_i in (99), but any other root finding algorithm may be used. Once the value of θ_i is determined, the square of the deviation from the point on the real contour is given by

$$e_i = (x_i - x_{0i})^2 + (y_i - y_{0i})^2 \ . \tag{101}$$

After determining θ_i for all $I+1$ points, the sum of squares of deviation is

$$E = \sum_{i=0}^{I} e_i \ . \tag{102}$$

Substituting (90) and (101) into (102) results in

$$E = \sum_{i=0}^{I} \left\{ \begin{array}{l} +\left(x_i + \sum_{n=0}^{N} (-1)^n M_s a_{2n-1} \sin((2n-1)\theta_i) \right)^2 \\ +\left(y_i + \sum_{n=0}^{N} (-1)^n M_s a_{2n-1} \cos((2n-1)\theta_i) \right)^2 \end{array} \right\} \tag{103}$$

for which new values of $[M_s a_{2n-1}]$ must be determined to minimize E. This implies

$$\frac{\partial E}{\partial [M_s a_{2j-1}]} = 0 \quad j = 0,...N \tag{104}$$

which results in $N+1$ equations

$$\begin{aligned} \sum_{i=0}^{I} \left\{ \begin{array}{l} -\sin((2j-1)\theta_i) \sum_{n=0}^{N} (-1)^n M_s a_{2n-1} \sin((2n-1)\theta_i) \\ -\cos((2j-1)\theta_i) \sum_{n=0}^{N} (-1)^n M_s a_{2n-1} \cos((2n-1)\theta_i) \end{array} \right\} & \quad j = 0,...N \\ = \sum_{i=0}^{I} \left\{ x_i \sin((2j-1)\theta_i) - y_i \cos((2j-1)\theta_i) \right\} & \ . \end{aligned} \tag{105}$$

Equation (105) is rewritten as

$$\begin{aligned} &\sum_{n=0}^{N}\left\{(-1)^n M_s a_{2n-1}\sum_{i=0}^{I}\cos((2j-2n)\theta_i)\right\} = \\ &\sum_{i=0}^{I}\left\{-x_i\sin((2j-1)\theta_i)+y_i\cos((2j-1)\theta_i)\right\} \qquad j=0,\ldots N \end{aligned} \quad . \tag{106}$$

To achieve the exact breadth and draft of the original contour, the last two equations are replaced such that (106) becomes

$$\begin{aligned} &\sum_{n=0}^{N}\left\{(-1)^n M_s a_{2n-1}\sum_{i=0}^{I}\cos((2j-2n)\theta_i)\right\} = \\ &\sum_{i=0}^{I}\left\{-x_i\sin((2j-1)\theta_i)+y_i\cos((2j-1)\theta_i)\right\} \qquad j=0,\ldots N-2 \\ &\sum_{n=0}^{N} M_s a_{2n-1} = B_s/2 \qquad j=N-1 \\ &\sum_{n=0}^{N}(-1)^n M_s a_{2n-1} = D_s \qquad j=N \end{aligned} \quad . \tag{107}$$

The system of equations in (107) is solved numerically to obtain new values of $M_s a_{2n-1}$ which are then be used to compute new values of θ_i. This iterative procedure is repeated until a specified error tolerance is achieved. It is suggested [8] that the difference in error calculated by (103) between subsequent iterations be less than

$$\Delta E = (I+1)\left(0.00005\sqrt{b_{\max}{}^2 + d_{\max}{}^2}\right)^2 , \tag{108}$$

where $b_{\max}$ is the maximum half breadth of the cross section and $d_{\max}$ is the maximum draft of the cross section.

APPENDIX C COMPUTING HYDRODYNAMIC COEFFICIENTS

The 2D potential coefficients are computed in heave, sway, and roll using close-fit conformal mapping and the potential theory of Tasai. For each motion mode it is assumed that an infinitely long circular cylinder is forced to oscillate with frequency ω. This forced harmonic motion will produce a system of standing waves which will be denoted by the subscript A, and a set of travelling waves which will be denoted by the subscript B. The process of determining the hydrodynamic coefficients involves deriving a set of velocity potential and stream functions that satisfies Laplace's equation and the boundary condition on the surface of the cylinder. This section very briefly describes the computation of the added mass and damping coefficients. A detailed derivation of these coefficients can be found in [8].

Heave Coefficients

To calculate the heave coefficients a_{33} and b_{33} in (19) and (20), it is necessary to determine the values of A_0, B_0, M_0, and N_0. It can be shown that the stream function which satisfies the boundary condition on the surface of the cylinder is

$$\Psi_0(\theta) = -\dot{y}\frac{b_0}{2}h(\theta) + C(t) \ . \tag{109}$$

Here, $b_0 = M_s \sum_{n=0}^{N} a_{2n-1}$ is the sectional breadth, $C(t) = 0$ due to the symmetry of the fluid about the y axis, and

$$h(\theta)=\frac{2x_0}{b_0}=-\frac{1}{\sigma_a}\sum_{n=0}^{N}\left\{(-1)^n a_{2n-1}\sin((2n-1)\theta)\right\} \tag{110}$$

where $\sigma_a=\sum_{n=0}^{N} a_{2n-1}$ is the sectional area coefficient.

The set of velocity potential functions for the standing wave that satisfies Laplace's equation, the symmetric motion of the fluid, and the free surface condition is given by

$$\Phi_A=\frac{g\eta_a}{\pi\omega}\left(\sum_{m=1}^{\infty}\{P_{2m}\phi_{A2m}(\alpha,\theta)\cos(\omega t)\}+\sum_{m=1}^{\infty}\{Q_{2m}\phi_{A2m}(\alpha,\theta)\sin(\omega t)\}\right) \tag{111}$$

where

$$\begin{aligned}\phi_{A2m}(\alpha,\theta)&=e^{-2m\alpha}\cos(2m\theta)\\&\quad-\frac{\xi_b}{\sigma_a}\sum_{n=0}^{N}\left\{(-1)^n\frac{2n-1}{2m+2n-1}a_{2n-1}e^{-(2m+2n-1)\alpha}\cos((2m+2n-1)\theta)\right\}\end{aligned} \tag{112}$$

in which $\xi_b=\frac{\omega^2 b_0}{2g}$ is the non-dimensional square frequency.

The set of conjugate stream functions for the standing wave is given by

$$\Psi_A=\frac{g\eta_a}{\pi\omega}\left(\sum_{m=1}^{\infty}\{P_{2m}\psi_{A2m}(\alpha,\theta)\cos(\omega t)\}+\sum_{m=1}^{\infty}\{Q_{2m}\psi_{A2m}(\alpha,\theta)\sin(\omega t)\}\right) \tag{113}$$

where

$$\begin{aligned}\psi_{A2m}(\alpha,\theta)&=e^{-2m\alpha}\sin(2m\theta)\\&\quad-\frac{\xi_b}{\sigma_a}\sum_{n=0}^{N}\left\{(-1)^n\frac{2n-1}{2m+2n-1}a_{2n-1}e^{-(2m+2n-1)\alpha}\sin((2m+2n-1)\theta)\right\}\end{aligned}. \tag{114}$$

The velocity potential for the travelling wave is given by

$$\Phi_B = \frac{g\eta_a}{\pi\omega}\left\{\phi_{Bc}(x,y)\cos(\omega t) + \phi_{Bs}(x,y)\sin(\omega t)\right\} \tag{115}$$

where

$$\phi_{Bc} = +\pi e^{-\nu y}\cos(\nu x)\ , \tag{116}$$

and

$$\phi_{Bs} = +\pi e^{-\nu y}\sin(\nu|x|) + \int_o^\infty \frac{\nu\sin(ky) - k\cos(ky)}{k^2+\nu^2} e^{-k|x|}dk\ . \tag{117}$$

in which $\nu = \frac{\omega^2}{g}$ is the wave number in deep water. The conjugate stream function is given by

$$\Psi_B = \frac{g\eta_a}{\pi\omega}\left\{\psi_{Bc}(x,y)\cos(\omega t) + \psi_{Bs}(x,y)\sin(\omega t)\right\} \tag{118}$$

where

$$\psi_{Bc} = +\pi e^{-\nu y}\sin(\nu|x|)\ , \tag{119}$$

and

$$\psi_{Bs} = -\pi e^{-\nu y}\cos(\nu x) + \int_o^\infty \frac{\nu\cos(ky) + k\sin(ky)}{k^2+\nu^2} e^{-k|x|}dk\ . \tag{120}$$

Convergence rate of the integrals in (117) and (120) are very slow, so they are replaced by a power series expansion [34] such that

$$\begin{aligned}\int_0^\infty \frac{\nu\cos(ky)+k\sin(ky)}{k^2+\nu^2}e^{-kx}dk &= \{Q\sin(\nu x)-(S-\pi)\cos(\nu x)\}e^{-\nu y}\\ \int_0^\infty \frac{\nu\sin(ky)-k\cos(ky)}{k^2+\nu^2}e^{-kx}dk &= \{Q\cos(\nu x)+(S-\pi)\sin(\nu x)\}e^{-\nu y}\end{aligned}, \quad (121)$$

where

$$\begin{aligned}Q &= \gamma+\ln\left(\nu\sqrt{x^2+y^2}\right)+\sum_{n=1}^{\infty}p_n\cos(n\beta)\\ S &= \beta+\sum_{n=1}^{\infty}p_n\sin(n\beta)\\ \beta &= \arctan\left(\frac{x}{y}\right)\\ p_n &= \frac{\left(\nu\sqrt{x^2+y^2}\right)^n}{n\cdot n!}\end{aligned}. \quad (122)$$

Here, γ is Euler's constant. While these power series expansions converge much faster than the numeric integration, the summation over n must be truncated at a certain value. It is suggested in [8] to use the number of mapping coefficients such that $n=1,...,N$.

The total velocity potential and stream function are now

$$\begin{aligned}\Phi &= \Phi_A+\Phi_B\\ \Psi &= \Psi_A+\Psi_B\end{aligned} \quad (123)$$

which after a change of parameters in (115) and (118) becomes

$$\Phi(\alpha,\theta)=\frac{g\eta_a}{\pi\omega}\begin{pmatrix}+\left(\phi_{Bc}(\alpha,\theta)+\sum_{m=1}^{\infty}\{P_{2m}\phi_{A2m}(\alpha,\theta)\}\right)\cos(\omega t)\\+\left(\phi_{Bs}(\alpha,\theta)+\sum_{m=1}^{\infty}\{Q_{2m}\phi_{A2m}(\alpha,\theta)\}\right)\sin(\omega t)\end{pmatrix}$$

$$\Psi(\alpha,\theta)=\frac{g\eta_a}{\pi\omega}\begin{pmatrix}+\left(\psi_{Bc}(\alpha,\theta)+\sum_{m=1}^{\infty}\{P_{2m}\psi_{A2m}(\alpha,\theta)\}\right)\cos(\omega t)\\+\left(\psi_{Bs}(\alpha,\theta)+\sum_{m=1}^{\infty}\{Q_{2m}\psi_{A2m}(\alpha,\theta)\}\right)\sin(\omega t)\end{pmatrix}. \quad (124)$$

By setting $\alpha=0$ in (124), which corresponds to the surface of the cylinder, the stream function is now equal to (109) such that

$$\Psi_0(\theta)=\frac{g\eta_a}{\pi\omega}\begin{pmatrix}+\left(\psi_{Bc}(\theta)+\sum_{m=1}^{\infty}\{P_{2m}\psi_{A02m}(\theta)\}\right)\cos(\omega t)\\+\left(\psi_{Bs}(\theta)+\sum_{m=1}^{\infty}\{Q_{2m}\psi_{A02m}(\theta)\}\right)\sin(\omega t)\end{pmatrix}=-\dot{y}\frac{b_0}{2}h(\theta), \quad (125)$$

where

$$\psi_{A02m}(\theta)=\sin(2m\theta)-\frac{\xi_b}{\sigma_a}\sum_{n=0}^{N}\left\{(-1)^n\frac{2n-1}{2m+2n-1}a_{2n-1}\sin((2m+2n-1)\theta)\right\}. \quad (126)$$

Therefore,

$$\begin{pmatrix}+\left(\psi_{Bc}(\theta)+\sum_{m=1}^{\infty}\{P_{2m}\psi_{A02m}(\theta)\}\right)\cos(\omega t)\\+\left(\psi_{Bs}(\theta)+\sum_{m=1}^{\infty}\{Q_{2m}\psi_{A02m}(\theta)\}\right)\sin(\omega t)\end{pmatrix}=-\dot{y}\frac{\pi\omega b_0}{2g\eta_a}h(\theta). \quad (127)$$

The right hand side of (127) can be rewritten as

$$-\dot{y}\frac{\pi\omega b_0}{2g\eta_a}h(\theta) = h(\theta)\left\{\frac{y_a}{\eta_a}\pi\xi_b\sin(\omega t+\delta)\right\} \\ = h(\theta)\{A_0\cos(\omega t)+B_0\sin(\omega t)\} \tag{128}$$

where

$$A_0 = \frac{y_a}{\eta_a}\pi\xi_b\sin\delta \\ B_0 = \frac{y_a}{\eta_a}\pi\xi_b\cos\delta \tag{129}$$

This results in the two sets of equations

$$\psi_{B0c}(\theta)+\sum_{m=1}^{\infty}P_{2m}\psi_{A02m}(\theta) = h(\theta)A_0 \\ \psi_{B0s}(\theta)+\sum_{m=1}^{\infty}Q_{2m}\psi_{A02m}(\theta) = h(\theta)B_0 \tag{130}$$

By setting $\theta=\pi/2$ the coefficients A_0 and B_0 are obtained as

$$A_0 = \phi_{B0c}(\pi/2)+\sum_{m=1}^{\infty}P_{2m}\psi_{A02m}(\pi/2) \\ B_0 = \phi_{B0s}(\pi/2)+\sum_{m=1}^{\infty}Q_{2m}\psi_{A02m}(\pi/2) \tag{131}$$

Substituting (131) into (130) yields two equations for each angle θ that can be solved for the unknown parameters P_{2m} and Q_{2m}

$$\psi_{B0c}(\theta)-h(\theta)\psi_{B0c}(\pi/2) = \sum_{m=1}^{\infty}f_{2m}(\theta)P_{2m} \\ \psi_{B0s}(\theta)-h(\theta)\psi_{B0s}(\pi/2) = \sum_{m=1}^{\infty}f_{2m}(\theta)Q_{2m} \tag{132}$$

where

$$f_{2m}(\theta) = -\psi_{A02m}(\theta) + h(\theta)\psi_{A02m}(\pi/2) \ . \tag{133}$$

By multiplying both sides by $\Delta\theta$ the summation over θ can be replaced by integration such that

$$\sum_{m=1}^{M}\left\{P_{2m}\int_0^{\pi/2} f_{2m}(\theta)\, f_{2n}(\theta)d\theta\right\} = \int_0^{\pi/2}\left(\psi_{B0c}(\theta) - h(\theta)\psi_{B0c}(\pi/2)\right) f_{2n}(\theta)d\theta$$

$$\sum_{m=1}^{M}\left\{Q_{2m}\int_0^{\pi/2} f_{2m}(\theta)\, f_{2n}(\theta)d\theta\right\} = \int_0^{\pi/2}\left(\psi_{B0s}(\theta) - h(\theta)\psi_{B0s}(\pi/2)\right) f_{2n}(\theta)d\theta \ . \tag{134}$$

$$n = 1, ..., M$$

To solve for P_{2m} and Q_{2m} in (134) it is required that $M \geq N$ where $N = 10$ for a close-fit mapped section. Using the solutions for P_{2m} and Q_{2m}, the coefficients A_0 and B_0 can now be obtained by (131), and the velocity potential on the surface of the cylinder becomes

$$\Phi_0(\theta) = \frac{g\eta_a}{\pi\omega}\begin{Bmatrix} +\left(\phi_{B0c}(\theta) + \sum_{m=1}^{\infty} P_{2m}\phi_{A02m}(\theta)\right)\cos(\omega t) \\ +\left(\phi_{B0s}(\theta) + \sum_{m=1}^{\infty} Q_{2m}\phi_{A02m}(\theta)\right)\sin(\omega t) \end{Bmatrix} . \tag{135}$$

The hydrodynamic pressure on the surface of the cylinder is obtained by the linearized Bernoulli equation as

$$p(\theta) = -\rho\frac{\partial\Phi_0(\theta)}{\partial t}$$

$$= \frac{-\rho g\eta_a}{\pi}\begin{Bmatrix} -\left(\phi_{B0c}(\theta) + \sum_{m=1}^{\infty} P_{2m}\phi_{A02m}(\theta)\right)\sin(\omega t) \\ +\left(\phi_{B0s}(\theta) + \sum_{m=1}^{\infty} Q_{2m}\phi_{A02m}(\theta)\right)\cos(\omega t) \end{Bmatrix}, \tag{136}$$

and the two dimensional vertical heave force acting on the cylinder is

$$F_y = \int_{-\pi/2}^{\pi/2} p(\theta)\frac{dx_0}{ds}ds = -2\int_0^{\pi/2} p(\theta)\frac{dx_0}{d\theta}d\theta \quad . \tag{137}$$

Equation (137) can be rewritten as

$$F_y = \frac{\rho g b_0 \eta_a}{\pi}(M_0\cos(\omega t) - N_0\sin(\omega t)) \tag{138}$$

where

$$\begin{aligned} M_0 = &-\frac{1}{\sigma_a}\int_0^{\pi/2}\phi_{B0s}(\theta)\sum_{n=0}^{N}\left\{(-1)^n(2n-1)a_{2n-1}\cos((2n-1)\theta)\right\} \\ &-\frac{1}{\sigma_a}\sum_{m=1}^{M}\left\{(-1)^m Q_{2m}\sum_{n=0}^{N}\left\{\frac{(2n-1)^2}{(2m)^2-(2n-1)^2}a_{2n-1}\right\}\right\} \\ &+\frac{\pi\eta_b}{4\sigma_a^2}\left(Q_2+\sum_{m=1}^{N}\left\{(-1)^m Q_{2m}\sum_{n=0}^{N-m}\left\{(2n-1)a_{2n-1}a_{2m+2n-1}\right\}\right\}\right) \end{aligned} \tag{139}$$

and

$$\begin{aligned} N_0 = &-\frac{1}{\sigma_a}\int_0^{\pi/2}\phi_{B0c}(\theta)\sum_{n=0}^{N}\left\{(-1)^n(2n-1)a_{2n-1}\cos((2n-1)\theta)\right\} \\ &-\frac{1}{\sigma_a}\sum_{m=1}^{M}\left\{(-1)^m P_{2m}\sum_{n=0}^{N}\left\{\frac{(2n-1)^2}{(2m)^2-(2n-1)^2}a_{2n-1}\right\}\right\} \\ &+\frac{\pi\eta_b}{4\sigma_a^2}\left(P_2+\sum_{m=1}^{N}\left\{(-1)^m P_{2m}\sum_{n=0}^{N-m}\left\{(2n-1)a_{2n-1}a_{2m+2n-1}\right\}\right\}\right) \end{aligned} \quad . \tag{140}$$

Sway Coefficients

To calculate the sway coefficients a_{22} and b_{22} in (19) and (20), it is necessary to determine the values of M_0, N_0, P_0 and Q_0. Following the same procedure used in the heave coefficients to define a set of velocity potential and stream functions results in

$$\phi_{A02m}(\theta) = \sin((2m+1)\theta) - \frac{\xi_b}{\sigma_a}\sum_{n=0}^{N}\left\{(-1)^n \frac{2n-1}{2m+2n} a_{2n-1}\sin((2m+2n)\theta)\right\}, \quad (141)$$

$$\psi_{A02m}(\theta) = -\cos((2m+1)\theta) + \frac{\xi_b}{\sigma_a}\sum_{n=0}^{N}\left\{(-1)^n \frac{2n-1}{2m+2n} a_{2n-1}\cos((2m+2n)\theta)\right\}, \quad (142)$$

$$\psi_{Bc} = +\pi e^{-\nu y}\cos(\nu x), \quad (143)$$

$$\psi_{Bs} = +\pi e^{-\nu y}\sin(\nu|x|) + \int_o^\infty \frac{\nu\sin(ky) - k\cos(ky)}{k^2+\nu^2} e^{-k|x|}dk - \frac{y}{\nu(x^2+y^2)}, \quad (144)$$

$$j\phi_{Bc} = -\pi e^{-\nu y}\sin(\nu|x|), \quad (145)$$

$$j\phi_{Bs} = +\pi e^{-\nu y}\cos(\nu x) - \int_o^\infty \frac{\nu\cos(ky) + k\sin(ky)}{k^2+\nu^2} e^{-k|x|}dk + \frac{|x|}{\nu(x^2+y^2)}. \quad (146)$$

Here, $\nu = \frac{\omega^2}{g}$ is the wave number in deep water and

$$\begin{aligned} j &= +1 \quad for:\ x \geq 0 \\ j &= -1 \quad for:\ x < 0 \end{aligned}. \quad (147)$$

The terms P_{2m} and Q_{2m} are determined according to

$$\sum_{m=0}^{M}\left\{P_{2m}\int_0^{\pi/2} f_{2m}(\theta)\,f_{2n}(\theta)d\theta\right\}=\int_0^{\pi/2}\left(\psi_{B0c}(\theta)-\psi_{B0c}(\pi/2)\right)f_{2n}(\theta)d\theta$$

$$\sum_{m=0}^{M}\left\{Q_{2m}\int_0^{\pi/2} f_{2m}(\theta)\,f_{2n}(\theta)d\theta\right\}=\int_0^{\pi/2}\left(\psi_{B0s}(\theta)-\psi_{B0s}(\pi/2)\right)f_{2n}(\theta)d\theta \qquad (148)$$

$$n=0,...,M$$

where

$$\begin{aligned} f_0(\theta) &= g(\theta) && m=0 \\ f_{2m}(\theta) &= -\psi_{A02m}(\theta)+\psi_{A02m}(\pi/2) && m>0 \end{aligned} \qquad (149)$$

and

$$g(\theta)=\frac{1}{\sigma_a}\sum_{n=0}^{N}(-1)^n a_{2n-1}\cos((2\,\mathrm{n}-1)\theta)\ . \qquad (150)$$

Finally M_0 and N_0 are computed as

$$\begin{aligned} M_0 = &-\frac{1}{\sigma_a}\int_0^{\pi/2}\phi_{B0s}(\theta)\sum_{n=0}^{N}\left\{(-1)^n(2n-1)a_{2n-1}\sin((2n-1)\theta)\right\} \\ &+\frac{\pi}{4\sigma_a}\sum_{m=1}^{N-1}\left\{(-1)^m Q_{2m}(2m+1)a_{2m+1}\right\} \\ &+\frac{\xi_b}{\sigma_a^2}\sum_{m=1}^{M}\left\{(-1)^m Q_{2m}\sum_{n=0}^{N}\sum_{i=0}^{N}\left\{\frac{(2n-1)(2i-1)}{(2m+2i)^2-(2n-1)^2}a_{2n-1}a_{2i-1}\right\}\right\} \end{aligned} \qquad (151)$$

and

$$\begin{aligned} N_0 = &-\frac{1}{\sigma_a}\int_0^{\pi/2}\phi_{B0c}(\theta)\sum_{n=0}^{N}\left\{(-1)^n(2n-1)a_{2n-1}\sin((2n-1)\theta)\right\} \\ &+\frac{\pi}{4\sigma_a}\sum_{m=1}^{N-1}\left\{(-1)^m P_{2m}(2m+1)a_{2m+1}\right\} \\ &+\frac{\xi_b}{\sigma_a^2}\sum_{m=1}^{M}\left\{(-1)^m P_{2m}\sum_{n=0}^{N}\sum_{i=0}^{N}\left\{\frac{(2n-1)(2i-1)}{(2m+2i)^2-(2n-1)^2}a_{2n-1}a_{2i-1}\right\}\right\} \end{aligned} \quad . \qquad (152)$$

Roll Coefficients

To calculate the roll coefficients a_{44} and b_{44} in (19) and (20) it is necessary to determine the values of P_0, Q_0, X_R, and Y_R. Following the same procedure used in the heave coefficients to define a set of velocity potential and stream functions results in

$$\phi_{A2m}(\alpha,\theta) = e^{-(2m+1)\alpha}\sin((2m+1)\theta) - \frac{\xi_b}{\sigma_a}\sum_{n=0}^{N}\left\{(-1)^n\frac{2n-1}{2m+2n}a_{2n-1}e^{-(2m+2n)\alpha}\sin((2m+2n)\theta)\right\}, \quad (153)$$

$$\psi_{A2m}(\alpha,\theta) = -e^{-(2m+1)\alpha}\cos((2m+1)\theta) + \frac{\xi_b}{\sigma_a}\sum_{n=0}^{N}\left\{(-1)^n\frac{2n-1}{2m+2n}a_{2n-1}e^{-(2m+2n)\alpha}\cos((2m+2n)\theta)\right\}, \quad (154)$$

$$\psi_{Bc} = +\pi e^{-\nu y}\cos(\nu x), \quad (155)$$

$$\psi_{Bs} = +\pi e^{-\nu y}\sin(\nu|x|) + \int_o^\infty \frac{\nu\sin(ky) - k\cos(ky)}{k^2+\nu^2}e^{-k|x|}dk - \frac{y}{\nu(x^2+y^2)}, \quad (156)$$

$$j\phi_{Bc} = -\pi e^{-\nu y}\sin(\nu|x|), \quad (157)$$

$$j\phi_{Bs} = +\pi e^{-\nu y}\cos(\nu x) - \int_o^\infty \frac{\nu\cos(ky) + k\sin(ky)}{k^2+\nu^2}e^{-k|x|}dk + \frac{|x|}{\nu(x^2+y^2)}. \quad (158)$$

Here, $\nu = \frac{\omega^2}{g}$ is the wave number in deep water and

$$\begin{aligned} j &= +1 \quad for:\ x \geq 0 \\ j &= -1 \quad for:\ x < 0 \end{aligned}. \quad (159)$$

The P_{2m} and Q_{2m} terms are calculated as

$$\sum_{m=0}^{M}\left\{P_{2m}\int_0^{\pi/2} f_{2m}(\theta)\,f_{2n}(\theta)d\theta\right\}=\int_0^{\pi/2}\left(\psi_{B0c}(\theta)-\psi_{B0c}(\pi/2)\right)f_{2n}(\theta)d\theta$$
$$\sum_{m=0}^{M}\left\{Q_{2m}\int_0^{\pi/2} f_{2m}(\theta)\,f_{2n}(\theta)d\theta\right\}=\int_0^{\pi/2}\left(\psi_{B0s}(\theta)-\psi_{B0s}(\pi/2)\right)f_{2n}(\theta)d\theta \qquad (160)$$
$$n=0,...,M$$

where

$$\begin{aligned} f_0(\theta)&=\mu(\theta)-1 && m=0\\ f_{2m}(\theta)&=-\psi_{A02m}(\theta)+\psi_{A02m}(\pi/2) && m>0\end{aligned} \qquad (161)$$

and

$$\mu(\theta)=\frac{x_0^2+y_0^2}{(b_0/2)^2}=\left(-\frac{1}{\sigma_a}\sum_{n=0}^{N}\left\{(-1)^n a_{2n-1}\sin((2n-1)\theta)\right\}\right)^2 + \left(\frac{1}{\sigma_a}\sum_{n=0}^{N}\left\{(-1)^n a_{2n-1}\cos((2n-1)\theta)\right\}\right)^2 . \qquad (162)$$

Finally X_R and Y_R are computed as

$$\begin{aligned} X_R=&\frac{1}{2\sigma_a^2}\int_0^{\pi/2}\phi_{B0c}(\theta)\sum_{n=0}^{N}\sum_{i=0}^{N}\left\{(-1)^{n+i}(2i-1)a_{2n-1}a_{2i-1}\sin((2n-2i)\theta)\right\}d\theta\\ &+\frac{1}{2\sigma_a^2}\sum_{m=1}^{M}\left\{(-1)^m P_{2m}\sum_{n=0}^{N}\sum_{i=0}^{N}\left\{\frac{(2i-1)(2n-2i)}{(2m+1)^2-(2n-2i)^2}a_{2n-1}a_{2i-1}\right\}\right\}\\ &-\frac{\pi\xi_b}{8\sigma_a^3}\sum_{m=1}^{M}\left\{\begin{array}{l}(-1)^m P_{2m}\cdot\\ \left(\begin{array}{l}\displaystyle\sum_{n=m}^{N}\sum_{i=0}^{n-m}\left\{\frac{(-2m+2n-2i-1)(2i-1)}{2n-2i}a_{2n-1}a_{2i-1}a_{-2m+2n-2i-1}\right\}\\ \displaystyle+\sum_{n=0}^{N-m}\sum_{i=m+n}^{N}\left\{\frac{(-2m-2n+2i-1)(2i-1)}{2n-2i}a_{2n-1}a_{2i-1}a_{-2m-2n+2i-1}\right\}\end{array}\right)\end{array}\right\}\end{aligned} \qquad (163)$$

and

$$
\begin{aligned}
Y_R = & \frac{1}{2\sigma_a^2}\int_0^{\pi/2}\phi_{B0s}(\theta)\sum_{n=0}^{N}\sum_{i=0}^{N}\left\{(-1)^{n+i}(2i-1)a_{2n-1}a_{2i-1}\sin((2n-2i)\theta)\right\}d\theta \\
& + \frac{1}{2\sigma_a^2}\sum_{m=1}^{M}\left\{(-1)^m Q_{2m}\sum_{n=0}^{N}\sum_{i=0}^{N}\left\{\frac{(2i-1)(2n-2i)}{(2m+1)^2-(2n-2i)^2}a_{2n-1}a_{2i-1}\right\}\right\} \\
& - \frac{\pi\xi_b}{8\sigma_a^3}\sum_{m=1}^{M}\left\{\begin{array}{l}(-1)^m Q_{2m}\cdot \\ \left(\begin{array}{l}\displaystyle\sum_{n=m}^{N}\sum_{i=0}^{n-m}\left\{\frac{(-2m+2n-2i-1)(2i-1)}{2n-2i}a_{2n-1}a_{2i-1}a_{-2m+2n-2i-1}\right\} \\ \displaystyle+\sum_{n=0}^{N-m}\sum_{i=m+n}^{N}\left\{\frac{(-2m-2n+2i-1)(2i-1)}{2n-2i}a_{2n-1}a_{2i-1}a_{-2m-2n+2i-1}\right\}\end{array}\right)\end{array}\right\}
\end{aligned}
\quad . (164)
$$

Coefficients of Roll Motion Coupled into Sway Motion

To calculate the coefficients a_{24} and b_{24} in (19) and (20), it is necessary to determine the values of M_0, N_0, P_0, and Q_0. The coefficients P_0 and Q_0 have already been determined by (160) in the procedure for finding the roll motion coefficients. The terms M_0 and N_0 are computed by (151) and (152) in the sway coefficient routine using the values for P_{2m} and Q_{2m} which were computed from (160).

APPENDIX: D HYDRODYNAMIC COEFFICIENTS OF A SHIP WITH FORWARD SPEED

The hydrodynamic coefficients of a ship with forward speed are given by [17]

$$
\begin{aligned}
A_{22} &= \int_0^L a_{22}dx - \frac{U}{\omega_e^2} b_{22}^A \\
A_{24} &= \int_0^L a_{24}dx - \frac{U}{\omega_e^2} b_{24}^A \\
A_{26} &= \int_0^L xa_{22}dx + \frac{U}{\omega_e^2}\int_0^L b_{22}dx - \frac{U}{\omega_e^2} x_a b_{22}^A + \frac{U^2}{\omega_e^2} a_{22}^A \\
A_{33} &= \int_0^L a_{33}dx - \frac{U}{\omega_e^2} b_{33}^A \\
A_{35} &= -\int_0^L xa_{33}dx - \frac{U}{\omega_e^2}\int_0^L b_{33}dx + \frac{U}{\omega_e^2} x_a b_{33}^A - \frac{U^2}{\omega_e^2} a_{33}^A \\
A_{42} &= A_{24} \\
A_{44} &= \int_0^L a_{44}dx - \frac{U}{\omega_e^2} b_{44}^A \\
A_{46} &= \int_0^L xa_{24}dx + \frac{U}{\omega_e^2}\int_0^L b_{24}dx - \frac{U}{\omega_e^2} x_a b_{24}^A + \frac{U^2}{\omega_e^2} a_{24}^A \\
A_{53} &= -\int_0^L xa_{33}dx + \frac{U}{\omega_e^2}\int_0^L b_{33}dx + \frac{U}{\omega_e^2} x_a b_{33}^A \\
A_{55} &= \int_0^L x^2 a_{33}dx + \frac{U}{\omega_e^2}\int_0^L b_{33}dx - \frac{U}{\omega_e^2} x_a b_{33}^A + \frac{U^2}{\omega_e^2} a_{33}^A \\
A_{62} &= \int_0^L xa_{22}dx + \frac{U}{\omega_e^2}\int_0^L b_{22}dx - \frac{U}{\omega_e^2} x_a b_{22}^A + \frac{U^2}{\omega_e^2} a_{22}^A \\
A_{64} &= \int_0^L xa_{24}dx - \frac{U}{\omega_e^2}\int_0^L b_{24}dx - \frac{U}{\omega_e^2} x_a b_{24}^A \\
A_{66} &= \int_0^L x^2 a_{22}dx + \frac{U}{\omega_e^2}\int_0^L a_{22}dx - \frac{U}{\omega_e^2} x_a^2 b_{22}^A + \frac{U^2}{\omega_e^2} a_a a_{22}^A
\end{aligned}
\tag{165}
$$

and

$$
\begin{aligned}
B_{22} &= \int_0^L b_{22}dx + Ua_{22}^a \\
B_{24} &= \int_0^L b_{24}dx + Ua_{24}^a \\
B_{26} &= \int_0^L b_{22}dx - U\int_0^L a_{22}dx + Ux_a a_{22}^A + \frac{U^2}{\omega_e^2}b_{22}^A \\
B_{33} &= \int_0^L b_{33}dx + Ua_{33}^a \\
B_{35} &= -\int_0^L xb_{33}dx + U\int_0^L a_{33}dx - Ux_a a_{33}^A - \frac{U^2}{\omega_e^2}b_{33}^A \\
B_{42} &= B_{24} \\
B_{44} &= \int_0^L b_{44}dx + Ua_{44}^a \\
B_{46} &= \int_0^L xb_{24}dx - U\int_0^L a_{24}dx + Ux_a a_{24}^A + \frac{U^2}{\omega_e^2}b_{24}^A \\
B_{53} &= -\int_0^L xb_{33}dx - U\int_0^L a_{33}dx - Ux_a a_{33}^A \\
B_{55} &= \int_0^L x^2 b_{33}dx + \frac{U^2}{\omega_e^2}\int_0^L b_{33}dx + Ux_a^2 a_{33}^A + \frac{U^2}{\omega_e^2}a_a b_{33}^A \\
B_{62} &= \int_0^L xb_{22}dx + U\int_0^L a_{22}dx + Ux_a a_{22}^A \\
B_{64} &= \int_0^L xb_{24}dx + U\int_0^L a_{24}dx + Ux_a a_{24}^A \\
B_{66} &= \int_0^L x^2 b_{22}dx + \frac{U^2}{\omega_e^2}\int_0^L b_{22}dx + Ux_a^2 a_{22}^A + \frac{U^2}{\omega_e^2}x_a b_{22}^A
\end{aligned}
\tag{166}
$$

where subscript a and superscript A refer to the aftmost section, x is the x-coordinate of the section in the body-fixed system, U is the ship's forward speed in m/s, and ω_e is the encounter frequency.

REFERENCES

[1] J. J. Holmes, "Reduction of a Ship's Magnetic Field Signatures," *Synthesis Lectures on Computational Electromagnetics,* vol. 3, pp. 1-68, 2008.

[2] J. J. Holmes, "Exploitation of a Ship's Magnetic Field Signatures," *Synthesis Lectures on Computational Electromagnetics,* vol. 1, pp. 1-78, 2006.

[3] H. ElBidweihy, C. D. Burgy, and E. Della Torre, "Stress-Associated Changes in the Magnetic Properties of High Strength Steels," *Physica B: Condensed Matter,* vol. 435, pp. 16-20, 2014.

[4] R. Bozorth and H. Williams, "Effect of Small Stresses on Magnetic Properties," *Reviews of Modern Physics,* vol. 17, p. 72, 1945.

[5] W. F. Brown Jr, "Irreversible Magnetic Effects of Stress," *Physical Review,* vol. 75, p. 147, 1949.

[6] E. Ovegård, "Numerical Simulation of Parametric Rolling in Waves," KTH, Stockholm, Sweden, 2009.

[7] J. O. Hallquist, "LS-DYNA Theory Manual," *Livermore Software Technology Corporation,* 2006.

[8] J. M. J. Journée and L. J. M. Adegeest, "Theoretical Manual of Strip Theory Program “SEAWAY for Windows”," *TU Delft Report,* vol. 1370, 2003.

[9] W. E. Cummins, "The Impulse Response Function and Ship Motions," presented at the Symposium on Ship Theory, Institut fur Schiffbau der Universitat Hamburg, Hamburg, Germany, 1962.

[10] G. Bordogna, "The Aero-Hydrodynamic Characteristics of Yachts Sailing Upwind in Waves," TU Delft, Delft University of Technology, 2013.

[11] J. M. J. Journee, "Hydromechanic Coefficients for Calculating Time Domain Motions of Cutter Section Dredges by Cummins Equations," Delft University of Technology, 1993.

[12] F. Ursell, "On the Heaving Motion of a Circular Cylinder on the Surface of a Fluid," *Quarterly Journal of Mechanics and Applied Mathematics,* vol. 2, pp. 215-231, 1949.

[13] F. Tasai, "On the Damping Force and Added Mass of Ships Heaving and Pitching," Research Institute for Applied Mechanics, Kyushu University, Fukuoka, Japan, 1959.

[14] Z. Thein, "Practical Source Code for Ship Motions Time Domain Numerical Analysis and Its Mobile Device Application," Department of Shipping and Marine Technology, Chalmers University of Technology, Goteburg, Sweden, 2012.

[15] O. Faltinsen, *Sea Loads on Ships and Offshore Structures* vol. 1: Cambridge university press, 1993.

[16] Jeffrey Falzarano, Abhilash Somayajula, and R. Seah, "An Overview of the Prediction Methods for Roll Damping of Ships " *Ocean Systems Engineering,* vol. 5, pp. 55-76, 2015.

[17] J. Hua and M. Palmquist, "A Description of SMS-A Computer Code for Ship Motion Simulation," KTH, Stockholm, Sweden, 1995.

[18] N. Salvesen, E. O. Tuck, and O. Faltinsen, "Ship Motions and Sea Loads," *Trans. SNAME,* vol. 78, pp. 250-287, 1970.

[19] C. G. Soares and J. Parunov, *Advanced Ship Design for Pollution Prevention*: CRC Press, 2010.
[20] J. Journee, "User manual of SEAWAY," *Technology University of Delft,* 2001.
[21] Y. Kawahara, K. Maekawa, and Y. Ikeda, "A Simple Prediction Formula of Roll Damping of Conventional Cargo Ships on the Basis of Ikeda's Method and its Limitation," *Journal of Shipping and Ocean Engineering,* vol. 2, pp. 201-210, 2012.
[22] J. C. Young and S. D. Gedney, "A Locally Corrected Nyström Formulation for the Magnetostatic Volume Integral Equation," *Magnetics, IEEE Transactions on,* vol. 47, pp. 2163-2170, 2011.
[23] J. C. Young, S. D. Gedney, R. Adams, C. Schneider, and C. Burgy, "A Stepped Non-Linear Solver for Non-Linear Magnetic Materials with Hysteresis," *IEEE Transactions on Magnetics,* vol. 51, 2015.
[24] D. C. Jiles, J. Thoelke, and M. Devine, "Numerical Determination of Hysteresis Parameters for the Modeling of Magnetic Properties Using the Theory of Ferromagnetic Hysteresis," *Magnetics, IEEE Transactions on,* vol. 28, pp. 27-35, 1992.
[25] D. Jiles and D. Atherton, "Theory of Ferromagnetic Hysteresis," *Journal of Magnetism and Magnetic Materials,* vol. 61, pp. 48-60, 1986.
[26] I. D. Mayergoyz, *Mathematical Models of Hysteresis and Their Applications*: Academic Press, 2003.
[27] C. S. Schneider, "Maximum Susceptibility of Ferromagnetic Hysteresis," *Magnetics, IEEE Transactions on,* vol. 48, pp. 3371-3374, 2012.
[28] S. D. Gedney and J. C. Young, "Magneto Stress Analysis End of Year Report," University of Kentucky, 2015.
[29] J. Norton and C. Arraez, "Machine Design," 2000.
[30] Y. Kawahara, et al., "A Simple Prediction Formula of Roll Damping of Conventional Cargo Ships on the Basis of Ikeda's Method and Its Limitation," presented at the Proceedings of the 10th International Conference on Stability of Ships and Ocean Vehicles, 2009.
[31] J. Falzarano, A. Somayajula, and R. Seah, "An Overview of the Prediction Methods for Roll Damping of Ships," *Ocean Systems Engineering,* vol. 5, pp. 55-76, 2015.
[32] M. Salehi, P. Ghadimi, and A. B. Rostami, "A more robust multiparameter conformal mapping method for geometry generation of any arbitrary ship section," *Journal of Engineering Mathematics,* vol. 89, pp. 113-136, Dec 2014.
[33] R. P. Brent, *Algorithms for Minimization Without Derivatives*: Courier Corporation, 2013.
[34] W. R. Porter, "Pressure Distributions, Added-Mass, and Damping Coefficients for Cylinders Oscillating in a Free Surface," University of California, Berkeley, 1961.

VITA

Cody Lonsbury received a Bachelor of Science in Electrical Engineering with highest distinction from the University of Kentucky in May of 2014. He is a member of Eta Kappa Nu and Tau Beta Pi engineering honor societies. From May 2013 to May 201 he worked as an Undergraduate Research Assistant for the Computation Electromagnetics Group at the University of Kentucky. From May 2014 to May 2015 he worked as a Co-op Engineer for Cypress Semiconductor in Lexington, KY. He has been working as a Graduate Research Assistant at the University of Kentucky since August 2014.